FORWARD-LOOKING LONG-WAVE INFRARED IMAGE BASED PRE-SCREENER FOR LANDMINE DETECTION

A THESIS SUBMITTED TO
THE GRADUATE SCHOOL OF NATURAL AND APPLIED SCIENCES
OF
MIDDLE EAST TECHNICAL UNIVERSITY

BY

AYLİN DOĞAN

IN PARTIAL FULLFILLMENT OF THE REQUIREMENTS
FOR
THE DEGREE OF MASTER OF SCIENCE
IN
ELECTRICAL AND ELECTRONICS ENGINEERING

JANUARY 2017

Approval of the thesis:

FORWARD-LOOKING LONG-WAVE INFRARED IMAGE BASED PRE-SCRENEER FOR LANDMINE DETECTION

submitted by **AYLİN DOĞAN** in partial fulfillment of the requirements for the degree of **Master of Science in Electrical and Electronics Engineering Department, Middle East Technical University** by,

Prof. Dr. Gülbin Dural Ünver
Dean, Graduate School of **Natural and Applied Sciences** _____

Prof. Dr. Tolga Çiloğlu
Head of Department, **Electrical and Electronics Eng.** _____

Prof. Dr. Gözde Bozdağı Akar
Supervisor, **Electrical and Electronics Eng. Dept., METU** _____

Examining Committee Members:

Assoc. Prof. Dr. İlkay Ulusoy Parnas
Electrical and Electronics Eng. Dept., METU _____

Prof. Dr. Gözde Bozdağı Akar
Electrical and Electronics Eng. Dept., METU _____

Assist. Prof. Sevinç Figen Öktem
Electrical and Electronics Eng. Dept., METU _____

Assoc. Prof. Dr. Uğur Murat Leloğlu
Geodetic and Geographic Inf. Tech. Dept., METU _____

Assist. Prof. Seniha Esen Yüksel
Electrical & Electronics Eng. Dept., Hacettepe University _____

Date: 03/01/2017

I hereby declare that all information in this document has been obtained and presented in accordance with academic rules and ethical conduct. I also declare that, as required by these rules and conduct, I have fully cited and referenced all material and results that are not original to this work.

Name, Last name: Aylin DOĞAN

Signature :

ABSTRACT

FORWARD-LOOKING LONG-WAVE INFRARED IMAGE BASED PRE-SCREENER FOR LANDMINE DETECTION

Doğan, Aylin

M. Sc., Department of Electrical and Electronics Engineering

Supervisor: Prof. Dr. Gözde Bozdağı Akar

January 2017, 140 pages

Infrared imagery is widely used in many applications in both civilian and military areas. In landmine detection, the goal is to detect the anomalies between mine surface and soil from variation of reflected/emitted thermal radiation.

In this thesis, various types of anomaly detection techniques of IR are investigated and the feasibility of these techniques for use in landmine detection is analysed. Additionally, effects of parameters for algorithms are compared and the parameters are optimized for increasing detection accuracy. Furthermore, fusion of the algorithms is performed to reduce False Alarm Rate (FAR). We also prepare an experimental setup to reflect the effects of environmental changes on FLIR imagery recording. Soil and various types of landmine mock-ups are also examined in this setup. Finally, all anomalies are mapped into local coordinate space for indicating possible landmines locations.

Keywords: Anomaly Detection, Forward Looking Infrared Imagery, Long-Wave Infrared, Explosive materials, Anti-personnel landmine

ÖZ

KARA MAYINI TESPİTİ İÇİN İLERİYE BAKAN UZUN DALGA KIZILÖTESİ GÖRÜNTÜLEME TABANLI ÖN GÖRÜNTÜLEYİCİ

Doğan, Aylin
Yüksek Lisans, Elektrik ve Elektronik Mühendisliği Bölümü
Tez Yöneticisi: Prof. Dr. Gözde Bozdağı Akar
Ocak 2017, 140 sayfa

Kızılötesi görüntüleme sivil ve askeri alanlarda sıkça kullanılmaktadır. Gömülü patlayıcılar hem siviller hem de askerler için oldukça önemli tehditlerdir. Mayın tespitindeki amaç, mayın yüzeyi ve toprak arasındaki yansıyan/saçılan ısıl radyasyon farklılığına bağlı oluşan anomalileri tespit etmektir.

Bu tezde, farklı tiplerde anomali tespit algoritmaları incelendi ve belirli durumlar altında bu tekniklerin mayın tespiti için uygulanabilirliği analiz edildi. Ek olarak, algoritma parametrelerinin etkileri karşılaştırıldı ve tespit doğruluğunu arttırmak için optimum hale getirildi. Ayrıca, Yanlış Hata Oranını azaltmak için algoritmaların birleşimi uygulandı. Çevresel faktörelerin İleriye Bakan Kızlötesi görüntü kaydı üzerinde olan etkilerini yasıtmak için ayrıca deneysel test düzeneği hazırladık. Toprak ve mayın çeşitliliği bu düzenekte incelendi. Son olarak, tespit edilmiş tüm anomaliler olası mayın göstergesi olarak yerel koordinat düzlemine aktarıldı.

Anahtar Kelimeler: Anomali Tespiti, İleriye Bakan Kızılötesi Görüntüleme, Uzun-Dalga Kızılötesi, Patlayıcı maddeler, İnsana karşı kara mayını

To my family,

Ayten Bayram,

Hüseyin Bayram,

Aytül Bayram,

and

to my husband,

Fırat Doğan

ACKNOWLEDGEMENTS

First of all, I would like to express my deepest gratitude to my family Ayten Bayram, Hüseyin Bayram and Aytül Bayram for their loving and continued support.

I cannot express enough thanks to my advisor, Prof. Dr. Gözde Bozdağı Akar for her excellent guiding, caring, patience and encouragement throughout the thesis. I had an outstanding research activity under her supervision.

I am grateful to ASELSAN Electronic Industries for giving me opportunity to improve my engineering capabilities and for providing me every kind of hardware, software and financial support.

I would like to thank my manager Ahmet Kırlılar, my chef Bülent Şen for their continuous support. In addition, I would also thank my other colleagues in ASELSAN.

I would like to extend my special appreciation to my husband Fırat Doğan for his support, patience, and kindness throughout my graduate study.

TABLE OF CONTENTS

LIST OF TABLES

TABLES

LIST OF FIGURES

FIGURES

LIST OF ABBREVIATIONS

AP : Anti-Personnel
AAC : Area above ROC
AROC : Area under ROC
AT : Anti-Tank
CFAR : Constant False Alarm Rate
CLAHE : Constant Limited Adaptive Histogram Equalization
DL-GPR : Downward-Looking Ground Penetrating Radar
EMI : Electromagnetic Induction
EO : Electro-Optics
FAR : False Alarm Rate
FLIR : Forward Looking Infrared
FL-LWIR : Forward Looking Long-Wave Infrared
FOV : Field of View
FPR : False Positive Rate
GM : Gaussian Model
GPR : Ground Penetrating Radar
GPS : Global Positioning System
HOG : Histogram of Gradients
IR : Infrared
LBP : Local Binary Pattern
LMS : Least Mean Square
LP : Linear Prediction
L_R : Received Radiance
L_{SKY} : Radiance due to sky
L_{SUN} : Radiance due to sun
L_T : Thermal Radiance
MIL : Multiple Instance Learning
MSER : Maximally Stable Extremal Region

NQR : Nuclear Quadrupole Resonance

PCA : Principal Component Analysis

ROC : Receiver Operating Characteristics

SVD : Singular Value Decomposition

SVM : Support Vector Machine

TPR : True Positive Rate

UTM : Universal Transverse Mercator

VMMD : Vehicle Mounted Mine Detection

ε : Surface Emissivity

ρ : Surface Reflectivity

CHAPTER 1

INTRODUCTION

A landmine is basically an explosive device which is found on or just below the land surface. Landmines are designed to explode when triggered by pressure; caused by a vehicle, a person, an animal, or remote control. Landmines are split into two types: Anti-Personnel (AP) Mines and Anti-Tank (AT) Mines. They have basically the same functionality which is destroying around itself. There are minor differences between them. Anti-tank mines have a purpose to destroy a tank or truck; so that they include more explosive materials and they are larger than Anti-personnel mines. To blow up Anti-tank mines, more pressure should be applied. Anti-personnel mines are designed to kill or injure one or more people. They are threatening both soldiers and civilians. AP mines possess more non-metallic materials compared to AT mines; thus, the detection of AP mines is more difficult.

Landmines were used in World War 1 and then had important role in warfare during World War 2. They have been widely used since World War 2. The aim of the usage of landmines in military is to secure borders and to stop enemy movement during the war. After cessation of military operations, millions of unmarked landmines left buried. Landmines are used to defence in war however, unmarked landmines become the worst environmental problem that affects the humanity. Not only soldiers but also civilians get hurt or killed because of these hazards all around the world [1]. Around 90 countries are under serious threat because of landmines in the world. It is estimated that there are from 50 to 70 million uncleaned landmines within at least 70 countries. About 26,000 people are killed or lost their limb every year by landmines.

As an example, one in 334 people are a landmine amputee in Angola and over 25,000 amputees are injured from mine blasts in Cambodia [2]. Landmines also impede over 22 million people's lives to return normal life. They cannot farm if any suspicion about buried explosives on land exists [3]. In Table 1 and Table 2, the countries and corresponding landmines / damages on human life in 2013 are shown [2].

Table 1 World Distribution of Landmines

Country	**Uncleaned Landmines**
Africa	18 – 30 million
Afghanistan	10 – 15 million
Angola	9 million
Cambodia	4-7 million
Iraq	4 million
Yugoslavia	3 million
Mozambique	2 million
Somalia	1 – 2 million
Sudan	1 – 2 million
Croatia	1 million
Serbia	0.5 – 1 million
Eritrea & Ethiopia	0.3 – 1 million
Bosnia	0.2 million
TOTAL	54 – 77.2million

Table 2 Landmine Damage on Human Life

Country	**Damage on Human Life (Killed - Injured)**
Afghanistan	350,000 – 500,000
Angola	26,000
Cambodia	30,000
Yugoslavia	600,000
Mozambique	6,000

When the damage created by landmine is considered, cleaning the world from mines becomes an important topic. There have been many technologies developed and they are still being improved to identify, detect and clear landmines. Traditionally, Electromagnetic Induction (EMI) sensors have been used to detect buried landmines

by inducing a current in the metal content. However, the metal content in landmine can vary depending on construction from a large amount of metal to plastic-cased with low-metal. EMI sensors suffer from detection of low-metal landmines. Additionally, there is lots of metallic clutter in environment. As a consequence, to detect low-metal mines, the threshold of EMI sensor should be small and this causes high False Alarm Rates (FAR) [4], [5]. To overcome these problems, there is significantly research effort that has been done [6].

Due to limits of EMI sensors and detection from EMI data, Ground Penetrating Radar (GPR) has been proposed to reduce FAR. In GPR system, an electronic radar pulse is projected into the ground. Differences in dielectric constants of ground and mine cause reflections, which are collected at receiver antenna. The signature of buried target or subsurface layer is investigated from reflected signal. Thus, GPR introduces a different phenomenology compared to EMI. Rather than metal content, GPR is sensitive to discontinuities in the electrical properties of media [7], [8], [9], [10], [11], [12].

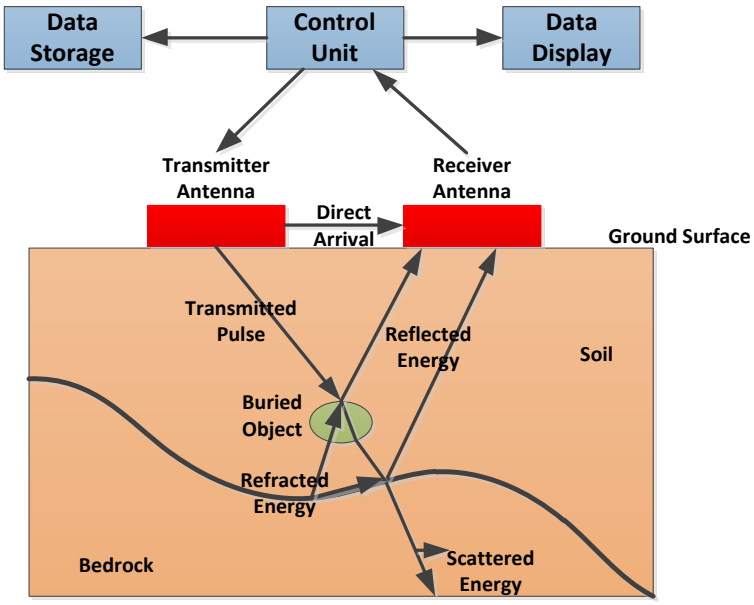

Figure 1 GPR Sensing Methodology

Besides low FAR, detection standoff distance also is an important parameter in the system. The typical distance between an alarm and landmine detection system, when

that alarm is detected by the system operator, is called as “detection standoff distance”. GPR suffers from short detection standoff. This is critical; because, operator does not have so much time to stop if a landmine exists in GPR system. While data is being processed after gathered by GPR sensors, vehicle approaches even closer to the alarm location. Besides short detection standoff, landmine detection system should move faster in some applications. GPR does not meet large standoff distance and not allow the vehicle to move faster. One of the ways to increase detection standoff distance is Forward Looking Infrared (FLIR) camera. The thermal energy is received by FLIR camera and the Infrared (IR) video is recorded in gray-scale domain. Buried landmines the thermal properties changing of surrounding soil and differences in IR characteristics can be used in detection [13]. The methodology is shown in Figure 2.

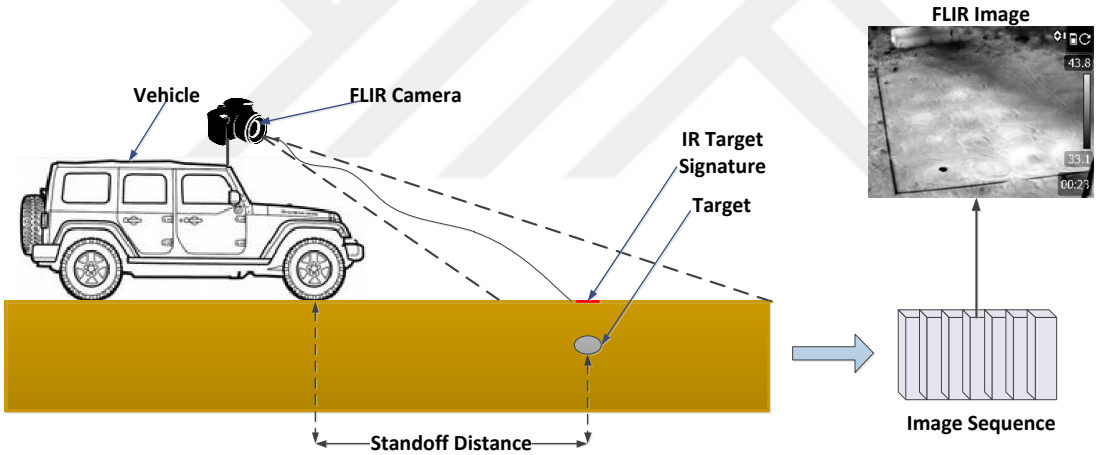

Figure 2 FLIR Sensing Methodology

There are also other landmine detection methods. Acoustic technique is based on sending acoustic waves into the ground. Reflected sound waves on boundaries between materials have different acoustic properties. The detection is done with these differences. However, the accuracy of acoustic measurements is poor because of the soil inhomogeneity. Signals are highly absorbed by sand during the propagation and air-to-ground interface causes strong disturbances [14]. Vapour sensors, Nuclear Quadrupole Resonance (NQR) devices, hyper spectral imaging, X-

Ray backscatter, neutron methods, biological methods (dogs, rates, bees, and bacteria) are other novel sensing techniques used for mine detection [64], [65].

1.1 Scope and Outline of the Thesis

Detection of buried landmines and labelling as target and non-target are complex procedures that require huge number of data. Pre-screener is preparation phase which minimizes required number of data. The scope of this thesis is to use FLIR image based pre-screener for landmine detection to increase standoff distance and to find possible landmine locations in the system. GPR suffers from short standoff distance; so GPR requires much more time to complete detection process. When FLIR imagery is used as pre-screener combined with the GPR system, the system standoff distance and vehicle speed are increased [73]. Besides these advantages, possible landmine coordinates extracted by FLIR image trigger GPR pre-screener which only detects the targets at received coordinates. The candidate landmine alarm locations are detected by FLIR at a very large standoff distance. The GPR pre-screener gets the possible alarm coordinates at far away before starting detection at that boundary. If the area is empty in the front of GPR, the processing algorithms are not required to run until possible alarm coordinates detected by FLIR. As a result of this, the detection on GPR system requires shorter time with FLIR. This enables to vehicle moving faster in the area. The contribution of this thesis is that in order to achieve a FLIR image based pre-screener; we implement state of the art anomaly detection algorithms and compare their performances and robustness to parameter changes on several datasets. We select 4 state of art anomaly detection algorithms which are Trainable Size Contrast Filter, Corner, Gaussian Model and Maximally Stable Extremal Region based landmine detection algorithms; because different kind of features are used to compensate disadvantages to each other under different circumstances. We further fuse all detection algorithms to reduce FAR [15], [16], [17], [18] and [19]. We also prepare an experimental setup to reflect the effects of environmental changes on FLIR imagery recording. Soil and various types of landmine mock-ups are also examined in this setup. Finally, all anomalies are mapped into local coordinate system for indicating possible landmines.

Based on the above mentioned content, this thesis is organized as follows. Initially, Chapter 1 describe briefly landmine types and landmine detection methods. In Chapter 2, previous work in literature about GPR and FLIR as pre-screener is given. In Chapter 3, the operation of landmine detection algorithms on FLIR imagery is explained. Additionally, our test setup is explained in detail and data capturing process is mentioned. In Chapter 4, implementation, simulation and results of detection algorithms with train and test frames are discussed. Finally, the thesis work is ended by giving summary, conclusion and future work in Chapter 5.

CHAPTER 2

LITERATURE REVIEW

Buried landmine detection has long been studied both on GPR and IR data. In GPR system, pre-screening is an important preliminary work to minimize the amount of data which is then processed by a complicated discrimination algorithm. In this thesis, FLIR camera is used as pre-screener to indicate the potential locations of mine targets. Therefore, the literature overview of the existing pre-screener algorithms on GPR and the algorithms on FLIR imagery to landmine detection are given below.

2.1 Ground Penetrating Radar Technology in Landmine Detection

The first radar system was found by Christian Hülsmeyer on April, 1904 [20]. His studies were based on to detect remote terrestrial metal objects. However, first usage of radar technology on buried objects was introduced Gotthelf Leimbach and Heinrich Löwy in 1910 [21]. The main feature of this work was that the system used surface antennas combined with continuous-wave radar. The first pulsed radar technique was appeared by Dr. Hülsenbeck in 1926 [22]. However; Pulsed GPR systems transmitted low mean signal power compared to CW GPR, the manufacturing of Pulsed GPR systems were easier, lower cost and required low level of signal processing. One of the first worldwide applications on measuring depth of a glacier applying by GPR was developed by W. Stern in 1926 [23]. This technology was not used until the Second World War. After the war, the researchers began to work on radar system for military applications. Nilsson was extended GPR system in 1978 [23]. The first vehicle mounted GPR system was developed by Morey in 1998. A wide range of researches on GPR system have been done until today.

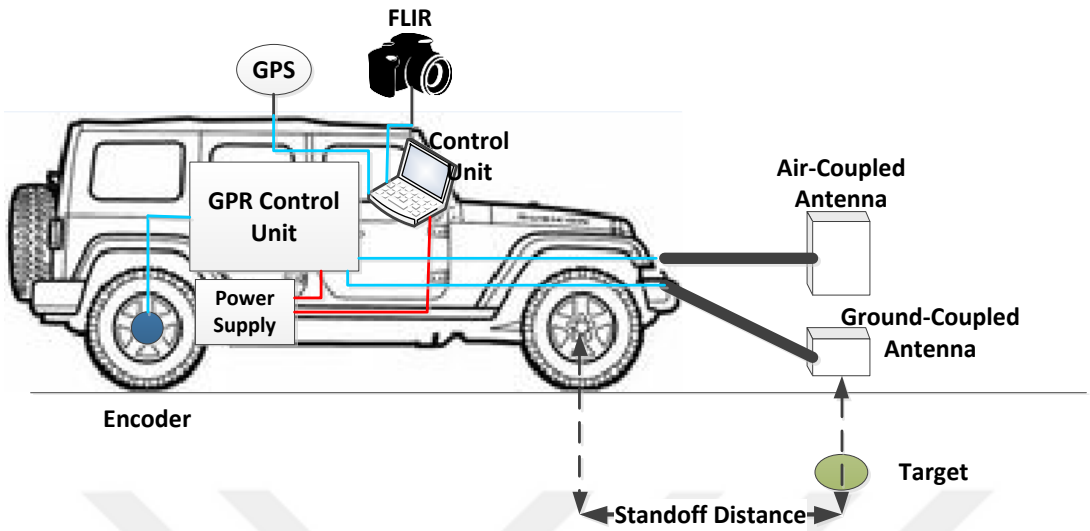

Figure 3 GPR System

The Control Unit of GPR system is divided into six parts as shown in Figure 4.

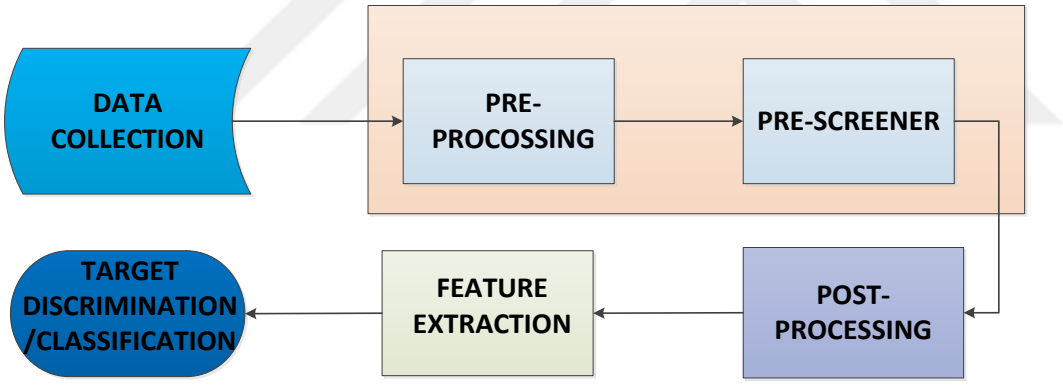

Figure 4 GPR Based Landmine Detection Flow

In any operations, before performing data on anomaly detector, pre-processing is required. The goal of pre-processing is to minimize the effects of the air/ground interactions on received data, smooth the data, suppress external noise and separate the data into depth-sections.

2.1.1 Pre-processing

The large dielectric discontinuity between air and ground is called as “Ground Bounce”. In 2001, Abrahamsson et al. [24] stated ground bounce was major source interference in GPR signals.

Ground Bounce Removal is one of the pre-processing steps. There are mainly three types of Ground Bounce Removal approach in literature. The first Ground Bounce Removal algorithm was implemented by Abrahamsson et al. [24] and Wu et al. [29] in 2001. They worked on GPR signals and Gader et al. [30] implemented these algorithms on landmine detection in 2003. Ho & Gader [28] stated in their work in 2008, there were two popular approaches to remove ground bounce. The first approach was the removing predetermined depth from aligned ground bounced data. If there were shallow targets, there consisted potential risk of removing responses from targets. The second was introduced by Ho & Gader [31] in 2002. According to this work, Linear-Prediction (LP) method was implemented. It based on subtract out the ground response at the current vector. The background was found from weighted sum of the past few of them. Maximum likelihood estimation method was used to find the weighting coefficients which were different for each sample location. Taking difference between current sample and background sample gave the removal of ground bounce. These two methods suffered from computational complexity and shallow targets could not be detected. To increase the performance of pre-screener, in 2006 Torrione & Collins [32] applied Kalman filtering method for ground response tracking. Computational complexity and latency was reduced with Kalman Filter. This proposed method resulted lower net false alarm rate and higher probability of detection for landmine detection.

The other step for pre-processing is to reduce unwanted speckle noise in GPR system. GPR system in Figure 2 is equipped with Global Positioning System (GPS) system which provides external data to Control Unit. The antennas of GPR system cover very wide band and they are susceptible to interference. Torrione et al. [26] and Collins et al. [27] explained that very high energy and very high frequency speckle noise were generated by the occasion of GPS system. To remove speckle noise, Median Filtering method was proposed by Huang, Yang and Tang [33] in 1979. Then, this algorithm was used in several applications in GPR system to remove unwanted speckle noise [26], [27], [28], [34], [35].

Depth segmentation is the other pre-processing before pre-screener. While signal is propagating, it losses energy and reflections from targets and sub-ground have different properties depending on their distance from the radar. Therefore, shallow buried landmines have higher energy compared to hollow ones. The purpose of whitening step is to mitigate these effects stated by Torrione et al [26], Collins et al. [27]. They explained that to reduce these effects adaptive whitening techniques were used; however estimating of signal variance adaptively was processed by computational complexity algorithm. The algorithm was implemented by Gader & Lee & Wilson [36]. Torrione et al. [26], Collins et al. [27] segmented data into "depth bins". They did this under estimation GPR response statistics which did not change dramatically. They aimed in their researches to reduce complexity of the adaptive whitening algorithm.

2.1.2 Pre-screener

After data is processed by pre-processing algorithms, there are several algorithms have been implemented to find anomalies. This section gives literature research on different pre-screener algorithms and implemented areas. There are novel pre-screener algorithms frequently used in literature such as Least Mean Square (LMS), Constant False Alarm Rate (CFAR) and Principal Component Analysis (PCA).

One of the pre-screener algorithms is Least Mean Square (LMS) algorithm. Widrow et al., and Widrow & Stearns [38], originally developed LMS algorithm in 1976 and 1985 respectively. The weights in transversal adaptive filter structure were updated according to gradient descent algorithm [39]. Extension of 2-D LMS algorithm was derived by Hadhoud & Thomas in 1988 [40]. After development of 2-D LMS algorithm, image processing areas used this algorithm in several applications such as image enhancement and image data compression. Azami-Sadjadi & Pan [41] explained other derived LMS based algorithms both in 1-D and 2-D in 1994. Chen & Kao [42] also proposed efficient 2-D LMS adaptive filtering algorithm. Small object detection in correlated clutter was enhanced by French et al. in 1997. In GPR system, 2-D LMS algorithm was used to detect possible landmine locations. Torrione et al. [26] and Collins et al. [27] applied 2-D LMS algorithm as pre-screener to GPR

signal. According to algorithm, the input signal filtered by weighted vector, then difference between desired signal and filtered signal was the result of the LMS stage, called as prediction error. For new sample, the weight vector was updated by using previous weight, mean, error and previous input data. The prediction error gave the information about the location of interest. Each sample in depth bin produced a prediction error and net error was calculated by squaring and summing the all prediction errors in each depth bin. Finally, by applying threshold to the net errors, possible alarms were located.

When pulse is sent to the ground, the received signal from mine has high energy contrast to the background. Constant False Alarm Rate (CFAR) is a type of pre-screener metric which measures the local contrast between background and foreground. The first analysis of CFAR was improved by Gandhi & Kassam [48] in 1988 while the background was non-homogeneous. Under arbitrary clutter distributions, Srinivasan [49] analysed CFAR detection algorithm. In 2004, CFAR method was used as pre-screener in landmine detection with GPR system. Gader et al. [36] derived CFAR algorithm which firstly computed mean and standard deviation of comparison region. While GPR system was moving, the track was segmented into three regions. The first one was point where the target was in, the second was the guard region which the region between mine location and background and should not be included in the calculations; finally comparison regions located before and after target. If the normalization value was high, then the anomalies were detected for further calculation to detect landmines. Kalika et al. [46] took forward this application in 2015. They also implemented CFAR algorithm in GPR signal processing, however, there were some difficulties such as inaccurate background statistics, varying of soil conditions between foreground and background. The next pre-screener enhances to detection landmine under these conditions.

Principal Component Analysis (PCA), which is used widely in GPR system, is one of the pre-screener methods. According to observations, the energy of clutter and noise does not change so much across scans and also they have less energy compared to

mines. In 1999, Yu & Mehra & Witten [44] used PCA as pre-screener for mine detection. The purpose of this research was to model noise rather than GPR signal features then subtract from signal. The subtraction result represented target energy. According to algorithm, the GPR signal was represented as combination of low-rank background signal and sparse foreground signal called as target. The eigenvectors of the corresponding largest eigenvalues of covariance matrix was used to take projection. After isolation from scan to scan by using projected signal, the possible mine location or background was discriminated by using threshold. Reichman et al. [45] also implemented PCA method as pre-screener in 2014. To model soil heterogeneity was hard task and they proposed aligning scans using PCA. However, modelling GPR data as estimating the sum of the background and foreground was not truly correct assumption. To get more robust results, the error should be considered. Thus, detection landmine with robust principal component analysis was studied by Kalika et al. [46] in 2015 based on Candes et al [47] in 2009. In this algorithm, the aim was to minimize the rank of the background, foreground sparsity and error for reconstruction.

2.2 Forward Looking Infrared Technology in Landmine Detection

The infrared radiation concept is the critical part to understand the infrared imagery technology. Visible light which can be seen by human vision is the small part of the electromagnetic spectrum. Electromagnetic spectrum is scale which classifies the different types of electromagnetic radiation such as gamma rays, X-rays, ultraviolet rays, visible rays, infrared rays, microwaves and radio waves [80]. The categorization of these rays is based on wavelength (or frequency). 400 nm – 700 nm (790 THz – 430 THz) and 700 nm – 1 mm (430 THz – 300 GHz) are classified as visible light and infrared light respectively. Infrared light was discovered by Herschel, in 1800 [81]. The thermal imaging region is between 8 μm – 15 μm called as Long Wave Infrared (LWIR).

IR radiation reveals from all warm-blood animals and all objects with temperatures above absolute zero, because atomic and molecular activity cannot be occurred at absolute zero. The increasing of temperature also increases the atomic and molecular

activity. There is a relationship between temperature and the amount of emitted thermal radiation which depends on Emissivity $\mathcal{E}$. The definition of emissivity is that the ratio of the energy radiated from material's surface to that radiated from blackbody under the same conditions such as wavelength and temperature [82]. Blackbody is called a perfect emitter and value is 1. A perfect reflector is assigned as 0. Emissivity is a dimensionless number between 0 and 1. It depends also nature of the surface. Polished metal surface will have lower emissivity compared to a rough one. On the other hand, oxidized metal surface will have higher emissivity compared to deoxidized one. As more heat and thermal radiation is brought out, more infrared radiation is emitted. Hot objects produce more infrared radiation than cool objects. This characteristic gives important information to IR image acquisition process. Depending on the temperature difference the object and the surroundings of it, landmines can be detected by IR camera.

After the discovery of infrared by Herschel in 1800, the first heat picture was created by Herschel in 1840 and also he managed to get primitive record of the thermal image on paper. Thermal imagery provided to detect infrared energy and created image out small heat differences. The thermal imagery technology was developed during the century. In 1978, the IR imaging system mounted on vehicle is realized by FLIR [84].

Infrared (IR) methods have been used in several applications such as border surveillance, force protection, search and rescue people by identifying friend or foe, law enforcement, night vision. Landmine detection is another execution area of IR imaging. IR imagery in landmine detection has started to be used by Nelson [50], since 2000. The goal of the methods is the detecting the anomalous between mine surface and soil from variation of reflected/emitted thermal radiation. Nelson also states that Forward Looking is critical to get Wide Field of View (WFOV) in Vehicle Mounted Mine Detection (VMMD) System. FLIR sensors offer to ability on detection of shallow buried (≤ 15 cm) non-metallic and metallic landmine. In sub-sections; the algorithms, has been used in literature to improve landmine detection system by decreasing False Alarm Rate (FAR), are explained.

As previously stated that, detection landmine using FLIR is based on the principle that the difference on thermal conductivity, thermal capacity and/or density between mine and surrounding soil. The mine could be cooler or warmer compared to soil [15]. The temperature difference is measured by FLIR. However, Kevin et al. [51] state that the thermal equilibrium changes in diurnal cross-over period. During the daylight changing, the cooling and heating process at landmine forms differences in temperature between soils immediately surround it and soils elsewhere in the ground. Detection principal is based on this temperature differences. At morning, landmine is indicated as dark region and at afternoon, landmines have a higher temperature region than ground with a bright region in captured image. There is an important issue to detect landmine on IR imagery. The maximum burial depth should be 10 cm to detect a significant thermal signature of a landmine at the surface, so, anti-personnel landmines could be detected by IR imagery technique. Anti-tank landmines are buried deeper and they cannot detected by IR [74].

Although IR imagery is a good technique for landmine detection, this system has some limitations. Firstly, the environment is not homogeneous. There are vegetation, rocks etc. all around the detection area. These cause image clutter in IR imagery and cause FA. When soil and buried target are in thermal equilibrium at times of day, the detection becomes harder [13]. Environment climate is another factor which affects thermal difference and detection performance of IR imagery.

The general FLIR based pre-screener flow is shown in Figure 5. In the next section, the literature review about steps of flow will be explained.

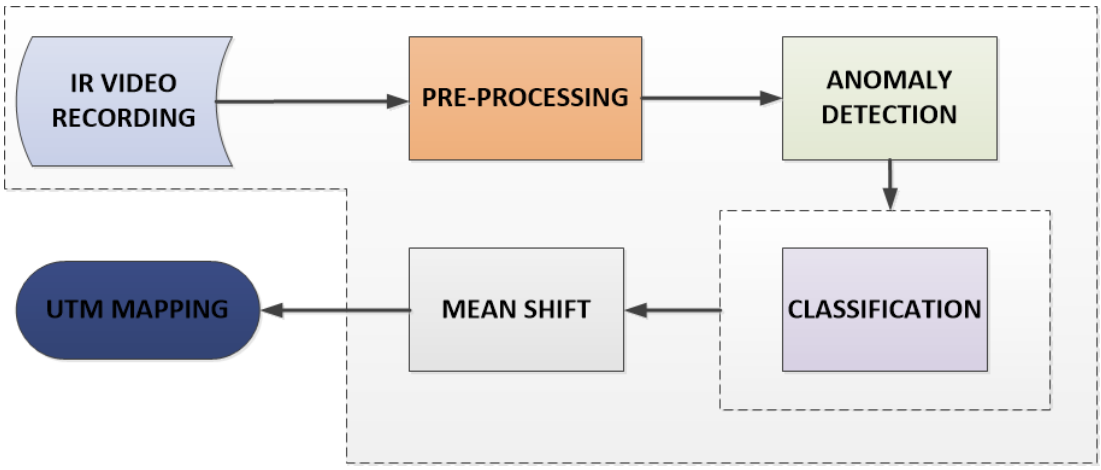

Figure 5 FLIR Based Landmine Detection Flow

2.2.1 Pre-processing

In FLIR system, high standoff distance affects the IR imagery. Before pre-screener process, the IR image should be enhanced in pre-processing step. Histogram Equalization is one of the well-known image enhancement techniques. Gonzales et al. [52] stated that the dynamic range and contrast of image is modified by adjusting image intensities. Rather than applying histogram equalization to entire image, Adaptive Histogram Equalization operated in a small data regions called as tiles and presented by Pizer et al. [53] in 1987. Because of the LWIR sensor and FL context, the brighter regions were close to the vehicle and darker regions were further from vehicle occur in current image. The adaptation of closer and further regions on IR image was solved by Kevin et al. [51] with Contrast Adaptive Histogram Equalization Algorithm (CLAHE) in 2012. By applying some threshold, the histogram was cut and then equalization was processed. The image cut into large number of tiles and each individual tile had enhanced contrast. Improvement of robustness of landmine detection according to time and field of temperature varying has been done by CLAHE algorithm.

2.2.2 Pre-screener

After pre-processing step, pre-screener is run in FLIR system. There are several novel approaches used for landmine detections. In this section, we will explain frequently used detection algorithms in literature.

One of the landmine detection algorithms was proposed by Stone et al. [15] and he defined an algorithm based on ensemble of trainable size-contrast filters and weighted mean shift clustering to detect buried landmines in 2011. According to detection method, there were two windows called inner and outer window. The aim was that to recognize high local image contrast existing and non-existing of buried targets from LWIR image. To detect anomalies, Mahalanobis distance and Bhattacharya distance, defined in Stone et al. [15], were used. These parameters were based on inner and outer window mean and variance. This algorithm has been used widely by Stone and Anderson et al. [13], [15], [16] and [54] to detect landmines from FLIR imagery. Several different sizes of filters have been processed in these researches.

In trainable size filter implementation, the objects in the IR imaging field of view remains at a constant size. However, the objects appear smaller if they are further from vehicle. The improvement on perspective size was done by Popescu et al. [59] with Corner Detection Algorithm which was the other landmine detection algorithm. The properties of corner detection and curvature properties were explained by He & Yung [60] in 2008. Since 2010, Popescu et al. have been improved landmine detection from FLIR imaging.

Gaussian Models (GM) is one of the methods that model background in video. Stauffer and Grimson [57] used GM to detect changing in video surveillance in 1999. The camera and its viewing remained fixed and a background was modelled. When a vehicle was moving across the camera, GM was updated, foreground was learned and object had been tracking while passing through the field of view of camera. GM was also applied to detect buried landmines by Spain et al. [58] in 2010. According the idea, there was slightly differences between concepts. Even though camera was fixed, the camera was mounted at top of vehicle which was moving on the road. In this application, temporal road model was learned and updated while vehicle's motion. Spain et al. [58] stated that each pixel was processed as a mixture of Gaussian distributions. According to histograms of pixels in overall frames, the Gaussian distribution with a given mean and standard deviation was tried to estimate.

After learning of background Gaussian distribution, the new pixel was compared whether it was inside background distribution (<2.5 σ) or not. If pixel was assigned as background/foreground, the labelling was done according to binary function (0/1). The GM background modelling method has been used by Stone and Anderson et al. [13], [16] and [54] and they states that the main advantage compared to previous algorithms, GM detect local recent changes while vehicle is in motion rather than search for buried landmines in a single image.

Another approach is Maximally Stable Extremal Regions (MSER) algorithm based detection for buried landmines. MSER is a type of blob detectors and used widely in stereo. MSER was introduced firstly Anderson et al. [13] in 2011. In 2002, Matas et al. [63] proposed MSER algorithm and he improved robust wide baseline stereo by using MSER algorithm in 2004. Anderson et al. [13], [16], [51] and [54] have been improved landmine detection from FLIR imagery using MSER since 2011. In these papers, the idea of MSER was based on extracting a number of co-variant regions from an image. Extremal regions were defined by Matas et al. [63] as the image regions which were formed by spatially connected pixels with similar threshold intensity. Maximally was explained as the extremal regions (blobs) could be brighter and darker regions according to defined thresholds.

There are also commonly used detection methods based on image texture features. Local Binary Patterns (LBP) is one of these algorithms. In 2006, Heikkilä and Pietikäinen [76] proposed a texture-based method which was modelling the background and detecting moving objects. Popescu et al. [62] applied LBP texture features in FLIR based landmine detection in 2011. In this method, there were P neighbours at a radius and the center pixel was assigned as C. P neighbours were calculated as 0 or 1 whether the P value was smaller or higher than C, respectively. The other texture based detection is Histogram of Gradient (HOG) based landmine detection. In this method, the gradient orientation occurrence was computed. Popescu et al. [77] used LBP and HOG texture features to detect buried explosives based on FLIR image in 2012. On the basis on these studies, Popescu et al. [78] investigated

new study by using Shearlet Features in 2013. The aim was to represent landmine signature with irregular shape in a better way.

After extracting foreground/background information, classification methods were used as next step. According to Popescu et al. [59], they implemented one-class classifier. To remove the hits associated to normal objects such as rocks, tire track, Multiple Instance Learning (MIL) was used as two-class classifier. The algorithm implementation was done by Popescu et al. [62] in 2011. They showed that two-class classifier improved the FAR performance compared to one-class classifier. Support Vector Machine (SVM) was used by Popescu et al. [77] as classification method in 2012.

Mean-Shift algorithm, stated by Cheng [56] in 1995, was used to reduce number of points extracting the features in [55]. Mean-Shift was an iterative method that aimed to locate local maxima of density function given a set of discrete samples. Under defined radius of circular neighbourhood samples, shifting the center of circle to the average of the data points continued until convergence.

Final step for FLIR pre-screener is the registration. The results of trainable size contrast filters were converted into local coordinate space by using Covariance Adaptation Evolutionary Strategy (CMAES) algorithm which explained by Hansen [55]. The transformation matrix from IR image sequences to Universal Transverse Mercator (UTM) coordinates was found by CMAES algorithm under flat earth assumption. In Corner based detection explained by Popescu et al. [62], classified objects were converted to UTM coordinates as trainable size filter and mean-shift clustering, stated by Cheng [56], processed on UTM coordinates. In GM, proposed by Spain et al. [58], after labelling the pixels as foreground/background (1/0), foregrounds were mapped into UTM spaces. In MSER, proposed by Anderson et al. [13], the outcome of blobs was mapped into UTM spaces. In LBP and HOG feature based detection used by Popescu et al. [77], UTM mapping was applied to points which were classified by SVM.

In this thesis, we propose a method that is the fusion of the different landmine detection algorithms to improve the detection rate. While fusing the detection algorithms, we try to make use of different features of FLIR image. For this reason, we choose both intensity and texture based features for fusion. We select Trainable Size Contrast Filters based, Corner based, Gaussian Modelling based and Maximally Stable Extremal Regions based landmine detection algorithms which have been explained previously.

CHAPTER 3

FORWARD LOOKING INFRARED IMAGE BASED ANTI-PERSONNEL LANDMINE DETECTION

3.1 Landmine Detection in FLIR Imagery

In FLIR system, the IR camera is mounted on top of the vehicle in forward looking sight of view. The data is collected while vehicle is moving. This system requires large standoff distance and fast rates. The detection phenomenology is the same as IR imagery mentioned before, but has some drawbacks. Because of the position of IR camera, the spatial resolution is lower than downward looking camera [67]. Each pixel has greater spatial information of the surface and extracting anomalous from image becomes tough work. The detection performance of FLIR is lower than DLIR. There is a trade-off between standoff distance and detection performance. In this thesis, we try to optimize and improve the performance of landmine detection by fusing FLIR detection methods.

In Figure 6, the landmine detection operation based on FLIR imagery flow chart is shown. According to Figure 6, the first step is data collection with FLIR camera. FLIR images are extracted from FLIR video and pre-processing step is run to enhance image. The next step is to detect anomalies which are possible landmines and the results of each detection algorithms are fused according to weights. Final step is to convert the image pixel locations into local coordinates and post-processing step removes the locations which are not inside the boundary of detected area.

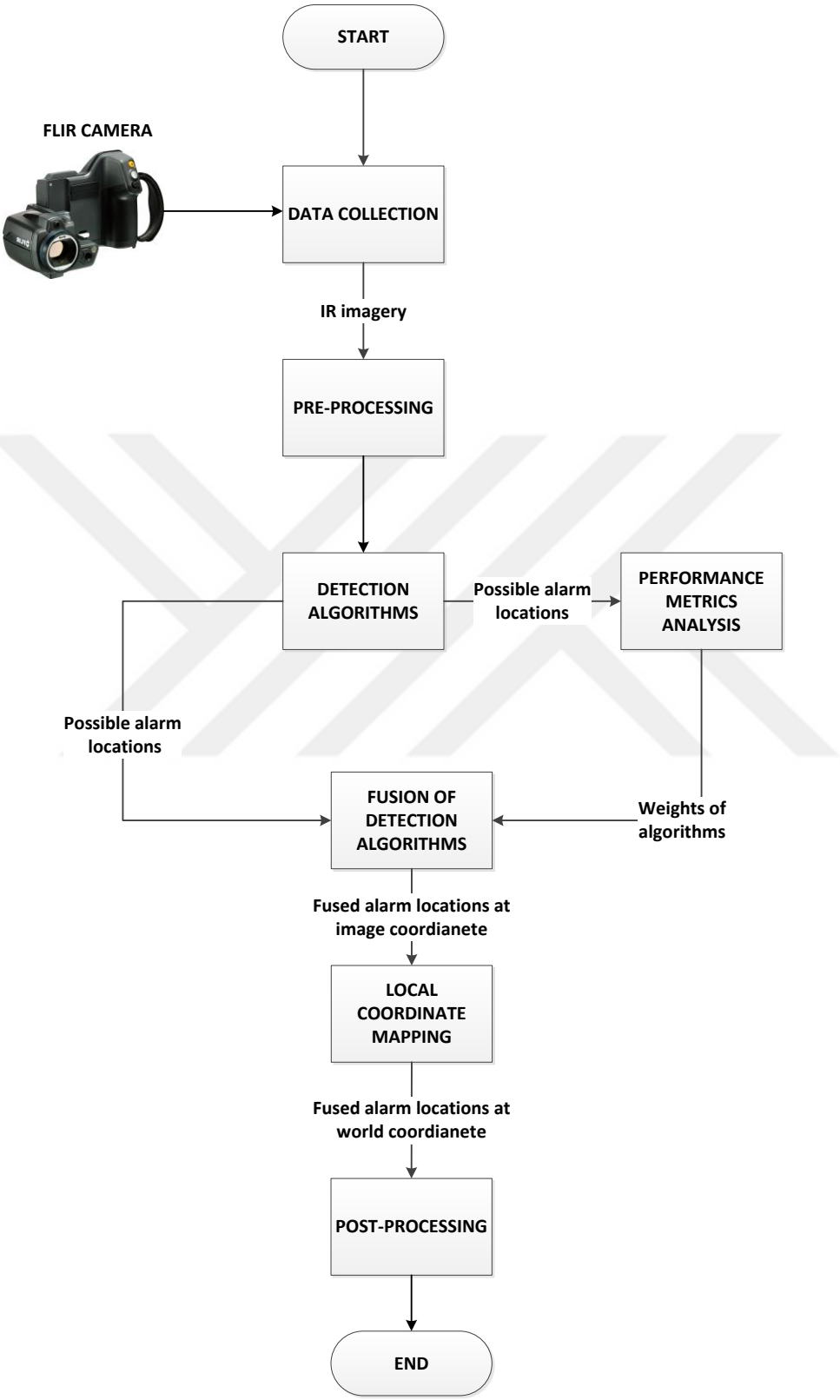

Figure 6 Flow Chart of FLIR Based Landmine Detection Operation

The block diagram corresponding to Figure 6 is given in Figure 7. Infrared image is firstly processed by Contrast Limited Adaptive Histogram Equalization Algorithm. Then, all detection algorithms execute contrast enhanced image and the performances are calculated to find out weights for fusion. Performance metrics and fusion algorithms will be explained in section 3.6 and section 3.7, respectively. Final image domain results are converted into local coordinate locations given detail in section 3.8.

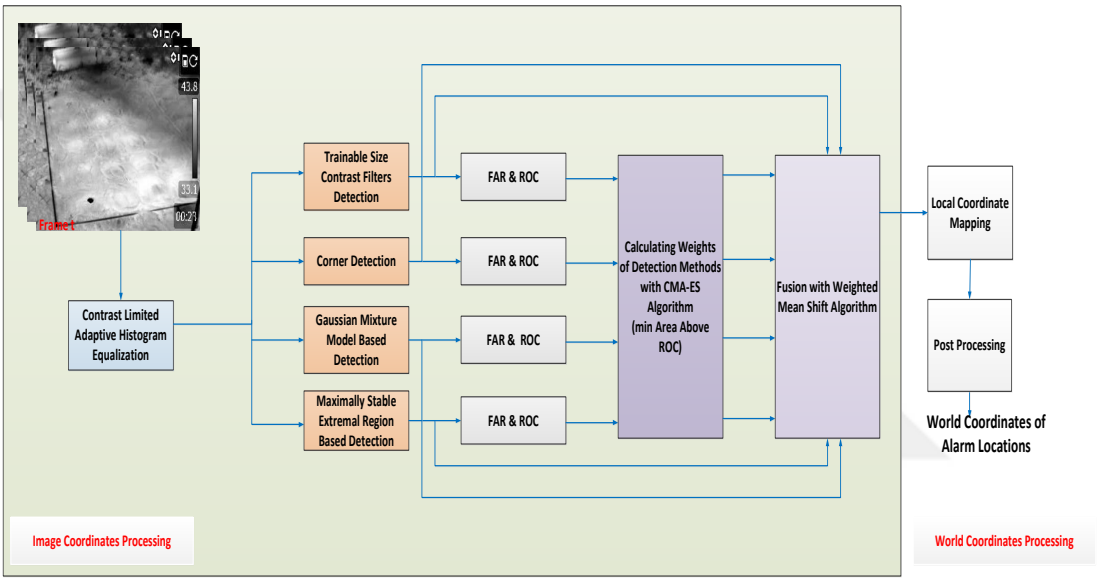

Figure 7 FLIR Based Landmine Detection Block Diagram

3.2 Experimental Test Setup

The data is collected from a sand box (2m x 1.5m) in company test side. Soil is dug and emptied then filled in sand. The FLIR camera is mounted to tripod. The distance from sand box to tripod is 2.5 m. The Field of View (FOV) of camera determines the recorded area. The temperatures of road, soil, weather and landmines define the accuracy of detection algorithms and also reference points, which are taken by local coordinate, determine the registration performance. We prepare our test setup and try to analyze the effects of these situations.

The FLIR T440 series camera is used. It is LWIR camera with 7.5-13 μm spectral range. The IR image is captured with a 320x240 resolution and frame rate is 60 Hz. The FLIR camera properties are given Table 3.

Table 3 T440 FLIR Camera Properties

T440 FLIR Camera Properties	
Spectral Range	7.5 to 13µm
Temperature Range	-20°C to 1200°C (-4°F to 2192°F)
Thermal Resolution	76,800 (320x240)
Thermal Sensitivity	<0.03 °C @ 30 °C
Accuracy	(+/-1°C) (+/-1.8°F) or +/-1% of reading for limited temperature range; ±2°C (±3.6°F) or 2%, whichever C14:C15s greater, at 25°C (77°F) nominal
Frame Rate	60 Hz
Built in Visual Camera	3.1 MP
FOV	25° x 19° / 0.4m / Field of View match where digital image FOV adapts to the IR lens

The role of reflected light is important for IR imagery. The relation is shown Figure 8. The received radiance L_R [$Wm^{-2}sr^{-1}$] at IR sensor [79] can be written as equation (1).

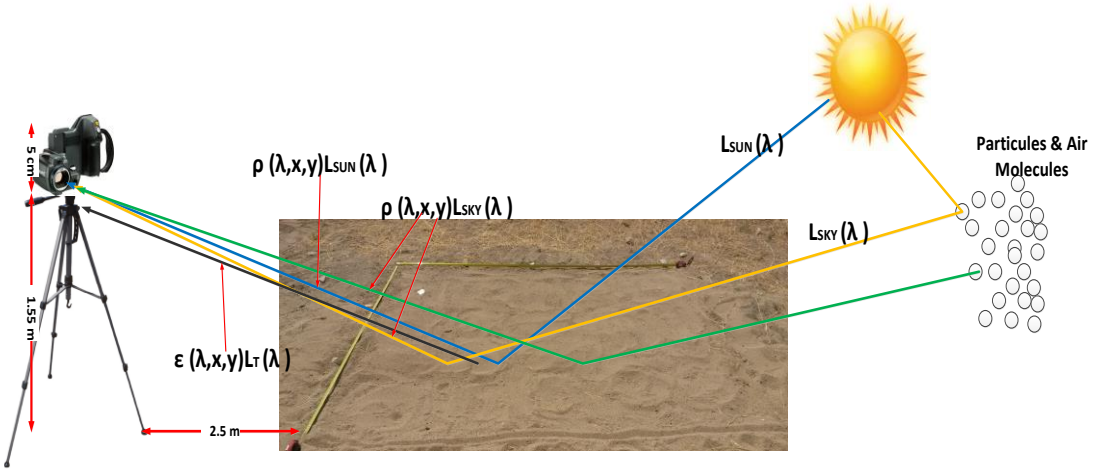

Figure 8 The Received Radiance at FLIR Camera from Atmosphere and Soil

$$L_R(\lambda,x,y) = \rho(\lambda,x,y)L_{SUN}(\lambda,x,y) + \rho(\lambda,x,y)L_{SKY}(\lambda,x,y) + \varepsilon(\lambda,x,y)\,L_T(\lambda,x,y) \quad (1)$$

Where ρ is the surface reflectivity, ε is the surface emissivity, L_{SUN} is the radiance due to sunlight, L_{SKY} is the radiance due to sky light (sunlight scattered by particles and molecules in the earth's atmosphere and thermal radiation from the warm atmosphere), L_T is the thermal radiance and λ is wavelength. According to this point of view, the emissivity and reflectivity of sand includes critical information. Table 4 indicates the properties of sand with different humidity rate [71]. Wet soil has higher emissivity value compared to dry soil. On the other hand, reflectivity equals to 1-emissivity. Rise at emissivity causes fall in the reflectivity which is the other positively affected parameter for received radiance.

Table 4 Properties of Sand with Different Humidity Rate

Soil Type	Emissivity
Sand	0.76
Dry Soil	0.92
Frozen Soil	0.93
Wet Soil	0.95
Limestone	0.95

Figure 9, Figure 10 and Figure 11 show the characterization of dry, moist and wet sand with respect to 2 to 20 μm [72].

In our system, long-wave infrared wavelength is 8-14 μm. 8 μm wavelength corresponds to 1250 cm^{-1} wavenumber and 14 μm wavelength corresponds to 714.29 cm^{-1} wavenumber. As seen in Figure 9, Figure 10 and Figure 11, reflectance increases between these wavelengths. Increasing reflectance is also increasing the received radiance according to equation (1). The reason for choosing the long-wave infrared in imagery is to get high received radiance value at camera and enhance the detection.

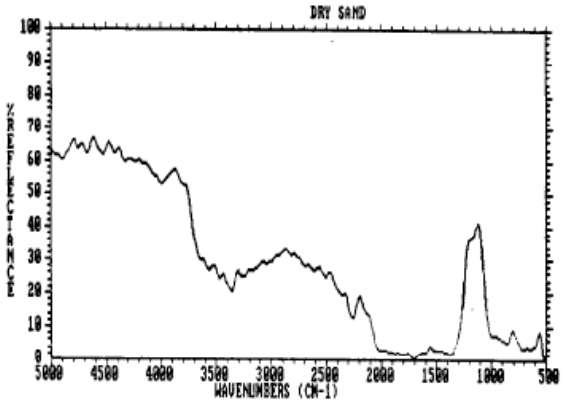

Figure 9 Dry Sand Reflectance between 2-20µm

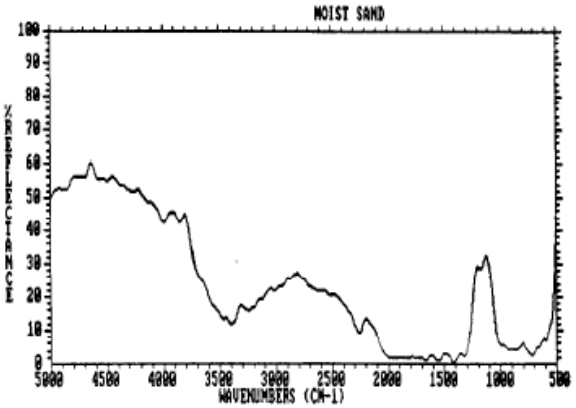

Figure 10 Moist Sand Reflectance between 2-20µm

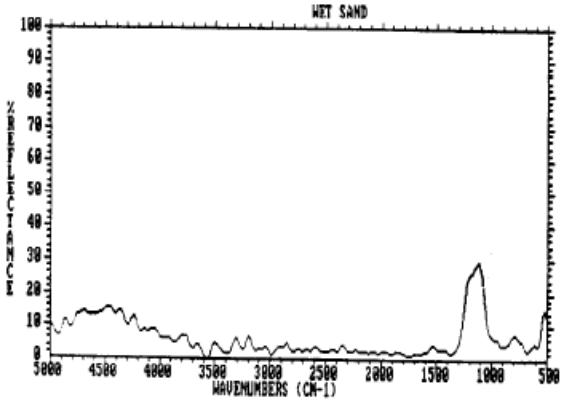

Figure 11 Wet Sand Reflectance between 2-20µm

Table 5 describes our test setup. We record 6 runs in a day and test lasts 5 days. The beginning of test is at 18 August 2016, and we continue test at 19, 20, 23, and 24th of August. During the day, we choose morning and afternoon hours such as 8:20, 10:30, 12:07, 14:50, 16:53 and 18:00. We compare the effects of changing of diurnal daylight on imagery. The camera is fixed to tripod, so we take videos in one direction. Additionally, weather is clear first 3 days, however, weather is rainy at evenings at last 2 days.

Table 5 Test Setup Requirements

Runs	6 runs
Collection Period	Span of 5 days
Times of day	Morning and afternoon
Directions	One direction
Weather	Clear for first 3 days, however rainy for last 2 days at evenings
Number of Targets	12 buried explosive hazards varying in metal content, 3 clutters
Target Depths	Between 0 - 5 cm

We buried dummy 12 explosive hazards and 3 clutters to sand box. 12 dummy anti-personal landmines were produced for analysis of the effects of depth variance, diameter variance, and metal density variance. While defining the target depth, we search the maximum depth size to detect a significant thermal signature of a mine at the surface. The maximum burial depth of most soil types is 10 cm for anti-personnel landmine. After determining depth size, we investigate the generally used mine types and their dimensions. Anti-personnel mines (APM) have smaller size such as 35-120 mm in diameter and 40-120 mm in height. As in Figure 12, PMN-1 has dimensions as diameter 112 mm and height 57 mm and PMN-2 has dimensions as diameter 120 mm and height 53 mm.

Figure 12 PMN-1 and PMN-2 Anti-Personnel Landmines

Table 6 indicates the dimensions of example landmines and real landmines. Our reference is the real landmines while we are deciding the dimensions for mock-up landmines.

Table 6 Example and Real Landmine Dimensions

Example Mine					Anti-Personnel Mine		
Diameter	Height	Aluminium Weight	Polyoxymethylene (POM) Weight	Weight Ratio	Mine Type	Diameter	Height
50 mm	100 mm	37g x 2	75g	1:1	PMM-1	54 mm	103 mm
35 mm	100 mm	37g x 2	75g	1:1	PMP	36 mm	120 mm
65 mm	100 mm	57g x 2	114g	1:1	PMA-2	68 mm	61 mm
80 mm	100 mm	85g x 2	170g	1:1	NR-15	88 mm	65 mm
100 mm	100 mm	135g x 2	265g	1:1	PMC	100 mm	100 mm
100 mm	100 mm	62,5g x 2	240g	1:2			
100 mm	100 mm	240g x 2	240g	2:1			
100 mm	100 mm	2.7kg					
100 mm	100 mm		305g				

The materials used for mock-up mines are Aluminium and Polyoxymethylene (POM) known as Dervin in commercial. The density of Aluminium and POM is 2.7g/cm^3 and 1.410-1.420g/cm^3, respectively. The density of materials is critical to arrange the ratio of weight. The mine types that we use the size are referenced as in [75].

The samples of landmines are shown in Figure 13. There are 13 different anti-personnel landmines mock-up. Our aim is to observe the effects of different depth size, diameter and metal-plastic ratio on IR imagery. We bury landmines in Figure 13 according to location in Figure 14.

Figure 13 Landmines and Clutter Examples Used in Experiment

As a next step after defining burial depth and mine sizes, we create our test setup. According to our previous results, 4 mines are produced diameter with 5 cm and buried to variable depth, 4 mines are produced variable diameter between 3.5 cm to 10 cm and buried to fix 3 cm finally the last 4 mines are produced variable metal density and buried to fix 3 cm below ground. Metal, pet, glass bottles and stone are used as clutter and buried to 3cm depth. Empty line is also placed to evaluate effects during days. Figure 14 shows the location of landmines and clutters with the distance between them.

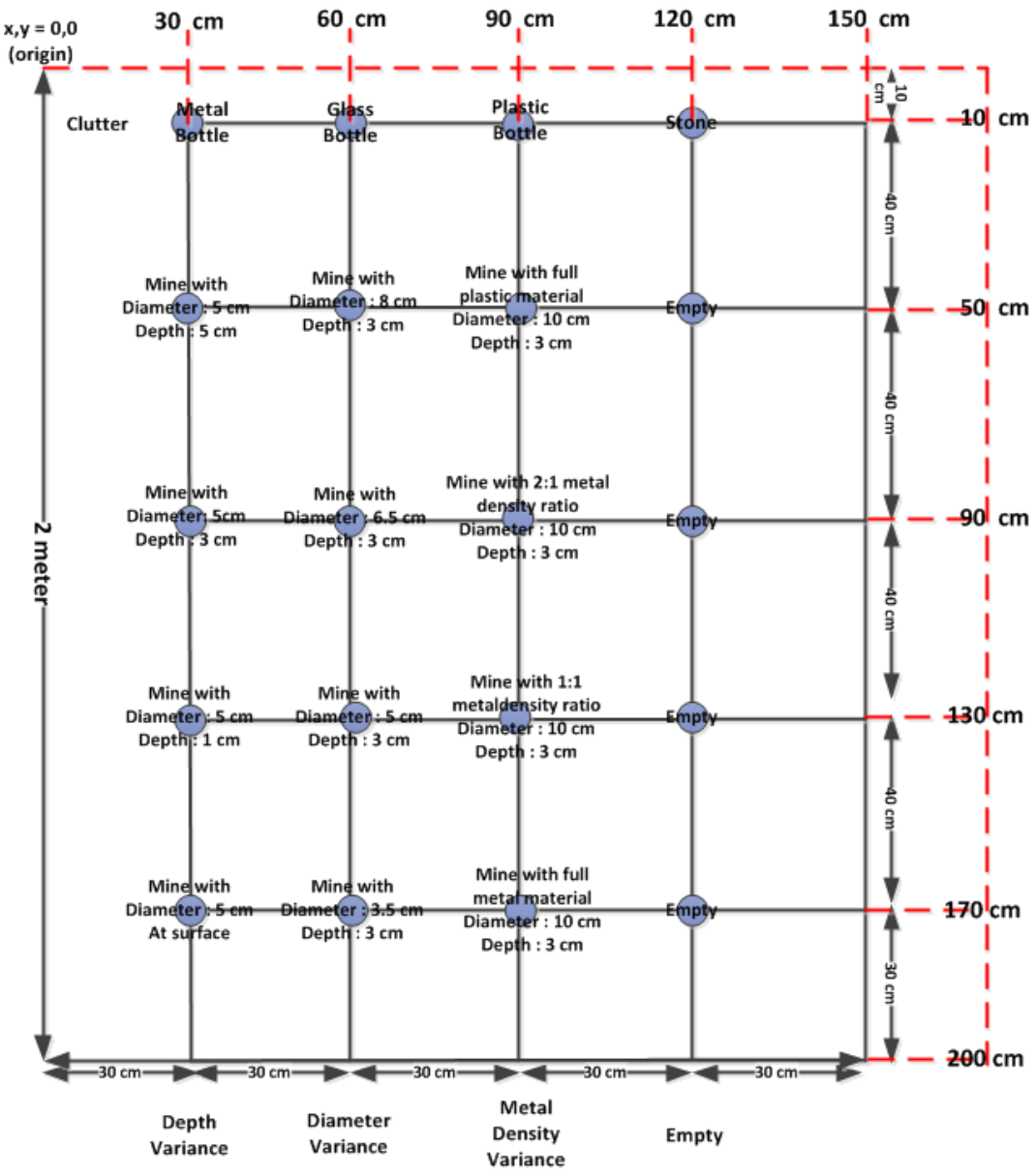

Figure 14 FLIR Imagery Setup for Detection of Anti-Personal Landmine

The final test setup after buried all materials is shown figure below. Camera Calibration process is required for conversion into image domain pixel locations to local coordinate positions. Instead of GPS, we specify 7 locations with meters such as (0,0)cm, (0,50) cm, (0,100) cm, (50,0) cm, (100,0) cm, (150,0) cm and (200,0) cm. The rocks are shown cooler in IR image and pixels corresponding to rocks are found for calibration. We use our local coordinate system for calibration process.

Figure 15 Final Experimental Test Setup View

3.3 Data Collection

Data set are collected during 5 days and runs are at hours 8:20, 10:30, 12:07, 14:50, 16:53 and 18:00. Each video is recorded 10 minutes. The frame rate of the IR camera is 60 Hz, so there are 36000 frames for each sample video. We record 6 runs in a day and we continue our test 5 days. Total frames are calculated as 5x6x36000 for our experiment. In our setup, the camera is fixed and sample videos are recorded at the same direction during recording. There is no motion so we can observe only temperature changes during 10 minutes at fixed area. For our detection algorithms, we use 10 different frames in each recorded sample video and we prepare set of frames for both train and test. We create as a train set from sample video taken at 16:53 and test sets from sample videos taken at 10:30 and 18:00. The performance metrics for both train and test sets are calculated based on 10 frames. We will give detail information about train and test sets at section 4.

The diurnal temperature is very important and affects mine and sand temperature relation during day. The temperature relation between mine, sand and atmosphere is given Table 7 and Figure 16. Earth temperature increases dramatically compared to atmosphere and mine temperatures. After midday, atmosphere temperature rises slowly and mine temperature continues increasing until 3 pm. However, earth

temperature starts decreasing after midday. At the end of the day, they reach settle point at 6 pm.

Table 7 Diurnal Temperature Variation

Hour	Earth Temperature (°C)	Mine Temperature(°C)	Atmospheric Temperature(°C)
08:20	25,0	22,9	20
12:07	51,9	25,8	30
14:50	48,8	36,6	31
16:53	42,0	33,2	32
18:00	35,0	32,7	32

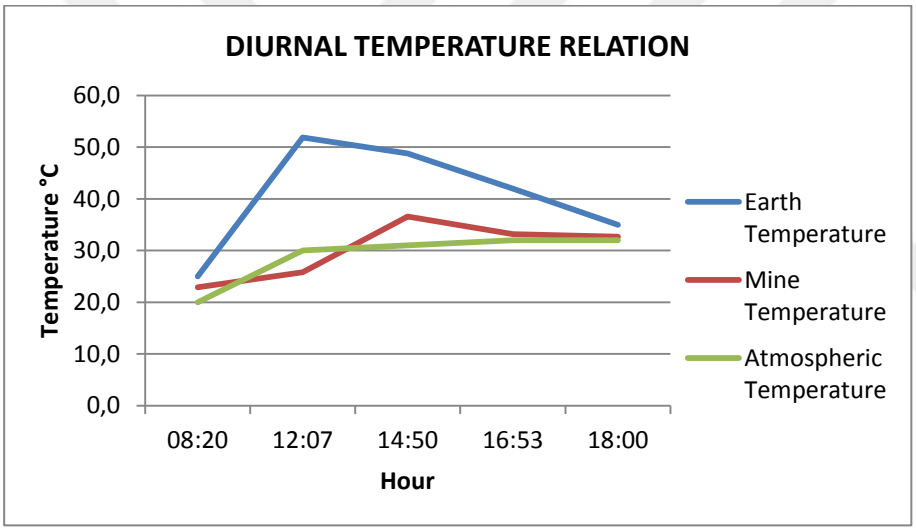

Figure 16 Diurnal Temperature Relation

Example images taken by FLIR T440 series camera from Electro-Optics (EO) and Infrared (IR) sensors are shown Figure 17 and Figure 18, respectively. The borders are defied by ruler and reference points are specified by stones. As seen in Figure 17, we put stones at location (0,0), (50,0), (100,0), (150,0), (200,0), (200,50) cm. These stones locations are used as reference points for registration. In Figure 18, we choose 3 locations to observe temperature changes during the day. Table 7 is extracted from these recording.

Figure 17 Example EO Frame taken by FLIR T440

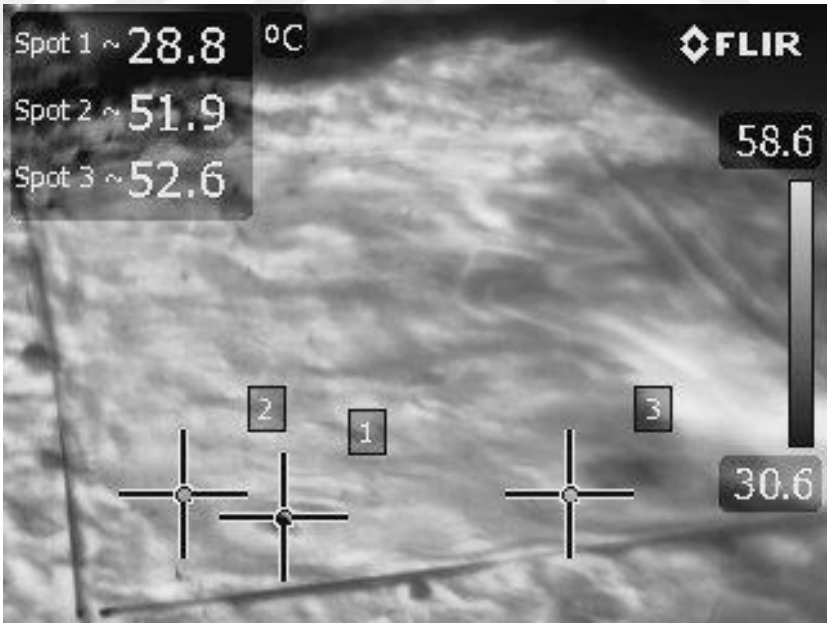

Figure 18 Example IR Frame Taken by FLIR T440

The diurnal changings affect the temperature of landmines. Figure 19 is captured at 12:00 and Figure 20 is captured at 18:00. At morning, sand gets warm faster than landmine; so landmine is seen darker. On the other hand, sand gets cold faster than

landmine; so landmine is seen brighter at afternoon. In our IR image, there is a landmine with full metal density at shown location. Therefore, the variations could be seen obviously. These results also match with Figure 16.

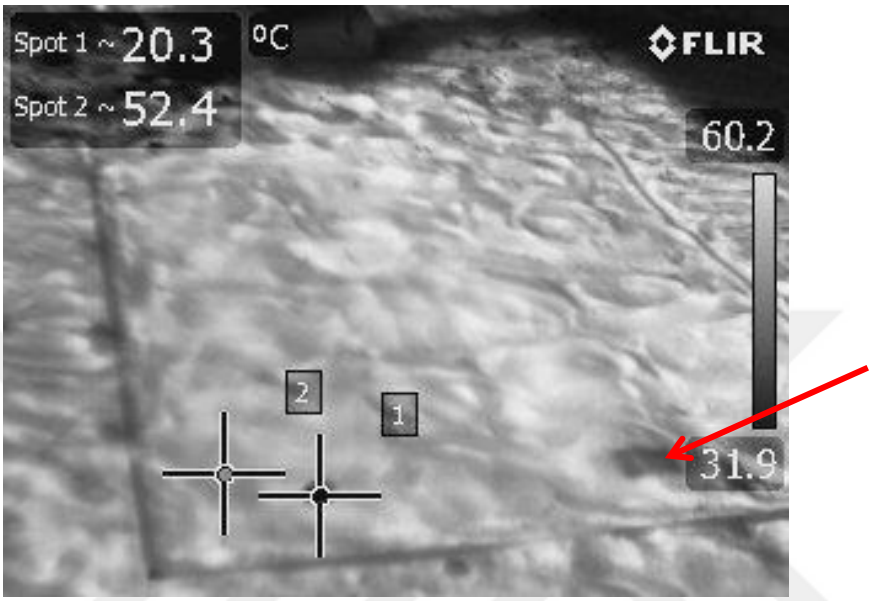

Figure 19 Example FLIR Frame taken at 12:00

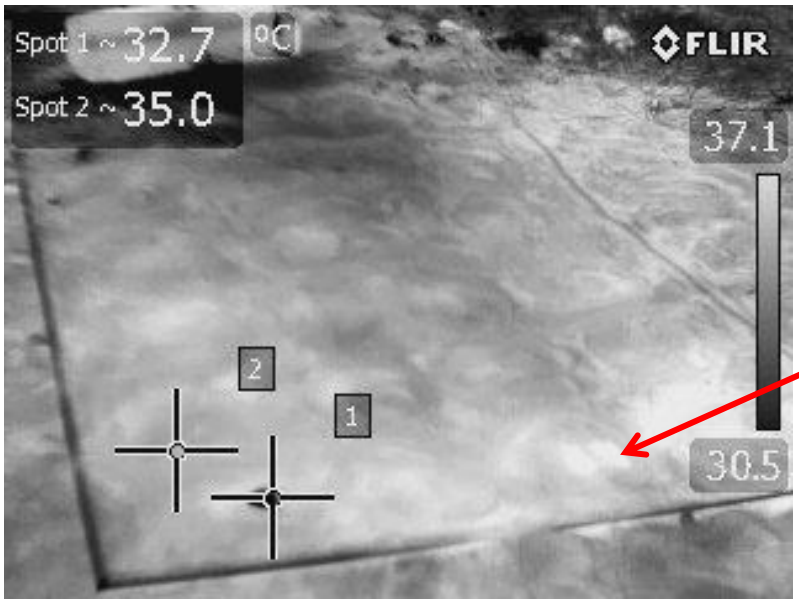

Figure 20 Example FLIR Frame Taken at 18:00

3.4 Pre-Processing of IR Imagery

3.4.1 Adaptive Histogram Equalization Algorithm

Histogram equalization techniques are conventional enhancement techniques for image processing. In FLIR perspective yields that closer regions are brighter than further regions. To remove intensity mismatch between closer and further area in the same frame and to increase detection area with greater standoff distance, Contrast Limited Adaptive Histogram Equalization (CLAHE) algorithm is applied to frame as a pre-processing method. CLAHE algorithm is based on Histogram Equalization (HE) algorithm which is defined as following equations.

For a give image $X = \{X(i, j)\}$ with L discrete gray levels such as $\{X_0, X_1, \ldots, X_{L-1}\}$, the probability density function can be written as equation (2).

$$p(X_k) = \frac{N_k}{N} \quad \text{for k=0,1,...,L-1} \tag{2}$$

where N_k is the number of times the level X_k appears in the input image and N is the total number of input image. Gray levels are denoted as L (L=256). Then, the cumulative density function c(x) is calculated as in (3);

$$c(X_k) = \sum_{j=0}^{k} p(X_j) \quad \text{for k=0,1,...,L-1} \tag{3}$$

The input image is mapped into the entire dynamic range (X_0, X_{L-1}) in histogram equalization process. The cumulative density function is used as a transform function and the transformation is indicated in equation (4).

$$f(x) = X_0 + (X_{L-1} - X_0).c(x) \tag{4}$$

where (X_{L-1}) is the maximum and (X_0) is minimum gray level. The corresponding output image after histogram equalization process is expressed as equation (5).

$$Y = f(x) = \{f(X(i, j)) \mid \forall X(i, j) \in X\} \tag{5}$$

where (i,j) represents the spatial coordinates of the pixel in the image.

The aim of histogram equalization method is that the high histogram regions are stretched and the low histogram regions are compressed. In that case, if the target area which should be detected is occupied a small portion in the image, and then it is not enhanced after histogram equalization. To overcome this problem, histogram is modified by clipping a threshold limit before the process of equalization. This method is called as Contrast Limited Adaptive Histogram Equalization (CLAHE) algorithm. The clipping limit is defined as equation (6).

$$\text{Clip limit} = \left[\frac{\varphi}{256}\right] + \left[\beta.\left(\varphi - \frac{\varphi}{256}\right)\right] \quad (6)$$

where β is the clipping enhancement parameter

[.] is the truncating the value to the nearest integer

φ is the product block size

256 is the number of bins (0-255).

The limit value in CLAHE method is critical parameter. Higher values for clip limit results more contrast image. The optimum parameter should be selected for FLIR imagery.

3.5 Landmine Detection Algorithms

In this thesis, we propose a method that is the fusion of the different landmine detection algorithms to improve the detection rate. While fusing the detection algorithms, we try to make use of different features of FLIR image. For this reason, we choose both intensity and texture based features for fusion. We select Trainable Size Contrast Filters based, Corner based, Gaussian Modelling based and Maximally Stable Extremal Regions based landmine detection algorithms and we will give detail information about these algorithms in next sections.

3.5.1 Trainable Size Contrast Filters Based Landmine Detection

Trainable Size Contrast Filters detection [15] is the first detection method that we implement. There are two windows called as inner and outer window. The difference between two windows is calculated at every pixel location. If the difference is higher than the threshold, then an anomalous is recorded at that location. The outer window represents the local background while inner window corresponds to anomalous if there is one. There are some parameters which represent inner and outer window size. Inner window vertical and horizontal radiuses are called as wsize_v and wsize_h respectively. Outer window vertical and horizontal paddings are called as pad_v and pad_h respectively. The range of wsize is [1, 64] and the range of pad is [1, 32]. This range changes according to resolution and target size. After defining the windows, the decision on which type of distance measurements for similarity is critical. On the assumption that if the variance of inner window is not affected the result (near outer window variance), mean brightness of two windows can be compared with the outer window variance. Taking the difference of mean values to ensure anomalous and dividing by outer window variance gives the square of Mahalanobis Distance indicated in equation(7).

$$D_M(p,q)=\sqrt{\frac{(\mu_p-\mu_q)^2}{\sigma^2}} \qquad (7)$$

Where μ_p : the mean value of inner window

μ_q : the mean value of outer window

σ^2 : the variance of outer window

In equation(7), if the outer window variance is high then the result will be small and there is no anomalous. If the outer window variance is small then mean differences is important.

In Mahalanobis Distance, the inner window variance is not taken into account so unexpected results can be occurred. For example, the outer window variance is very high where inner window variance is very low that means the gray scale line

surrounding with black and white pixels, the result will be no anomalous in Mahalanobis Distance measure. However, there is a target which should be detected. Bhattacharya Distance is taken into account both inner and outer window mean and variance values.

$$D_B(p,q)=\frac{(\mu_p-\mu_q)^2}{4(\sigma_p^2+\sigma_q^2)}+0.5*\ln\left(\frac{\sigma_p^2+\sigma_q^2}{2\sqrt{\sigma_p^2\sigma_q^2}}\right) \quad (8)$$

Where μ_p : the mean value of inner window

μ_q : the mean value of outer window

σ_p^2 : the variance of inner window

σ_q^2 : the variance of outer window

In some cases, windows have similar means with different variances. Equation (7) goes to zero in Mahalanobis distance; however, equation (8) tends to grow according to variance difference in Bhattacharya distance. Bhattacharya distance gives more realistic results. In algorithm implementation, we require six parameters. Four parameters define windows size and two parameters define thresholds for distances.

3.5.2 Corner Based Landmine Detection

The critical information is extracted from corners that can be essential for the identification studies. There are many areas in video processing which utilize in detection of corners, stereo matching, object recognition and tracking [62]. In our application, we aim to detect landmines locations using corner features [59].

Corner detection algorithm, which is based on single-scale, works very well if the image has similar-size features. FLIR image contains multi-scale features because of the angle of LWIR camera. The position of the camera mounted top of the vehicle results perspective seen in the image. Hence, multi scale algorithm based on curvature scale space (CSS) algorithm is used to detect corners of landmine [60]. The steps of CSS algorithms are explained in sub-sections.

3.5.2.1 Canny Edge Detection

The first step of CSS algorithm is that Canny edge detection is applied to each IR image. Canny edge detector, which is one of the edge detector algorithms, contains multi stage process.

a. Gaussian filter is applied to IR image to remove noise. Noise causes false corners in an image and affects the edge detection. To reduce effects of noise on detection, the image is smoothed by Gaussian filter [68]. 2D continuous Gaussian function is described as;

$$G(x,y) = \frac{1}{2\pi\sigma^2} e^{-\frac{x^2+y^2}{2\sigma^2}} \quad (9)$$

Where σ : variance

In discrete domain, the Gaussian filter is calculated in (10).

$$H_{Gij} = \frac{1}{2\pi\sigma^2} \exp\left(-\frac{(i-(k+1))^2 + (j-(k+1))^2}{2\sigma^2} \right) \quad ; \ 1 \le i,j \le (2k+1), \quad (10)$$

Where the Gaussian filter kernel size is $(2k+1)\times(2k+1)$ and i,j: discrete pixel location.

If the size of Gaussian filter is 5×5 with σ = 1.4, then kernel equals to (11).

$$H = \frac{1}{159}\begin{bmatrix} 2 & 4 & 5 & 4 & 2 \\ 4 & 9 & 12 & 9 & 4 \\ 5 & 12 & 15 & 12 & 5 \\ 4 & 9 & 12 & 9 & 4 \\ 2 & 4 & 5 & 4 & 2 \end{bmatrix} \quad (11)$$

b. The most intensity changing in gray scale image gives the edges in the Canny algorithm. These locations are found by taking gradient of filtered image in horizontal and vertical directions. G_x and Gy are the first derivative in the horizontal and vertical direction respectively. Edge gradient magnitude and direction are calculated as;

$$|G| = \sqrt{G_x^2 + G_y^2} \quad , \quad \Theta = \arctan 2\left(G_y, G_x\right) \tag{12}$$

Where the magnitude of gradient $|G|$ is the Euclidean distance and the edge direction angle, which is the perpendicular to edge, is limited as $0^\circ, 45^\circ, 90^\circ$ and 135°.

Sobel operator is one of the edge detection operators that used in implementation and the kernel of Sobel operator is described in [68].

$$K_{GX} = \begin{bmatrix} -1 & 0 & 1 \\ -2 & 0 & 2 \\ -1 & 0 & 1 \end{bmatrix} \quad \text{and} \quad K_{GY} = \begin{bmatrix} 1 & 2 & 1 \\ 0 & 0 & 0 \\ -1 & -2 & -1 \end{bmatrix} \tag{13}$$

Filtered image is convolved by both K_{GX} and K_{GY}. Then, equation (12) is calculated to find gradients of IR image.

c. The third step in Canny algorithm is the non-maximum suppression algorithm which is an edge thinning technique. The goal of this step is to obtain more sharp edges. The idea is that all gradient directions are rounded to $0^\circ, 45^\circ, 90^\circ$ and 135° and then the current pixel's edge strength is compared to the pixel gradient strengths which are the positive and negative gradient directions. Whole local maxima values are preserved and the others are removed.

d. After non-maxima suppression, still some edge pixels caused by noise exist. Double thresholding method is applied to separate weak edge to strong edge. They are called as low threshold and high threshold values. If the pixel value is higher than the high threshold value then it is called as strong edge. If the pixel value is lower than the low threshold value then it is called as weak edge.

e. Final step for Canny edge detector is the edge tracking by hysteresis. Strong edges can be assigned directly as true edges. If weak edges are connected to strong edges then they are added as true edges, otherwise, they are removed.

3.5.2.2 Corner Detection and False Edge Removal

After applying Canny edge detector, edge contours are extracted from edge map and if there is a gap between edges, the gap is filled until that end point of edge is nearly connected to another end point of edge. The close contour curves are selected for landmine detection. The corners of identified contours are computed. There are many false corners which are eliminated according to the average curvature, corner angle and axes ratio of inscribed ellipse [62].

To identify corners, curvature of contours is calculated. Curvature gives information about the sharpness of a curve. Curvature is defined as the magnitude of the rate of change "ψ" with respect to the distance "s" moved along the curve. Figure 21 expresses curvature.

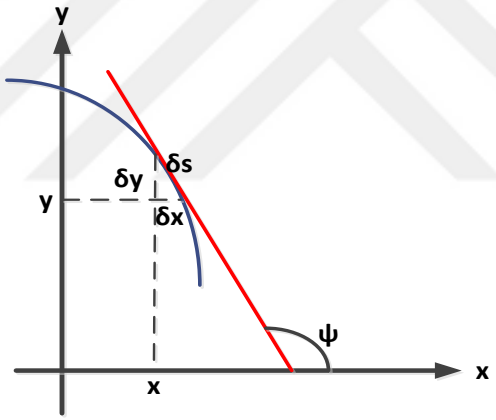

Figure 21 Curvature Expression

If curvature is denoted as κ (kappa), Equation (14) below identifies this relation.

$$\kappa = \left| \frac{d\psi}{ds} \right| \tag{14}$$

Equation (14) above can be converted more familiar form to equation (15).

$$\frac{d\psi}{ds} = \frac{d\psi}{dx}\frac{dx}{ds} = \frac{d\psi}{dx} / \left(\frac{ds}{dx} \right) \tag{15}$$

δx and δy denote small increments in the x and y directions, respectively. In Figure 21, there is a small triangle with hypotenuse δs which is the arc-length along the curve. From Phytagoras' theorem:

$$\left(\frac{\delta s}{\delta x}\right)^2 = 1 + \left(\frac{\delta y}{\delta x}\right)^2 \text{ so that } \frac{\delta s}{\delta x} = \sqrt{1 + \left(\frac{\delta y}{\delta x}\right)^2} \tag{16}$$

If the increments get smaller, the relation can be written in derivative form.

$$\frac{ds}{dx} = \sqrt{1 + \left(\frac{dy}{dx}\right)^2} \tag{17}$$

As $y = f(x)$, equation (17) turns into equation (18).

$$\frac{ds}{dx} = \sqrt{1 + \left(\frac{df}{dx}\right)^2} = (1 + |f'(x)|^2)^{1/2} \tag{18}$$

The relation between the angle ψ and derivative of f'(x) is

$$\frac{df}{dx} = \tan\psi \tag{19}$$

Second order derivative can be written as equation (20).

$$\frac{d^2f}{dx^2} = \sec^2\psi \frac{d\psi}{dx} = (1 + \tan^2\psi)\frac{d\psi}{dx} = (1 + [f'(x)]^2)\frac{d\psi}{dx} \tag{20}$$

When we invert equation (20),

$$\frac{d\psi}{dx} = \frac{f''(x)}{(1 + [f'(x)]^2)} \tag{21}$$

So, finally curvature can be calculated as equation (22).

$$\kappa = \left|\frac{d\psi}{ds}\right| = \left|\frac{d\psi}{dx} / \left(\frac{ds}{dx}\right)\right| = \left|\frac{f''(x)}{(1 + [f'(x)]^2)^{3/2}}\right| \tag{22}$$

Basically, $\frac{dy}{dx} = \frac{\dot{y}}{\dot{x}}$ and $\frac{d^2y}{dx^2} \doteq \frac{\dot{x}\ddot{y} - \dot{y}\ddot{x}}{\dot{x}^3}$ where $\dot{x} = \frac{dx}{dt}$ and $\ddot{x} = \frac{d^2x}{dt^2}$

Then, curvature κ can be formed into equation (23).

$$\kappa = \left| \frac{f''(x)}{(1 + [f'(x)]^2)^{3/2}} \right| = \left| \frac{\dot{x}\ddot{y} - \dot{y}\ddot{x}}{\dot{x}^3 \left[1 + \left(\frac{\dot{y}}{\dot{x}} \right)^2 \right]^{3/2}} \right| = \left| \frac{\dot{x}\ddot{y} - \dot{y}\ddot{x}}{\left[\dot{x}^2 + \dot{y}^2 \right]^{3/2}} \right| \quad (23)$$

In our curvature calculation, we use final basic formulation. After we find curvature, we calculate local maxima which are the corners of contours.

The total parameters that are used in implementation are:

H: the high threshold value of Canny edge detector

L: the low threshold value of Canny edge detector

L=0 and H=[0.15,0.35]

C: the axes ratio of corner inscribed ellipse. C=1.5

T: maximum angle of corner. T=160

Endpoint: assigned as whether endpoint of contour or not. Endpoint = 0

Gap_size: required number of pixels to close to contour.

3.5.3 Gaussian Model-Based Landmine Detection

Gaussian Model (GM) [58] is one of the landmine detection methods that have been used for modelling foreground/background. In this algorithm, each pixel is assigned as a mixture of Gaussian distributions [58]. If new pixel is added, then these distributions are updated. For each frame, the histogram of IR image is calculated and Gaussian curve is fitted to this histogram. The mean and variance of the histogram are estimated while fitting the Gaussian curve.

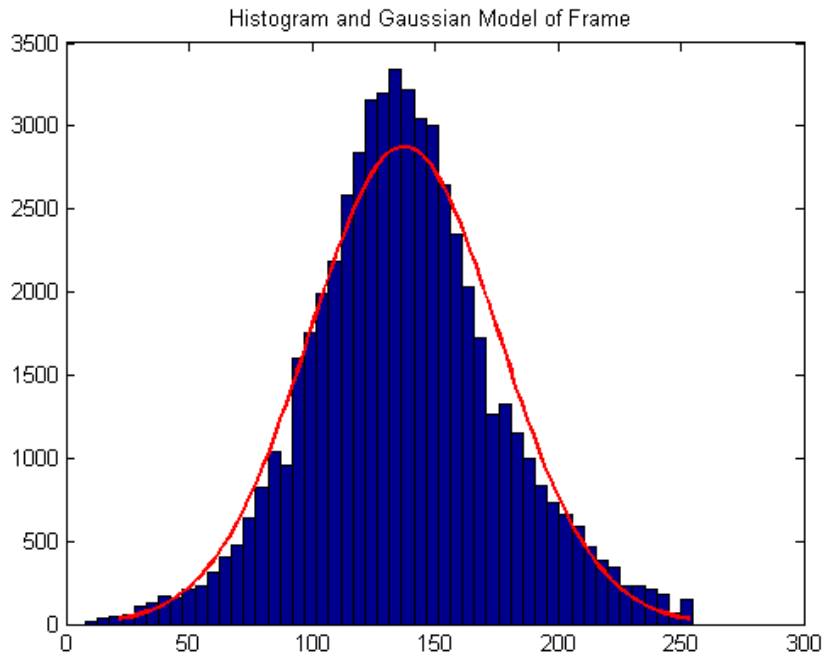

Figure 22 Histogram of Train IR Image

Foreground/background (1/0) modelling is a type of binary function and defined as FG(x,y);

$$FG(x,y) = \begin{cases} 1, & |I_t(x,y) - \mu(x,y)| > 2.5\sigma \\ 0, & \text{else} \end{cases} \quad (24)$$

Where $I_t(x,y)$: the pixel value at location (x,y) at frame t

$\mu(x,y)$: the mean of Gaussian background model at pixel location (x,y)

σ :standard deviation

According to equation (24), if new pixel value is outside 2.5 standard deviations of the background, then it is called as foreground and labelled as '1'. Otherwise, it is called as background and labelled as '0'.

After labelling, Weighted Mean-Shift algorithm and coordinate conversion are applied to find center location of landmines in local coordinate as explained in section 3.7.2 and section 3.8 respectively.

3.5.4 Maximally Stable Extremal Region Based Landmine Detection

Maximally Stable Extremal Region (MSER) [63] algorithm is a technique which used in detection of buried landmines in LWIR image. As an informal definition, MSERs are blobs that are either darker or brighter regions compared to surroundings. Additionally, blobs are stable within the range of threshold. In formal definition, Extremal Regions are defined by Matas et al. [63] as the image regions which are formed by contiguous pixels and these pixels are spatially connected and possess similar threshold intensity. After detection of ERs, each ERs compared to stability factor to find the Maximally Stable ER (MSER)s. Resulting blobs indicate possible landmine locations in LWIR imagery.

Image: Let image I be mapping $I : D \subset Z^2 \rightarrow \{0,1,\ldots,255\}$ which is totally ordered, i.e. reflective, antisymmetric and transitive binary relation. This is required for ERs and the next requirement for ERs is a **neighbourhood (spatial adjacency) relation** defined as $A \subset D \times D$

e.g. 4-neighbors spatial adjacency,

$$p,q \in D \text{ are adjacent (pAq) iff } \sum_{i=1}^{d} |p_i - q_i| \leq 1 \qquad (25)$$

Region: Region R is the subset of D such that for each $p,q \in D$ there is as sequence $p,a_1,\ldots,a_n,q$ and $pAa_1,\ldots,a_1Aa_{i+1},\ldots,a_nAq,\ a_i \in R$, i.e. region is a connected component in terms of neighbourhood relation A.

Outer Boundary: Outer Boundary is defined as $\partial R = \{q \in D \setminus R : \exists p \in R : qAp\}$ i.e. the boundary ∂R of R is the set of pixels which are adjacent at least one pixel of R but not inside the R.

Extremal Region: Region R is an extremal region E if and only if $E \subset D$ such that $\forall p \in E, \forall q \in \partial E$ and

$$\begin{aligned} &I(p) > I(q) : \text{maximum intensity region or} \\ &I(p) < I(q) : \text{minimum intensity region} \end{aligned} \tag{26}$$

Maximally Stable Extremal Region (MSER): Let $E_1, \ldots, E_{i-1}, E_i, \ldots$ be a sequence of nested extremal regions, i.e. $E_{i-1} \subset E_i$. Extremal region E_{i^*} is maximally stable if and only if

$$q(i) = \left| E_{i+\Delta} \setminus E_{i-\Delta} \right| / \left| E_i \right| \tag{27}$$

has a local minimum at i^* where Δ is the user defined parameter.

Equation (27) defines the measure of the relative change of region area over a fixed number of intensities. The number of pixels $E_{i+\Delta} \setminus E_{i-\Delta}$ in the range of intensities $\langle i - \Delta, i + \Delta \rangle$, which gives the change of region area, called as mixed pixels.

The MSER algorithm is used landmine detection in LWIR imagery, because of the following properties of MSER.

- It is an invariant algorithm to affine transformation called as affine invariance property.
- During image domain transformation, the adjacency is preserving.
- It is also stable, since unchanged regions based on thresholds are selected as extremal regions.
- Multi-scale detection is another property, since MSER detects both very fine and very large blobs in same view.

These properties are important in application because FLIR camera records a video while vehicle is moving. In different frames, the same blob is seen in different angle view and MSER is not affected by affine transformations. Additionally, MSER detects blobs in LWIR imagery. The blobs shapes and brighter/darker appearance depend on distance to vehicle, burial depth and daily whether conditions. In MSER, the point is the stability in blobs so the algorithm is robust to external factors.

MSERs can be denoted as ellipsoids. After finding samples according to MSER algorithm, covariance matrixes of regions are calculated. Firstly, standard deviation, which provides a measure of how much the data is spread across the feature space, is calculated.

The standard deviation in x direction is obtained as in equation (28).

$$\sigma_x^2 = \frac{1}{N-1}\sum_{i=1}^{N}(x_i - \mu)^2 = E[(x - E(x))(x - E(x))] = \sigma(x, x) \qquad (28)$$

The standard deviation in y direction is obtained as in equation (29).

$$\sigma_y^2 = \frac{1}{N-1}\sum_{i=1}^{N}(y_i - \mu)^2 = E[(y - E(y))(y - E(y))] = \sigma(y, y) \qquad (29)$$

The standard deviation in x and y direction is obtained as in equation (30).

$$\sigma_{xy}^2 = = E[(x - E(y))(y - E(y))] = \sigma(x, y) \qquad (30)$$

Where μ is mean value and E defines expected value function.

Therefore, covariance matrix **C** is computed as equation (31).

$$C = \begin{bmatrix} \sigma(x, x) & \sigma(x, y) \\ \sigma(y, x) & \sigma(y, y) \end{bmatrix} \qquad (31)$$

The ellipse axis vectors are obtained as the unit eigenvectors $\mathbf{e}_0$ and $\mathbf{e}_1$ of the matrix of **C** and corresponding eigenvalues are $\lambda_0 > \lambda_1 > 0$ respectively. $\mathbf{e}_0$ is the largest eigenvector with λ_0 largest eigenvalue. Since **C** is a real symmetric matrix, there is an orthonormal basis for $\Re^n$ of eigenvectors of **C**. Each vector's norm is 1 and they are orthogonal with respect to **C** in orthonormal case. This means, $\mathbf{e}_0{}^t C \mathbf{e}_1 = 0$ or $\mathrm{Cov}(\mathbf{e}_1, \mathbf{e}_0) = 0$. Then $\mathrm{Var}(\mathbf{e}) = \lambda \|\mathbf{e}^2\| = \lambda$.

Ellipse is defined as equation (32).

$$\left(\frac{x}{\sigma_x}\right)^2 + \left(\frac{y}{\sigma_y}\right)^2 = s \tag{32}$$

where s defines the scale of ellipse.

s is chosen according to confidence level such that a 95% confidence level corresponds to s=5.991 where the degrees of freedom is 2. In our cases, the degrees of freedom is 2 because, there are two unknowns [69].

As a result, major half axis is defined as $\sqrt{5.991}\sigma_0\mathbf{e}_0$ and the minor half axis is $\sqrt{5.991}\sigma_1\mathbf{e}_1$. Using relation $\mathrm{Var}(\mathbf{e}) = \lambda\|\mathbf{e}^2\| = \lambda$, then the major and minor axis are defined as $\sqrt{5.991\lambda_0}\mathbf{e}_0$ and $\sqrt{5.991\lambda_1}\mathbf{e}_1$ respectively.

The orientation of ellipse is obtained by calculating the angle of the largest eigenvector towards the x-axis.

$$\alpha = \arctan\frac{\mathbf{e}_0(y)}{\mathbf{e}_0(x)} \tag{33}$$

Finally ellipse defined as equation below.

$\text{ellipse} = Q' * R$ where

$$Q = \begin{bmatrix} \sqrt{5.991\lambda_0}\times\cos(\theta) \\ \sqrt{5.991\lambda_1}\times\sin(\theta) \end{bmatrix} \text{ and } R = \begin{bmatrix} \cos(\alpha) & \sin(\alpha) \\ -\sin(\alpha) & \cos(\alpha) \end{bmatrix} \text{ where } \theta : [0, 2\pi] \tag{34}$$

3.6 Performance Metrics of Detection Algorithms

Receiver Operating Characteristics (ROC) curve is a technique to visualize, organize and select the classifiers based on their performance. In detection theory, there is trade-off between hit rate and false alarm rate. ROC curves analyse false positive rate and true positive rate at x and y directions, respectively.

In landmine detection, two classes, which are foreground and background, are classified by anomaly detection algorithms. Each instance is mapped to one element

of the set {**p, n**} of positive and negative class labels. These classes are true classes. With classification algorithms, predicted classes are formed and labelled as {**Y, N**}. The combination of instance and classifier results four possible outcomes [70].

Table 8 Confusion Matrix (Contingency Table)

		True Class	
		p	n
Hypothesized Class	Y	True Positive	False Positive
	N	False Negatives	True Negative

The combination of instance and classifier results four possible outcomes.

Table 8 shows the four possible outcomes. If the instance is positive and if classified as positive, then it is counted as True Positive (TP), if classified as negative then it is classified as False Negative (FN). If the instance is negative and if classified as positive, then it is counted as False Positive (FP), if classified as negative then it is classified as True Negative (TN).

There are some parameters which defines the classifier performance.

True positive rate is also called as hit rate and recall defined as (35),

$$\text{tp rate} \approx \frac{\text{Positives correctly classified}}{\text{Total positives}} = \frac{\text{TP}}{\text{P}} \tag{35}$$

False positive rate is also called false alarm rate defined as (36),

$$\text{fp rate} \approx \frac{\text{Negatives incorrectly classified}}{\text{Total negatives}} = \frac{\text{FP}}{\text{N}} \tag{36}$$

Additional terms associated with ROC curves are expressed in (37).

$$\text{sensitivity} = \text{recall} = \frac{\text{TP}}{\text{P}}$$

$$\text{specifity} = \frac{\text{True negatives}}{\text{False positives + True negatives}} = 1 - \text{fp rate}$$

$$\text{positive predictive value} = \text{precision} = \frac{\text{TP}}{\text{TP} + \text{FP}} \tag{37}$$

$$\text{accuracy} = \frac{\text{TP} + \text{TN}}{\text{P} + \text{N}}$$

$$\text{F} - \text{measure} = \frac{2}{1/\text{precision} + 1/\text{recall}}$$

ROC graph is a two-dimensional graph which plots fp rate on X axis, tp rate on Y axis. At (0,0) location, there is no false positives errors but also no true positives. At (1, 1) defines both true and false positives are the same. (0, 1) point represents the perfect classification. Increasing the area under ROC gives better classification.

3.7 Fusion Algorithms

In this thesis, fusion of detection algorithms is examined to increase accuracy and detection performance. Mean Shift and Weighted Mean Shift algorithms are implemented in this section. There results a set of discrete samples after landmine detection algorithms. We need to find local maxima of a density function given a set of discrete samples. Mean shift algorithm is well known method finding local maxima according to [15]. That so; we use weighted mean shift algorithm as a fusion technique for locating local maxima resulted samples which are outcomes of each detection algorithm.

3.7.1 Mean Shift Algorithm

After image is processed by detection algorithms, bright or dark blobs are formed. Mean-Shift algorithm is applied data in image space to locate peaks. Mean-Shift method aims to locate maxima of density function given a set of discrete samples iteratively. The mean shifted pixel locations of blobs are projected into local coordinates as explained in section 3.8. The procedure is based on gradient ascent algorithm with the kernel density estimator [15]. Equation (38) gives the general formula.

$$\hat{f}(x) = \frac{1}{nh}\sum_{i=1}^{N} K\left(\frac{x - x_i}{h}\right) \tag{38}$$

Where K : Kernel function (a symmetric function that integrates to one);

h : Variance in Window Size

N : Number of data points

The gradient of (38) with respect to x is taken and equalized to zero, then (39) results.

$$x = \frac{\sum_{i=1}^{N} K'\left(\frac{x - x_i}{h}\right) x_i}{\sum_{i=1}^{N} K'\left(\frac{x - x_i}{h}\right)} \tag{39}$$

If rectangular Kernel function is used, (39) is reduced into(40).

$$x = \frac{\sum_{x_i \in L} x_i}{|L|} \quad , \quad K_r(x - x_i, h) = \begin{cases} 1, & \|x - x_i\|_2 \le h \\ 0, & \text{otherwise} \end{cases} \tag{40}$$

Where L : Set of all points for $K_r(x - x_i) = 1$;

$|L|$ **:** Cardinality of the set L

The initial points are required for Mean-Shift procedure. All hit locations in image coordinate are selected as initial points and they are updated until convergence. The convergence is defined as that changing in mean value between old mean and new mean is less than 20. All hit points with in convergence are merged and peak location is found. The distribution can be multimodal depending on number of targets and the result will be more than one peak location. If the merging is done in a single frame, then it is called as Intra-Frame Mean-Shift. To improve the detection, peak locations in individual frames are combined and consecutive frames are processed by Mean-Shift algorithm. This is called as Inter-Frame Mean-Shift and it reduces FA while

increasing detection performance. After finding local maxima in frame, mean shifted image pixel locations converted into local coordinate.

3.7.2 Weighted Mean Shift Algorithm

Each individual detector results hit locations and these hit locations are combined mean shift algorithm. 3.7.1 Mean shift algorithm is explained in detail. One more step to increase performance of data fusion is that we assigned to each detector a unique weight. Weights are calculated by CMA-ES algorithm and the aim of CMA-ES is to minimize Area above ROC (AAC) curve of detection algorithms. The minimum AAC gives the better performance while fusing data. Then, while mean shifting the data within the bandwidth, they are multiplicated with the corresponding weights then weighted data is used.

The weighted mean shift algorithm [15] is explained in equation (41).

$$\hat{f}(x) = \frac{1}{nh}\sum_{j=1}^{M}\sum_{i=1}^{N_j} K\left(\frac{x - x_{i,j}}{h}\right) w_j(x_{i,j}) \tag{41}$$

Where $w_j(x_{i,j})$ is the weight for point $x_{i,j}$, M is the number of different detection algorithm, N_j is the number of points corresponding to jth detection algorithm.

The gradient of above equation with respect to x is taken and equalized to zero, then updated version of x in equation (42).

$$x = \frac{\sum_{j=1}^{M}\sum_{i=1}^{N_j} K'\left(\frac{x - x_{i,j}}{h}\right) w_j(x_{i,j}) x_{i,j}}{\sum_{j=1}^{M}\sum_{i=1}^{N_j} K'\left(\frac{x - x_{i,j}}{h}\right) w_j(x_{i,j})} \tag{42}$$

If rectangular Kernel function is used, (42) is reduced into (43).

$$x = \frac{\sum_{x_{i,j}\in L} w_j(x_{i,j}) x_{i,j}}{\sum_{x_{i,j}\in L} w_j(x_{i,j})} \quad , \quad K(x - x_{i,j}, h) = \begin{cases} 1, & \left\| x - x_{i,j} \right\|_2 \le h \\ 0, & \text{otherwise} \end{cases} \tag{43}$$

Where K is the rectangular Kernel, h is the variance in window size. h will be used differently in detection algorithms.

3.8 Infrared Camera Registration

While system is moving on the road, Forward Looking IR camera records a scene in a multiple frames of video and the pose of scene is different at each time relatively to the camera. In other words, the position and orientation of object is changed from frame to frame in recorded video. Changing the size and shape of the object on video is a challenging; if the object is projected into world coordinates, then detection performance is improved. Additionally, the internal parameters and position of the camera should be known for calibration between image plane and world plane transition. Thus, IR camera registration is an important topic for precise detection and extracting world coordinates of landmines.

3.8.1 Perspective Projection Model

Pinhole camera is generally modelled as perspective projection. Three dimensional camera reference frame coordinates (X, Y, Z) is transformed into two dimensional image coordinates (x, y). 3D coordinate system has an origin at the center of projection and its Z axis is along the optical axis. The corresponding system is shown in Figure 23.

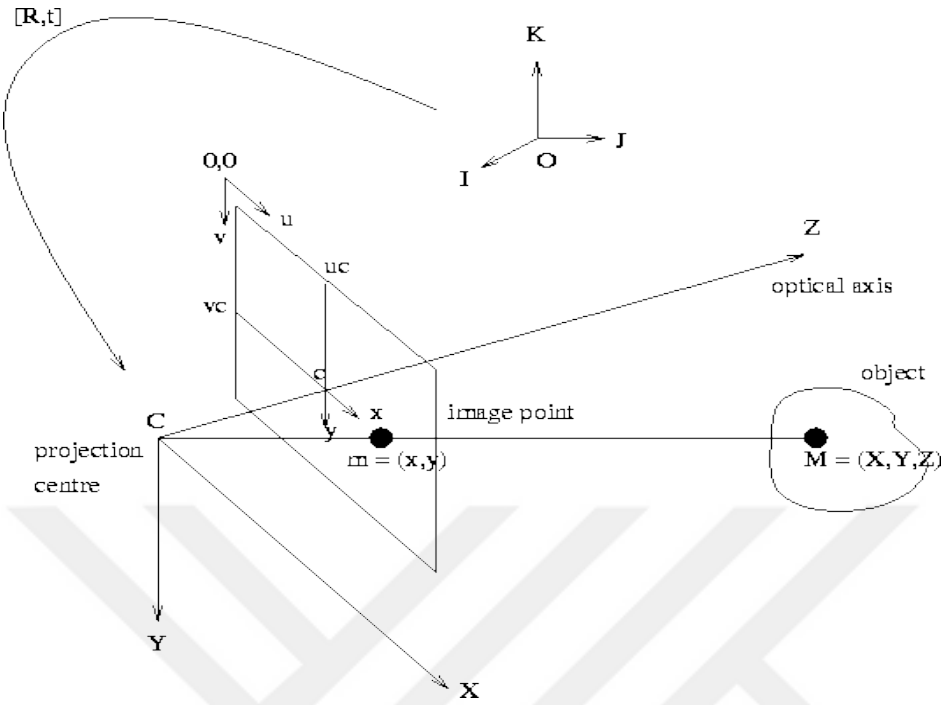

Figure 23 Perspective Projection Model

A point M on an object will be imaged at some point m=(x,y) in the image plane. These coordinates are the intersection of optical axis and image plane and whose x and y are parallel to the X and Y axes. The relationship between the two coordinate systems depends on 3x3 camera matrix which captures the intrinsic parameters of the camera. Firstly, relation depending on focal length of camera (f) is defined as in (44).

$$x = \frac{fX}{Z}, y = \frac{fY}{Z} \tag{44}$$

In homogeneous coordinates, this can be written as in matrix form equation (45).

$$\begin{bmatrix} x \\ y \\ 1 \end{bmatrix} = \begin{bmatrix} f & 0 & 0 & 0 \\ 0 & f & 0 & 0 \\ 0 & 0 & 1 & 0 \end{bmatrix} \begin{bmatrix} X \\ Y \\ Z \\ 1 \end{bmatrix} \tag{45}$$

The actual pixel coordinates (u, v) are defined with respect to an origin in the top left hand corner of the image plane, and (46) gives the relation.

$$u = u_c + \frac{x}{\text{pixel width}} \text{ and } v = v_c + \frac{y}{\text{pixel height}} \tag{46}$$

The resulting conversion from camera reference frame to image pixel coordinates is in (47).

$$Z_u = Z_{u_c} + \frac{Xf}{\text{pixel width}} \text{ and } Z_v = Z_{v_c} + \frac{Yf}{\text{pixel height}} \tag{47}$$

In homogeneous coordinates, the equation (47) is represented as in (48).

$$\begin{bmatrix} u \\ v \\ 1 \end{bmatrix} = \begin{bmatrix} \frac{f}{\text{pixel width}} & 0 & u_c & 0 \\ 0 & \frac{f}{\text{pixel height}} & v_c & 0 \\ 0 & 0 & 1 & 0 \end{bmatrix} \begin{bmatrix} X \\ Y \\ Z \\ 1 \end{bmatrix} \equiv \breve{\mathbf{u}} = \mathbf{P}.\breve{\mathbf{M}} \tag{48}$$

where $\breve{\mathbf{u}}$ represents the homogeneous vector of image pixel coordinates, $\mathbf{P}$ is the perspective projection matrix, and $\breve{\mathbf{M}}$ is the homogeneous vector of world coordinates.

There are five parameters such as which affect this equation and also known as intrinsic parameters of camera;

$$\alpha_u = \frac{f}{\text{pixel width}}, \qquad \alpha_v = \frac{f}{\text{pixel height}} \tag{49}$$

f : focal length

u_c : u pixel coordinate at the optical center

v_c : v pixel coordinate at the optical center

The resulting P matrix becomes as in(50);

$$\mathbf{P} = \begin{bmatrix} \alpha_u & 0 & u_c & 0 \\ 0 & \alpha_v & v_c & 0 \\ 0 & 0 & 1 & 0 \end{bmatrix} \tag{50}$$

3.8.2 World to Camera Reference Frame

To use described projection model, we must first transform world coordinates into the camera reference frame. We assume that we know 3D world coordinates from local coordinate references and transformation can be done with 3x3 rotation matrix **R** and 3x1 translation matrix **T**. In homogeneous form **K** matrix is represented in (51);

$$\mathbf{K} = \begin{bmatrix} \mathbf{R} & \mathbf{T} \\ 0_3^T & 1 \end{bmatrix} \tag{51}$$

Thus, multiplication (48) is converted into(52).

$$\breve{\mathbf{u}} = \mathbf{P.K.}\breve{\mathbf{M}} \tag{52}$$

Camera calibration matrix, **C**, equals to $\mathbf{C} = \mathbf{P}.\mathbf{K}$ and

$$\mathbf{C} = \mathbf{P.K} = \begin{bmatrix} \alpha_u & 0 & u_c & 0 \\ 0 & \alpha_v & v_c & 0 \\ 0 & 0 & 1 & 0 \end{bmatrix} \begin{bmatrix} \mathbf{r_1} & t_x \\ \mathbf{r_2} & t_y \\ \mathbf{r_3} & t_z \\ \mathbf{0} & 1 \end{bmatrix} = \begin{bmatrix} \alpha_u \mathbf{r_1} + u_c \mathbf{r_3} & \alpha_u t_x + u_c t_z \\ \alpha_v \mathbf{r_1} + u_v \mathbf{r_3} & \alpha_v t_x + v_c t_z \\ \mathbf{r_3} & t_z \end{bmatrix} \tag{53}$$

where the vectors

$$\mathbf{r_1} = \begin{bmatrix} r_{11} & r_{12} & r_{13} \end{bmatrix}, \mathbf{r_2} = \begin{bmatrix} r_{21} & r_{22} & r_{23} \end{bmatrix}, \mathbf{r_3} = \begin{bmatrix} r_{31} & r_{32} & r_{33} \end{bmatrix} \tag{54}$$

are the row vectors of the rotation matrix **R**, and translation matrix **T**

$$\mathbf{T} = \begin{bmatrix} t_x & t_y & t_z \end{bmatrix}' . \tag{55}$$

The matrix C, like the P, has rank three.

3.8.3 Solving for Calibration Matrix

Calibration is the process of the estimating the intrinsic and extrinsic parameters of the camera. It can be thought as a two stage process;

3.8.3.1 Estimating the Calibration Matrix C

$\breve{\mathbf{u}} = \mathbf{P.K.}\breve{\mathbf{M}}$ is converted into $\breve{\mathbf{u}} = \mathbf{C.}\breve{\mathbf{M}}$,

$$\begin{bmatrix} u \\ v \\ 1 \end{bmatrix} = \begin{bmatrix} c_{11} & c_{12} & c_{13} & c_{14} \\ c_{21} & c_{22} & c_{23} & c_{24} \\ c_{31} & c_{32} & c_{33} & c_{34} \end{bmatrix} \begin{bmatrix} X \\ Y \\ Z \\ 1 \end{bmatrix} = \begin{bmatrix} . & \mathbf{c}_1^T & . & . \\ . & \mathbf{c}_2^T & . & . \\ . & \mathbf{c}_3^T & . & . \end{bmatrix} \begin{bmatrix} X \\ Y \\ Z \\ 1 \end{bmatrix} \equiv \breve{\mathbf{u}} = \mathbf{C.}\breve{\mathbf{M}} \quad (56)$$

Conversion back from homogeneous coordinates results equation(57).

$$\mathbf{u} = \frac{\mathbf{c_1.M}}{\mathbf{c_3.M}} \text{ and } \mathbf{v} = \frac{\mathbf{c_2.M}}{\mathbf{c_3.M}} \quad (57)$$

Solving equation (56) for each point, i, results (58).

$$\begin{aligned} (\mathbf{c}_1 - u_i\mathbf{c}_3) \bullet \mathbf{M}_i &= 0 \\ (\mathbf{c}_1 - v_i\mathbf{c}_3) \bullet \mathbf{M}_i &= 0 \end{aligned} \quad (58)$$

If known and unknown parameters are combined in matrix form for n sample points, matrix form of multiplication is written as in (59).

$$\begin{bmatrix} \mathbf{M}_1^T & \mathbf{0}^T & -u_1\mathbf{M}_1^T \\ \mathbf{0}^T & \mathbf{M}_1^T & -v_1\mathbf{M}_1^T \\ \vdots & \vdots & \vdots \\ \mathbf{M}_n^T & \mathbf{0}^T & -u_n\mathbf{M}_n^T \\ \mathbf{0}^T & \mathbf{M}_n^T & -v_n\mathbf{M}_n^T \end{bmatrix} \begin{bmatrix} \mathbf{c}_1 \\ \mathbf{c}_2 \\ \mathbf{c}_3 \end{bmatrix} = \begin{bmatrix} 0 \\ 0 \\ \vdots \\ 0 \\ 0 \end{bmatrix} \equiv \mathbf{A.x = 0} \quad (59)$$

All elements of (59) are shown in equation (60).

$$\begin{bmatrix} M_{1x} & M_{1y} & M_{1z} & 1 & 0 & 0 & 0 & 0 & -u_1M_{1x} & -u_1M_{1y} & -u_1M_{1z} & -u_1 \\ 0 & 0 & 0 & 0 & M_{1x} & M_{1y} & M_{1z} & 1 & -v_1M_{1x} & -v_1M_{1y} & -v_1M_{1z} & -v_1 \\ \vdots & \vdots & \vdots & \vdots & \vdots & \vdots & \vdots & \vdots & \vdots & \vdots & \vdots & \vdots \\ M_{nx} & M_{ny} & M_{nz} & 1 & 0 & 0 & 0 & 0 & -u_nM_{nx} & -u_nM_{ny} & -u_nM_{nz} & -u_n \\ 0 & 0 & 0 & 0 & M_{nx} & M_{ny} & M_{nz} & 1 & -v_nM_{nx} & -v_nM_{ny} & -v_nM_{nz} & -v_n \end{bmatrix} \begin{bmatrix} c_{11} \\ c_{12} \\ c_{13} \\ c_{14} \\ c_{21} \\ c_{22} \\ c_{23} \\ c_{24} \\ c_{31} \\ c_{32} \\ c_{33} \\ c_{34} \end{bmatrix} = \begin{bmatrix} 0 \\ 0 \\ \vdots \\ 0 \\ 0 \end{bmatrix} \quad (60)$$

To solve (60), we should find minimum eigenvector corresponding to minimum eigenvalue of **A** matrix or Single Value Decomposition (SVD) can be used to solve homogeneous mxn linear system. A is and mxn matrix where rows m are greater than the columns n. Then, $\mathbf{A=USV^T}$ such that;

U is a column orthogonal matrix of size mxn.

S is a diagonal matrix with positive or zero elements of size nxn.

V is an orthogonal matrix of size nxn.

Let **S**=diag{σ1, σ2,…, σn} where σ1≥ σ2≥…≥ σn≥0 then σ1, σ2,…, σn are called singular values of **A**. These singular values are not same as the eigenvalues. For a matrix **A**, matrix $\mathbf{A^HA}$ is normal with non-negative eigenvalues where singular values of **A** are square root of the eigenvalues of $\mathbf{A^HA}$. The last column of **V** gives the **c** column vector where the size of this column vector equals to 12x1. Calibration matrix **C** is the 3x4 form of 12x1 column vector.

3.8.3.2 Estimating the Intrinsic and Extrinsic Parameters

A general 3x4 projective matrix has eleven degrees of freedom: it has 12 entries, but an arbitrary scale factor is involved, so one of the entries can be set to 1 without loss of generality. **C** matrix can be written as in (61);

$$\mathbf{C} = \begin{bmatrix} \mathbf{q}_1^T & q_{14} \\ \mathbf{q}_2^T & q_{24} \\ \mathbf{q}_3^T & q_{34} \end{bmatrix}, \tag{61}$$

C matrix includes four sets of intrinsic and extrinsic parameters if and only if the following two conditions are satisfied:

- $\|q_3\| = 1$
- $(\mathbf{q_1} \times \mathbf{q_3}) \bullet (\mathbf{q_2} \times \mathbf{q_3}) = 0$, $\times$: means cross product, $\bullet$: means dot product

The proof of these conditions is explained as;

If **C** is in the form of equation (59), then $\mathbf{q_3} = \mathbf{r_3}$ and since $\mathbf{r_3}$ is a row of rotation matrix, its norm is 1. Additionally, (62) is the proof of equality of zero.

$$\begin{aligned} (\mathbf{q_1} \times \mathbf{q_3}) \bullet (\mathbf{q_2} \times \mathbf{q_3}) &= ((\alpha_u \mathbf{r_1} + u_c \mathbf{r_3}) \times \mathbf{r_3}) \bullet ((\alpha_v \mathbf{r_2} + v_c \mathbf{r_3}) \times \mathbf{r_3}) \\ &= (\alpha_u \mathbf{r_1} \times \mathbf{r_3}) \bullet (\alpha_v \mathbf{r_2} \times \mathbf{r_3}) = 0 \end{aligned} \tag{62}$$

The calibration matrix is the equality of (53) and (61) as in (63);

$$\mathbf{C} = \begin{bmatrix} \alpha_u \mathbf{r_1} + u_c \mathbf{r_3} & \alpha_u t_x + u_c t_z \\ \alpha_v \mathbf{r_1} + u_v \mathbf{r_3} & \alpha_v t_x + v_c t_z \\ \mathbf{r_3} & t_z \end{bmatrix} = \begin{bmatrix} \mathbf{q}_1^T & q_{14} \\ \mathbf{q}_2^T & q_{24} \\ \mathbf{q}_3^T & q_{34} \end{bmatrix} \tag{63}$$

The results are shown (64),(65),(66),(67) and (68).

$$t_z = q_{34} \quad \text{and} \quad \mathbf{r_3} = \mathbf{q_3^T} \tag{64}$$

Taking the inner product of $\mathbf{q_3}$ with $\mathbf{q_1}$ and $\mathbf{q_2}$ yields u_c and v_c :

$$u_c = \mathbf{q_1^T} \bullet \mathbf{q_3} \quad \text{and} \quad v_c = \mathbf{q_2^T} \bullet \mathbf{q_3} \tag{65}$$

Computing the squared magnitudes of $\mathbf{q_1}$ and $\mathbf{q_2}$ yields:

$$\alpha_u = \sqrt{\mathbf{q_1^T q_1} - u_c} \quad \text{and} \quad \alpha_v = \sqrt{\mathbf{q_2^T q_2} - v_c} \tag{66}$$

Rotation matrix parameters are found as;

$$\mathbf{r}_1 = \frac{\mathbf{q}_1^T - u_c \mathbf{q}_3^T}{\alpha_u} \qquad \text{and} \qquad \mathbf{r}_2 = \frac{\mathbf{q}_2^T - u_c \mathbf{q}_3^T}{\alpha_v} \tag{67}$$

Translation matrix parameters are found as;

$$t_x = \frac{q_{14} - u_c t_z}{\alpha_u} \qquad \text{and} \qquad t_y = \frac{q_{24} - v_c t_z}{\alpha_v} \tag{68}$$

3.8.4 Solving for Calibration Matrix under Flat Earth Assumption

In our particular case, we could not get information about the height of the vehicle and target in landmine detection system. Flat earth assumption is done in this situation. Z is selected as '0' that means, everything is assumed to lie in Z=0 plane. The corresponding figure is shown in Figure 24.

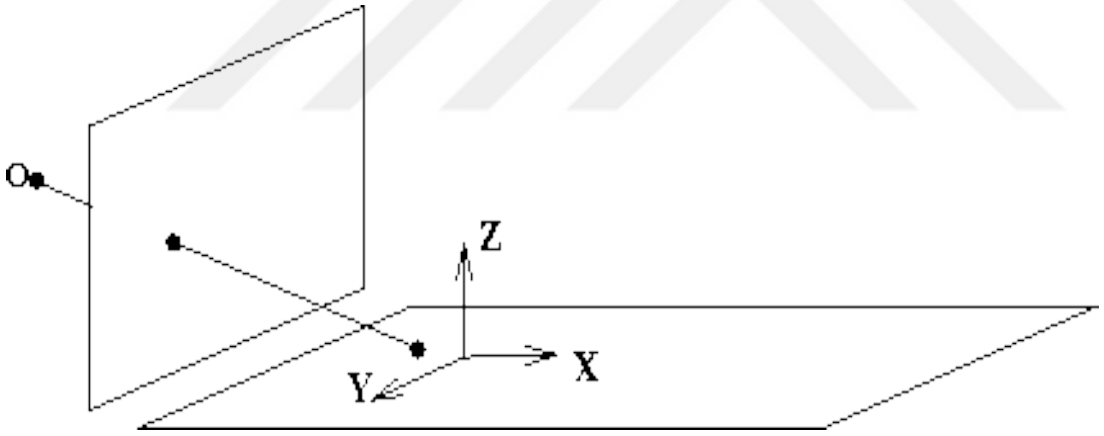

Figure 24 Plane Projective Model

The plane projection matrix at Z=0, (53) is reduced to (69).

$$\begin{bmatrix} x \\ y \\ 1 \end{bmatrix} = \begin{bmatrix} p_{11} & p_{12} & p_{13} & p_{14} \\ p_{21} & p_{22} & p_{23} & p_{24} \\ p_{31} & p_{32} & p_{33} & p_{34} \end{bmatrix} \begin{bmatrix} X \\ Y \\ 0 \\ 1 \end{bmatrix} = \begin{bmatrix} \alpha_u & 0 & u_x \\ 0 & \alpha_v & u_y \\ 0 & 0 & 1 \end{bmatrix} \begin{bmatrix} X \\ Y \\ 1 \end{bmatrix} \tag{69}$$

The calibration matrix becomes into (70).

$$\mathbf{C} = \begin{bmatrix} \alpha_u \mathbf{r}_1 & \alpha_u t_x + u_c \\ \alpha_v \mathbf{r}_2 & \alpha_v t_y + v_c \\ 0 & 1 \end{bmatrix} = \begin{bmatrix} q_1^T & q_{13} \\ q_2^T & q_{23} \\ q_3^T & q_{33} \end{bmatrix} \tag{70}$$

3.8.5 CMA-ES Optimization Algorithm

To minimize 3x3 plane projective matrix, SVD method also can be used. These projection functions may include properties such that SVD or other gradient descent algorithms suffer from. These properties are:

- Non-linear, non-quadratic, non-convex
- Ruggedness
    - Non-smooth, discontinuous, multimodal and/or noisy function
- Non-separable
    - Dependencies between the objective variables
- Ill-conditioning

The optimization process Covariance Matrix Adaptation Evolution Strategy (CMA-ES) is designed for non-linear functions. Numerical optimization of non-linear or non-convex continuous optimization problems is solved by Evolution strategies (ES), which is stochastic, derivative-free method. An evolutionary algorithm is based on the principle of biological evolution: variation and selection. Variation occurs due to recombination and mutation. In each generation (iteration) new individuals (candidate solutions, denoted as x) are generated by variation. Then, some individuals are selected to become the parents in the next generation based on their fitness or objective function value f(x). In an evolution strategy, new candidate solutions are sampled according to a multivariate normal distribution in the R^n. Recombination amounts to selecting a new mean value for the distribution. Mutation amounts to adding a random vector, a perturbation with zero mean. Pairwise dependencies between the variables in the distribution are represented by a covariance matrix. The covariance matrix adaptation (CMA) is a method to update

the covariance matrix of this distribution. This is particularly useful, if the function f is ill-conditioned. The generation process is basically shown in Figure 25.

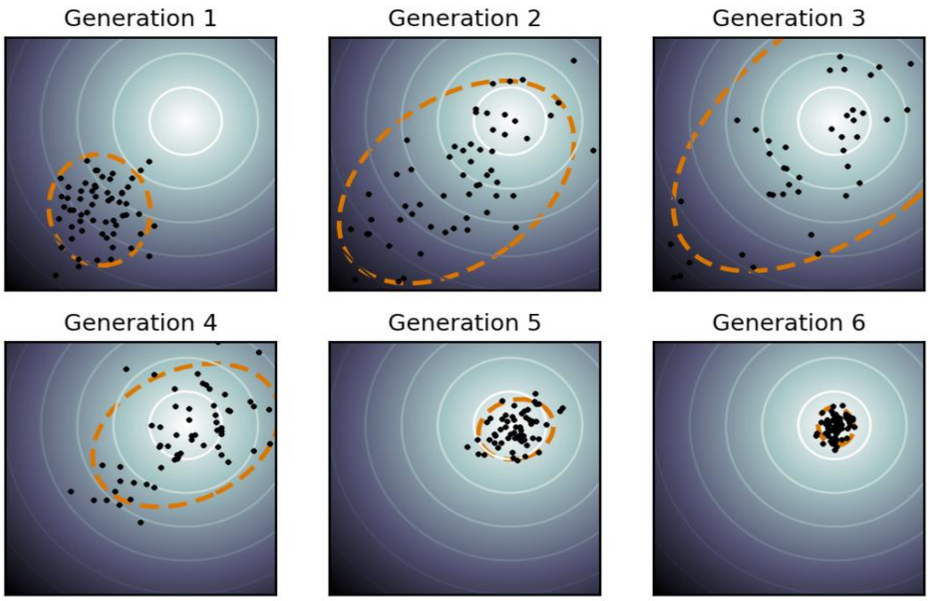

Figure 25 Generation Steps for CMA-ES Algorithm

3.8.5.1 Sampling

In the CMA Evolution Strategy, a population of new search points (individuals, offspring) is generated by sampling a multivariate normal distribution. The basic equation for sampling the search points, for generation number g = 0,1,2,…

$$x_k^{(g+1)} \sim m^{(g)} + \sigma^{(g)} N(0, C^{(g)}) \quad \text{for } k=1,...,\lambda \tag{71}$$

where $\sim$: denotes the same distribution on the left and right hand side

$N(0,C^{(g)})$: multivariate distribution with zero mean and covariance matrix $C^{(g)}$

$x_k^{(g+1)} \in R^n$,:k-th offspring form generation g+1

$m^{(g)} \in R^n$: mean value of the search distribution at the generation g

$\sigma^{(g)} \in R_+$:"overall" standard deviation, step size, at generation g

$C^{(g)} \in R^{nxn}$: covariance matrix at generation g

$\lambda \geq 2$: population size, sample size, number of offspring

3.8.5.2 Selection and Recombination: Moving the Mean

The new mean $m^{(g+1)}$of the search distribution is a weighted average of μ selected points from the sample $x_1^{(g+1)}, \ldots, x_\lambda^{(g+1)}$ and it is written as (72).

$$m^{(g+1)} = \sum_{i=1}^{\mu} w_i x_{i:\lambda}^{(g+1)} \tag{72}$$

$$\sum_{i=1}^{\mu} w_i = 1, \; w_1 \geq w_2 \geq \cdots \geq w_\mu \geq 0 \tag{73}$$

$\mu \leq \lambda$: the parent population size, i.e. the number of selected points

$w_{i=1\ldots\mu} \in R_+$: positive weight coefficients for recombination

$x_{i:\lambda}^{(g+1)}$: i-th best individual out of $x_1^{(g+1)}, \ldots, x_\lambda^{(g+1)}$ and

$$f(x_{i:\lambda}^{(g+1)}) \leq f(x_{2:\lambda}^{(g+1)}) \leq \cdots \leq f(x_{\lambda:\lambda}^{(g+1)})$$

3.8.5.3 Adapting Covariance Matrix

$$p_c^{(g+1)} = (1-c_c)p_c^{(g)} + \sqrt{c_c(2-c_c)\mu_{eff}}\,\frac{m^{(g+1)} - m^{(g)}}{\sigma^{(g)}} \quad \text{where} \tag{74}$$

$p_c^{(g)} \in R^n$: evolution path at generation g.

$c_c \leq 1, 1/c_c$: the backward time horizon of the evolution path p_c

$\mu_{eff} \leq 1 + \ln n$

Resulting covariance matrix adaptation is obtained (75).

$$C^{(g+1)} = (1 - c_1 - c_\mu)C^{(g)} + c_1 \underbrace{p_c^{(g+1)} p_c^{(g+1)^T}}_{\text{Rank-one update}} + c_\mu \underbrace{\sum_{i=1}^{\mu} w_i y_{i:\lambda}^{(g+1)} y_{i:\lambda}^{(g+1)^T}}_{\text{Rank-}\mu\text{ update}} \tag{75}$$

- **Rank-one update:** The complete covariance matrix is calculated by using selected steps from single generation.
- **Rank-μ update:** The complete covariance matrix is calculated by using previous generations' information

The corresponding figure for covariance adaptation for one generation is shown in Figure 26.

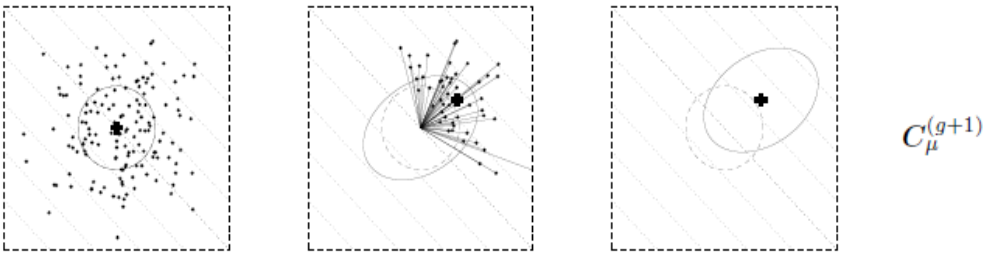

Figure 26 Covariance Matrix Adaptation

3.8.5.4 Step Size Control

Two specific reasons to introduce a step-size control in addition to adaptation rule;

- The optimal overall step length cannot be well approximated, in particular if μ_{eff} is chosen larger than one.
- The largest reliable learning rate for the covariance matrix update is too slow to achieve competitive change rates for overall step length.

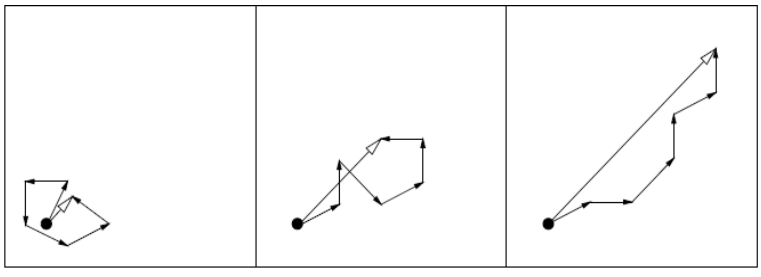

Figure 27 Step Size Control

Default strategy parameters are defined in (76),(77) and (78).

- Selection and Recombination

$$\lambda = 4 + \lfloor 3\ln n \rfloor, \quad \mu = \lfloor \mu' \rfloor, \quad \mu' = \frac{\lambda}{2}$$
$$w_i = \frac{w_i'}{\sum_{j=1}^{\mu} w_j}, \qquad w_i' = \ln(\mu' + 0.50) - \ln i \quad \text{for } i=1,\ldots,\mu \tag{76}$$

- Step-size control

$$c_\sigma = \frac{\mu_{eff} + 2}{n + \mu_{eff} + 5}, \qquad d_\sigma = 1 + 2\max\left(0, \sqrt{\frac{\mu_{eff} - 1}{n+1}}\right) + c_\sigma \tag{77}$$

- Covariance matrix adaptation

$$c_c = \frac{4 + \frac{\mu_{eff}}{n}}{n + 4 + \frac{2\mu_{eff}}{n}}, \qquad c_1 = \frac{2}{(n+1.3)^2 + \mu_{eff}},$$
$$c_\mu = \min\left(1 - c_1, \alpha_\mu \frac{\mu_{eff} - 2 + \frac{1}{\mu_{eff}}}{(n+2)^2 + \frac{\alpha_\mu \mu_{eff}}{2}}\right) \tag{78}$$
$$\text{with } \alpha_\mu = 2 \text{ where } \mu_{eff} = \frac{1}{\sum_{i=1}^{\mu} w_i^2} \geq 1 \text{ and } \sum_{i=1}^{\mu} w_i = 1$$

3.9 Post-Processing of IR Imagery

After converting the image coordinates into world coordinates, there occurs some anomaly at boundary. The boundary is known in environment such as road width, so we could eliminate the false alarms caused by boundary. The anomaly locations out of the boundary are taken out at this step.

CHAPTER 4

FLIR BASED LANDMINE DETECTION ALGORITHMS AND SENSITIVITY ANALYSIS BASED ON EXPERIMENTAL TEST SETUP FRAME SET

4.1 FLIR Based Algorithm Results Based on FLIR Train and Test Sets

This section of thesis, we take train set and test sets from FLIR sample videos and run all detection algorithms with these sets. Both train and test sets are formed by 10 frames in sample videos at 16:53, 10:30 and 18:00, respectively. Figure 28 is example frame which is the 700th frame from train set. This frame is recorded at 16:53, 23 August 2016. The weather temperature is like in Figure 16 during the day. There is as awning at the right hand side of test setup, that so, after midday, the shadow effects on imagery could be seen. The awning partially prevents the sun light to reach top-right corner of sandbox and this area is shown cooler than expected.

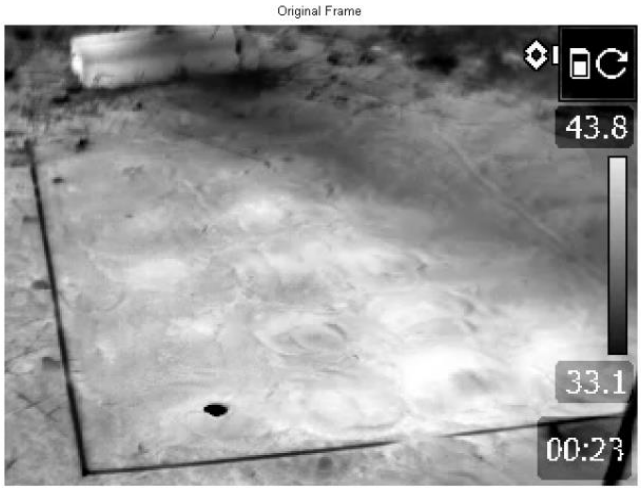

Figure 28 Example Frame from Train Set taken by FLIR T440 at 16:53

We also label the ground truth of train frames to calculate performance metrics of detection algorithms. Figure 29 shows that there are green windows which indicate landmine locations inside them. If the pixel locations are inside the border of green windows, then they are labelled as possible landmine. We bury 12 different landmines and 4 different clutters in our setup, so we do not label the clutter location as ‘1’. Because, the clutters cause false alarms and they affect the performance of detectors. Additionally, there is an empty column at the right hand side of frame. We do not label empty column as ‘1’, either.

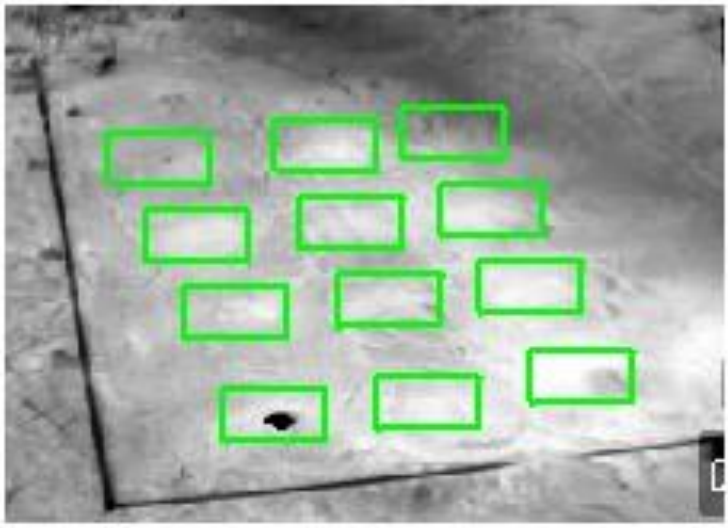

Figure 29 Ground Truth of Example Train Frame used in Performance Metrics

After defining the pixel locations of possible landmines, we label as ‘1’ for possible landmine locations and otherwise, we label as ‘0’. The corresponding binary labelling is shown in Figure 30.

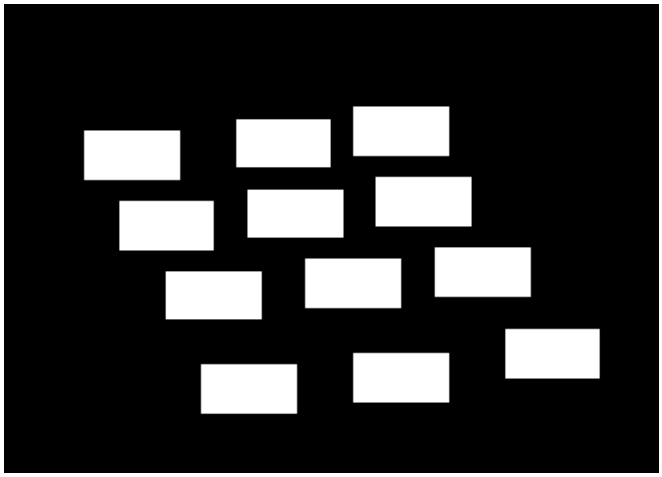

Figure 30 Binary Labelling of Example Train Frame used in Performance Metrics

After train set process, we also define test sets to understand that the performance improvement is valid different frames under different conditions. Our test sets are chosen from video samples taken at 10:30 and 18:00. We select morning and evening hours to compare train frames IR signatures taken at 16:53. Figure 31 indicates an example test frame, which is the 700^{th} frame from test set, taken at 10:30. The IR signature is also related with material of landmine. The right-bottom located landmine has full aluminium type of material so it is colder compared to other landmine types at 10:30 hour.

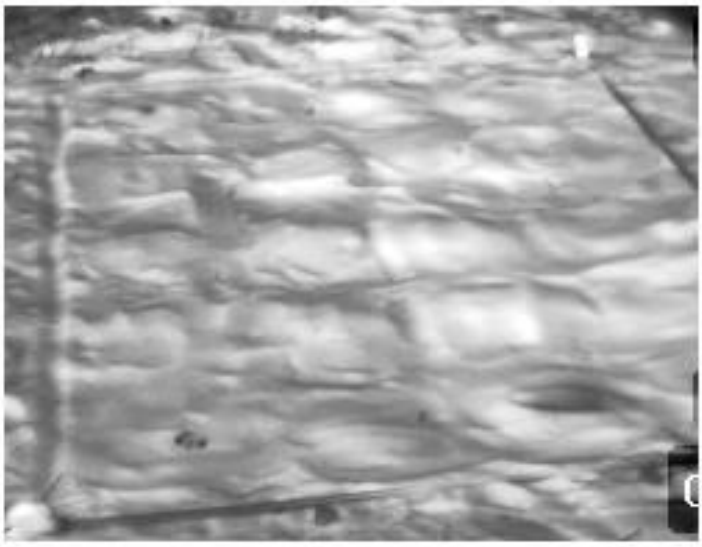

Figure 31 Example Frame from Test Set taken at 10:30

We also extract the ground truth locations for the first test frames. The inside of the green windows point landmine locations as shown in Figure 32.

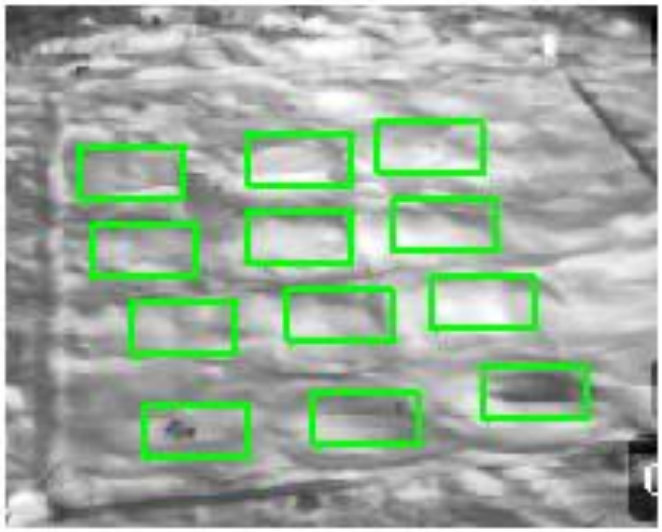

Figure 32 Ground Truth of Example Test Frame at 10:30 used in Performance Metrics

The other test set is run with detection algorithms to compare performances. This test frames are recorded at 18:00. Figure 33 indicates the example test frame, which is the 700th frame from test set, recorded at 18:00.

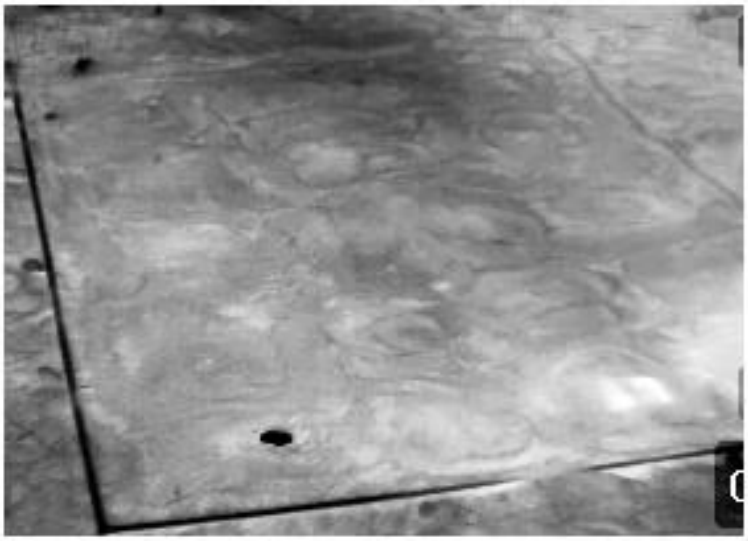

Figure 33 Example Test Frame from Test Set taken at 18:00

We also extract the ground truth locations for the second test frames. The inside of the green windows point landmine locations as shown in Figure 32

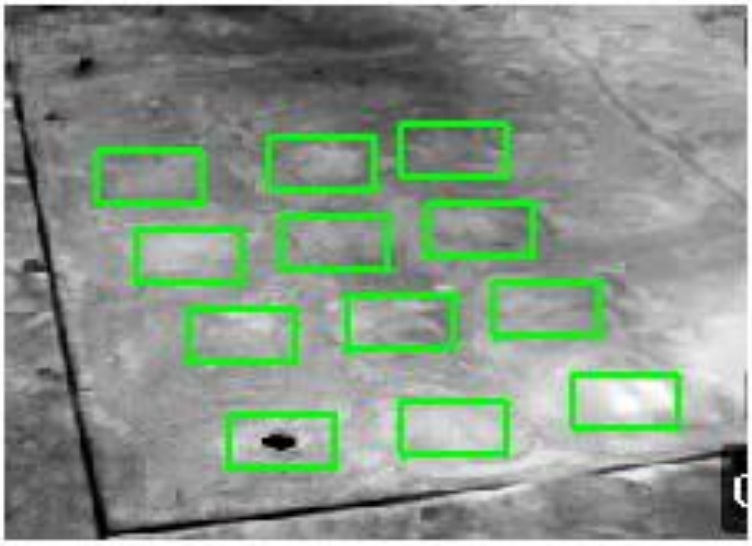

Figure 34 Ground Truth of Example Test Frame at 18:00 used in Performance Metrics

After selecting train set and test sets and defining ground truth locations for each set, we process all detection algorithms on train and test frames.

4.1.1 Pre-Processing of IR Imagery

4.1.1.1 Adaptive Histogram Equalization Algorithm

The parameters for Adaptive Histogram Equalization Algorithm are clipping limit, number of bins, alpha and distribution. The used parameters for simulations are stated in **Error! Reference source not found.** as referenced in [51].

Table 9 Contrast Limited Adaptive Histogram Equalization Algorithm Parameters

Contrast Limited Adaptive Histogram Equalization Paramaters	
Parameter	**Initial Value**
Clip Limit	0,01
Number of bins	256
Alpha	0,04
Distribution	Rayleigh

Increasing the clipping limit enhances the contrast of image. In these simulations, we extract how the clipping limit affects the detection algorithm performances.

The indicators of the right side of frames are removed and histogram equalization method is applied to clipped train frames. Figure 35 indicates the result of example train frame after processing of histogram equalization.

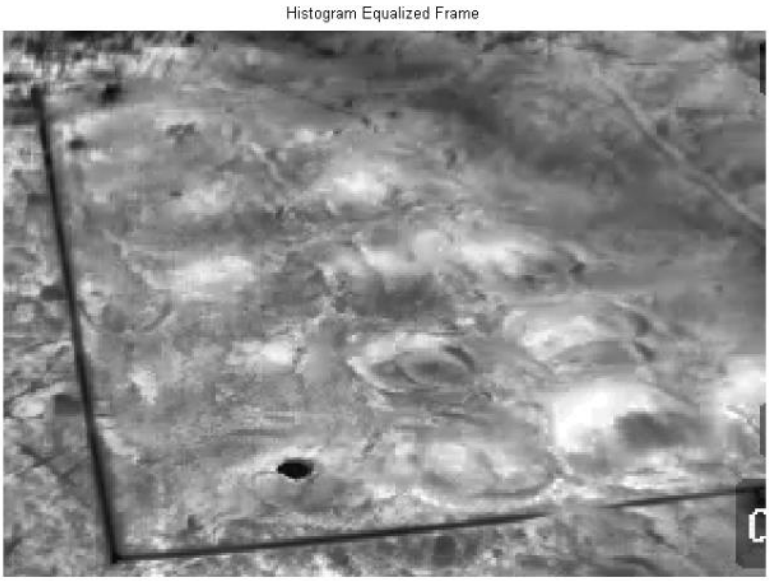

Figure 35 Histogram Equalized Example Train Frame

After these pre-processing steps, train set is run at Trainable Size Contrast Filters, Corner Detection, Gaussian Model Detection and Maximally Stable Extremal Region Detection algorithms. Optimum performances are observed at clipping limit 0.01. So that, we process all detection algorithms in this section with clipping limit 0.01.

4.1.2 Landmine Detection Algorithms Results on Train Sets

In this thesis, we have implemented four detection algorithms such as Trainable Size Contrast Filters based detection, Corner based detection, Gaussian Model based detection and Maximally Stable Extremal Region based detection. The block diagram of algorithms is shown in Figure 7. In this section of thesis, we analyse the performances of algorithms based on different values which affect the algorithms. Iteratively, we change the parameters value and observe the performance at each

step. We also analyse Receiver Operating Characteristic (ROC) curve while changing the parameters. All simulations are run at MATLAB 2014a. After using parameter values as assigned initially, we examine the sensitivity analysis for landmine detection algorithms to explain the effects of metrics on performance based on both FAR and process time. Area under ROC (AROC), True Positive Rate (TPR) and False Positive Rate (FPR) metrics are calculated. In section 4.1, we have mentioned that the train and test sets with ground truth. Ground truth of frames are used in TPR and FPR calculation. After labelling the ground truth, possible landmine pixel locations are calculated by detection algorithms and compared to ground truth locations to find True Positives and False Positive. We do this analysis for both optimum threshold and fixed FPR at 0.25. Our aim is to find optimum parameters for each detection algorithms which provides maximum AROC and TPR besides min FAR and fixed FAR. We use optimum threshold for first analysis. We calculate the distance 1-TPR and FPR and the ratio corresponding minimum distance gives the optimum threshold location. The equation gives the calculation about finding optimum threshold value for ROC.

$$\min(\text{distance}(i)) = \min(\sqrt{(1-\text{TPR}(i))^2 + (\text{FPR}(i))^2}) \qquad (79)$$

Where i is the number of ratios.

The second analysis for AROC, TPR and FPR is processed at fixed false positive rate. Our aim is to find AROC and TPR values at fixed FPR=0.25. Then, we compare the results of train set and the analysis is explained in 4.1.2.6. Additionally, other performance metrics such as sensitivity, specificity are calculated as explained in section 3.6. Furthermore, we try to both find optimum parameters and understand that the optimum parameters are usable for all sample videos which are recorded by our test setup environment.

4.1.2.1 Trainable Size Contrast Filters Based Landmine Detection Algorithm and Results

The first implemented algorithm for Landmine Detection is Trainable Size Contrast Filters based landmine detection. The block diagram for algorithm is indicated in Figure 36.

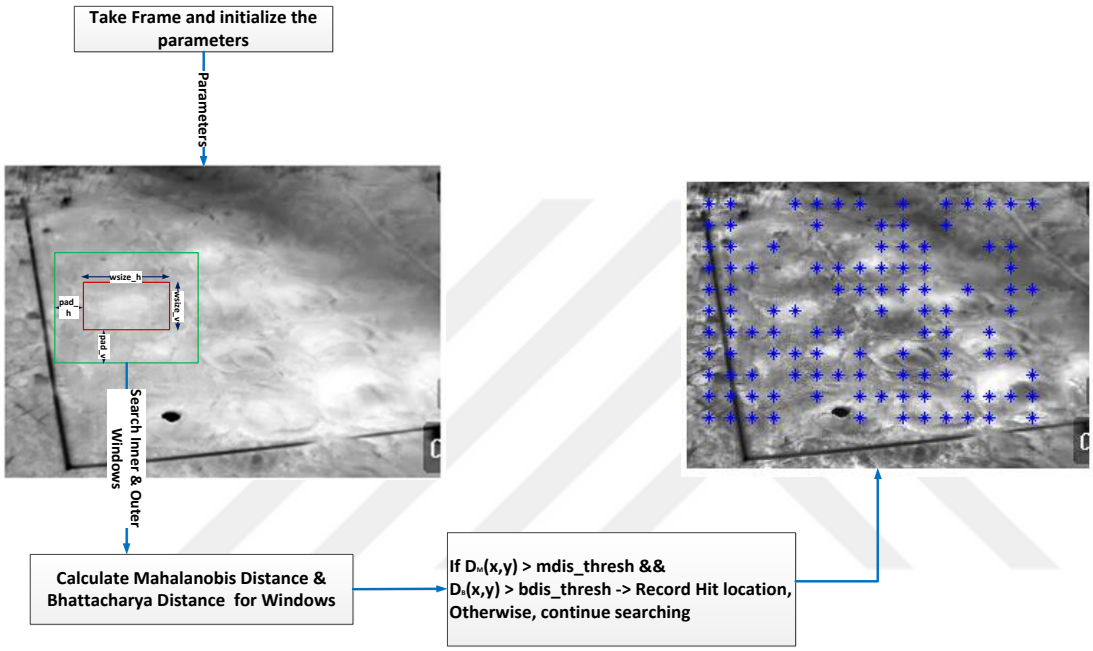

Figure 36 Trainable Size Contrast Filters Detection Algorithm Block Diagram

According to [16], Trainable Size Contrast Filters Detection algorithm is implemented 8 different algorithm parameters with 14 iterations. The initial and optimum parameters are seen in Table 10.

Table 10 Trainable Size Contrast Filter Based Landmine Detection Algorithm Parameters

Trainable Size Contrast Filter Based Landmine Detection Algorithm Parameters		
Parameter	**Initial Value**	**Optimum Value**
Clip Limit	0,01	0,01
Width	14	20
Height	1	20
Pad_width	17	20
Pad_height	38	20
Bhattacharya Distance	0,9365	200
Mahalanobis Distance	397,7208	500
Variance in Window Size	40	40

The detector parameters are Bhattacharya distance, Mahalanobis distance and window sizes at horizontal and vertical directions.

The detected landmines for initial values are shown in Figure 37. This algorithm with initial values detects nearly 4 landmine locations within 12 landmines. The boundary of sandbox affects the detection, because, the decision is made according to variation and mean value of surrounding of center area. The boundary has dramatic changes; however, these false landmines will be removed in post-processing.

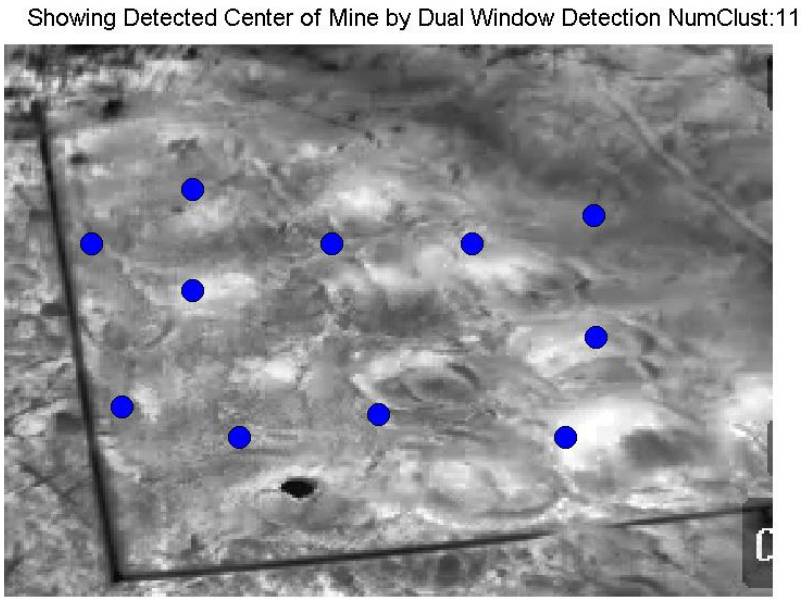

Figure 37 Trainable Size Contrast Filter Based Landmine Detections with Initial Values for Train Set

The corresponding ROC curve and threshold values for ROC are given in Figure 38.

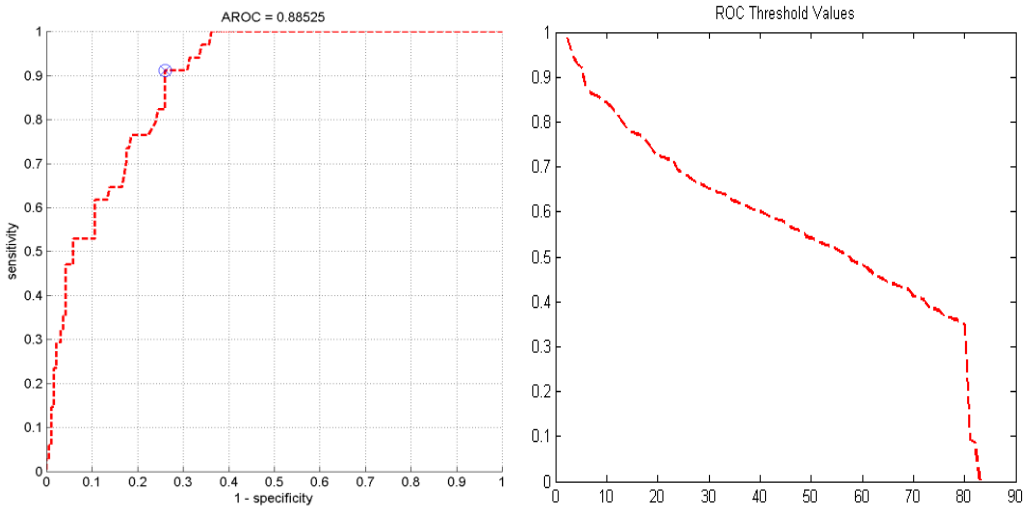

Figure 38 ROC and Threshold of Trainable Size Contrast Filter Based Landmine Detection with Initial Values for Train Set at Optimum Threshold

The detected landmines for optimum values are shown in Figure 39. This algorithm detects nearly 8 landmine locations within 12 landmines.

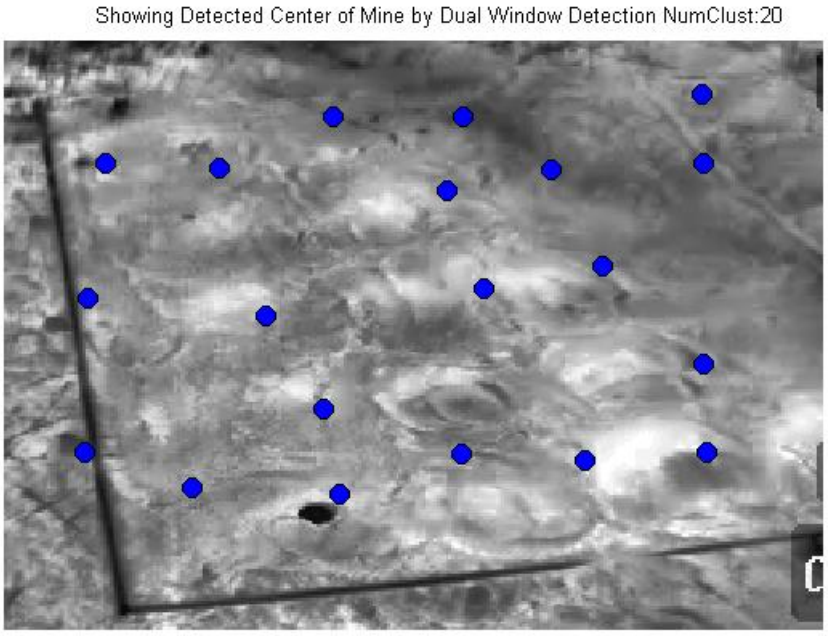

Figure 39 Trainable Size Contrast Filter Based Landmine Detections with Optimum Values for Train Set

The corresponding ROC curve and threshold values for ROC are given in Figure 40.

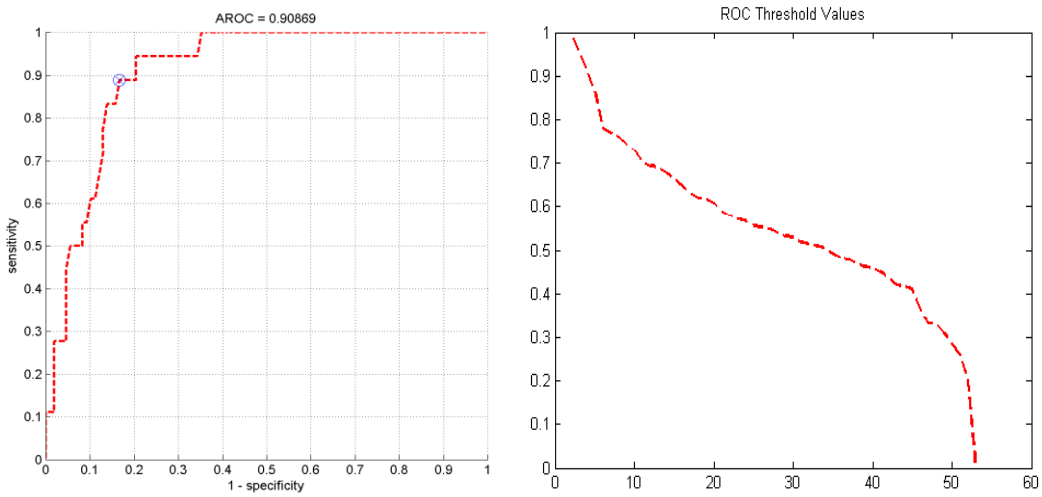

Figure 40 ROC and Threshold of Trainable Size Contrast Filter Based Landmine Detection with Optimum Values for Train Set at Optimum Threshold

The performance of algorithm is enough; however, FLIR image are sensitive to window size. In sensitivity analysis, we will compare the results with different window sizes.

4.1.2.2 Corner Based Landmine Detection Algorithm and Results

Block diagram for corner based anomaly detection is shown in Figure 41. While implementing Corner based detection algorithm, the variables are defined for extracting the curvature. Table 11 shows the variables for Corner detection based algorithm.

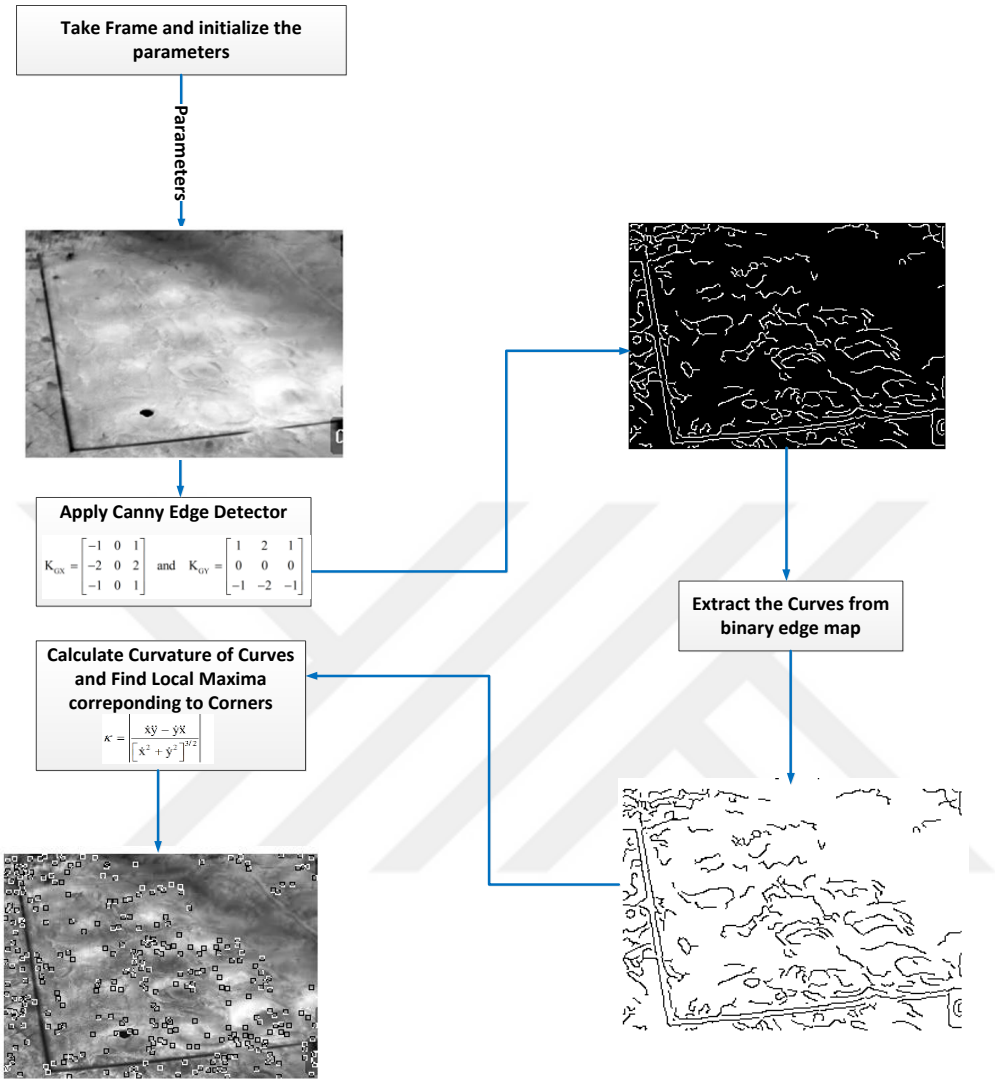

Figure 41 Corner Detection Based Landmine Detection Algorithm Block Diagram

According to [59] and [62], Corner Detection algorithm is implemented with variables defined in Table 11. C defines the axes ratio of corner inscribed ellipse, L and H are the thresholds for edges, T is the maximum angle of corner and gap size is the gap between start and end point.

Table 11 Corner Based Landmine Detection Algorithm Parameters

Corner Based Landmine Detection Algorithm Parameters		
Parameter	**Initial Value**	**Optimum Value**
Clip Limit	0,01	0,01
C	1,5	1,5
L	0,15	0,15
H	0,35	0,35
T	160	160
Sigma	3	2,5
End Point	1	1
Gap Size	20	20
Variance in Window Size	45	45

The algorithm result based on initial and optimum values is shown in Figure 42 and Figure 44, respectively. The algorithm detects nearly 5 landmines within 12 landmines. The problem is that the test setup has gap 40 cm between landmines; so corners of landmines are so close to separate them from each other. When we fuse the corners, we find the locations between the mines. If the mine gap in test area is higher, then this algorithm will have better performance.

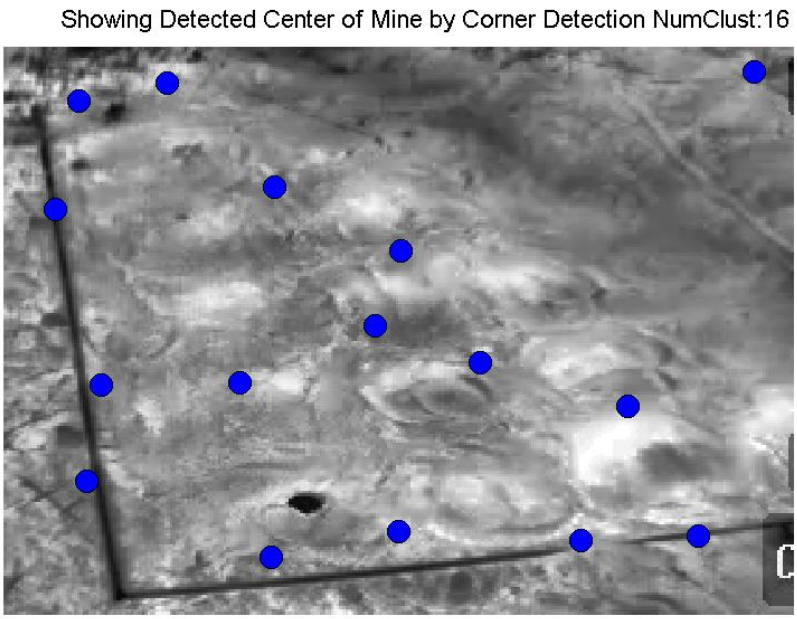

Figure 42 Corner Based Landmine Detections with Initial Values for Train Set

The corresponding ROC curve and threshold values are shown in Figure 43.

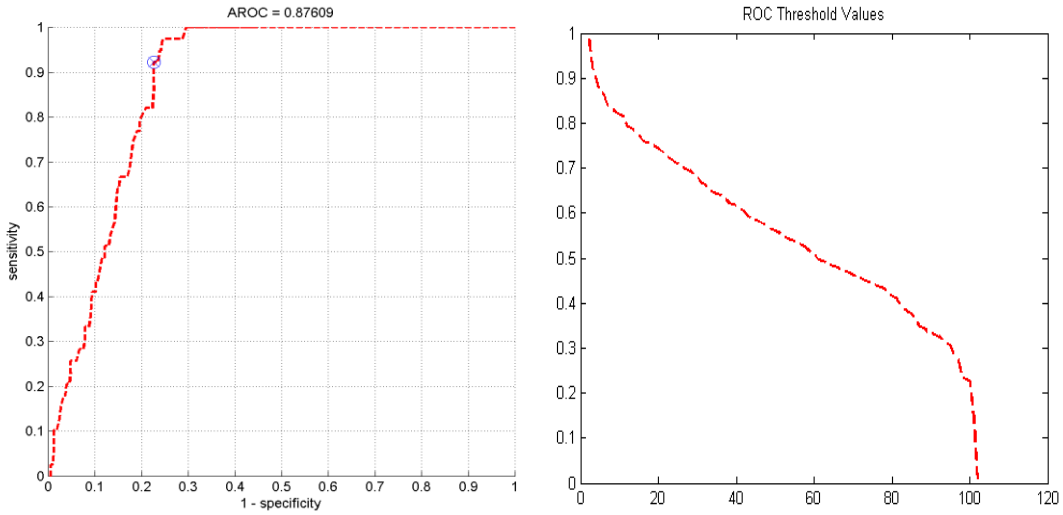

Figure 43 ROC and Threshold of Corner Based Landmine Detection with Initial Value for Train Set at Optimum Threshold

The algorithm result for optimum value is shown in Figure 44.

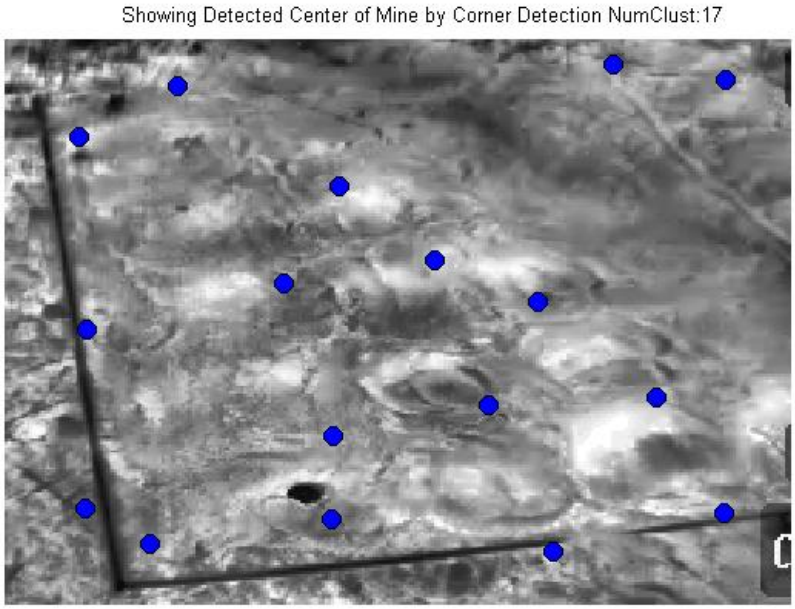

Figure 44 Corner Based Landmine Detections with Optimum Values for Train Set

The ROC curve for Figure 44 is given in Figure 45.

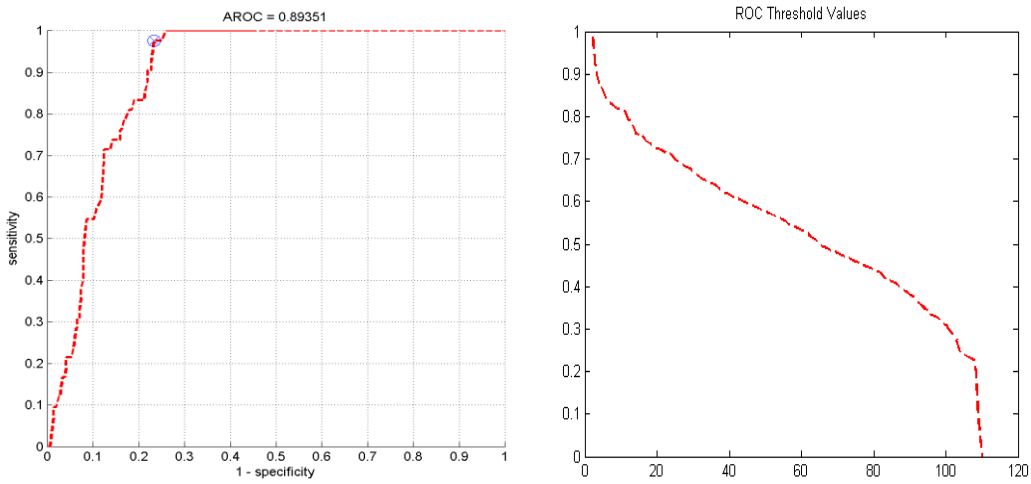

Figure 45 ROC and Threshold of Corner Based Landmine Detection with Optimum Values for Train Set at Optimum Threshold

The performance of Corner based detection is very sensitive to high and low threshold value that we use while extracting the edges. These thresholds also depend on the FLIR image. According to our test image, we optimize the values as shown in Table 11. The effects of parameters are analyzed in sensitivity section.

4.1.2.3 Gaussian Model Based Landmine Detection Algorithm and Results

Block diagram for Gaussian Model based anomaly detection is shown in Figure 46. While implementing for Gaussian Model based detection algorithm, there are 2 variables which are alpha which effects the Gaussian curve and constant which effects the background and foreground intensity discrimination.

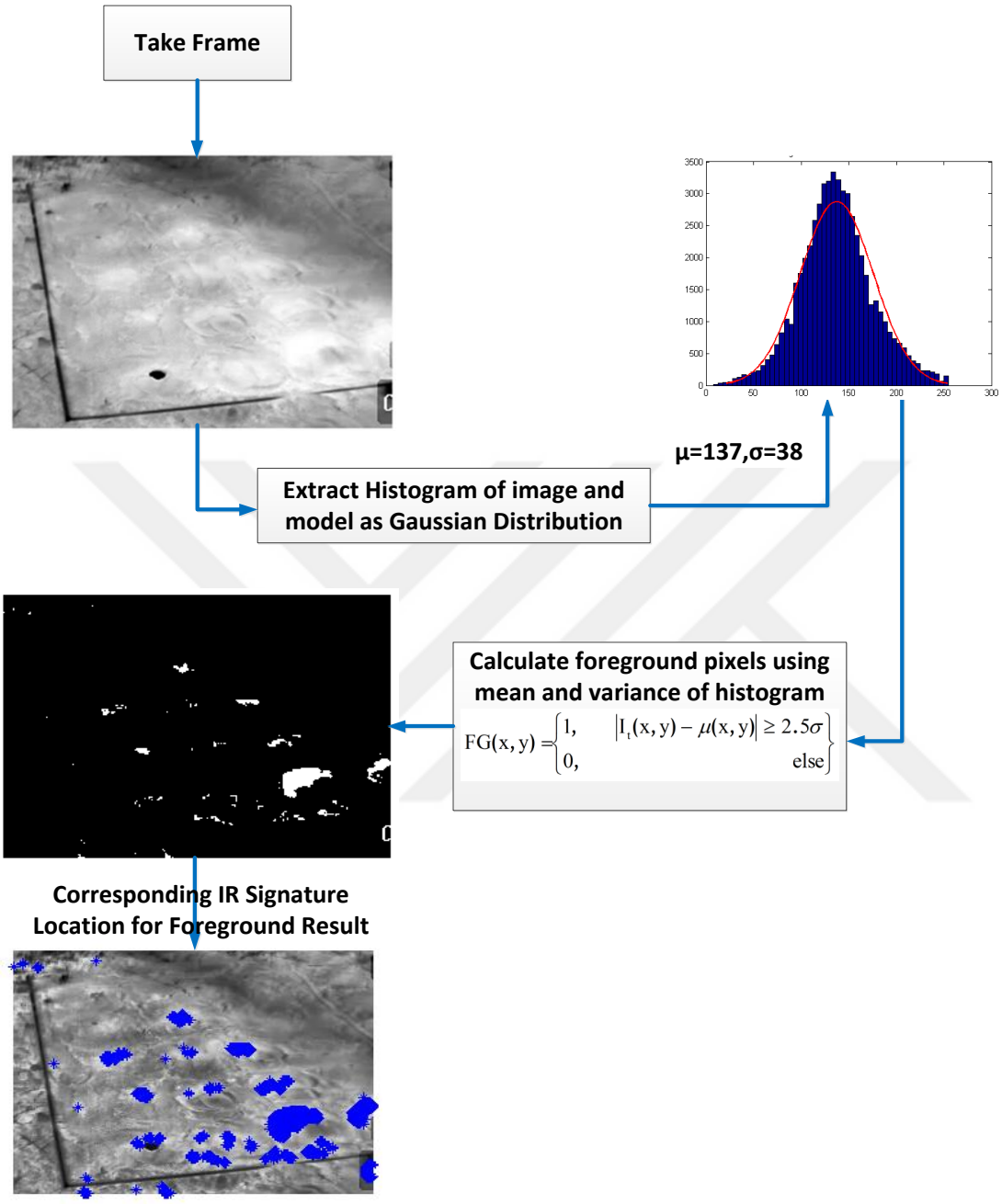

Figure 46 Gaussian Model-Based Detection Algorithm Block Diagram

According to [58], GM algorithm is implemented with variables defined in Table 12. Constant defines the ratio which is multiplied with the variance of the image to determine foreground and background.

Table 12 GM Based Landmine Detection Algorithm Parameters

GM Based Landmine Detection Algorithm Parameters		
Parameter	**Initial Value**	**Optimum Value**
Clip Limit	0,01	0,01
Alpha	0,03	0,03
Constant	2,5	2,5
Variance in Window Size	35	35

The detection results of GM algorithm for initial and optimum values are shown in Figure 47. The optimum values are observed that they are the same with initial value. The sensitivity analysis section, we will explain these results. The algorithm is detected 8 landmine locations more precisely. In this algorithm, we extract the histogram of IR image and Gaussian curve is fitted to find mean and variance of image. The constant that we use in multiplication affects the decision. For our image, we use 2.5 as optimum value. The change depending on constant and alpha value is observed in sensitivity analysis. Compared to other algorithms, GM based landmine detection has less parameter; this reduces the sensitivity to different IR images.

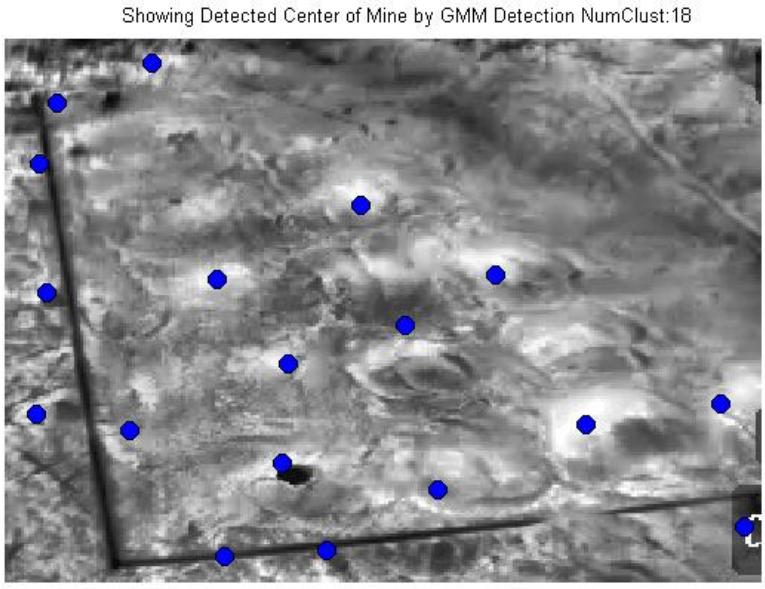

Figure 47 GM Based Landmine Detections with Initial and Optimum Values for Train Set

In Figure 48, the ROC curve for GM is given. The threshold values for this ROC are higher than the previous ones; because, the intensity values of the locations detected by GM based detection algorithm are higher.

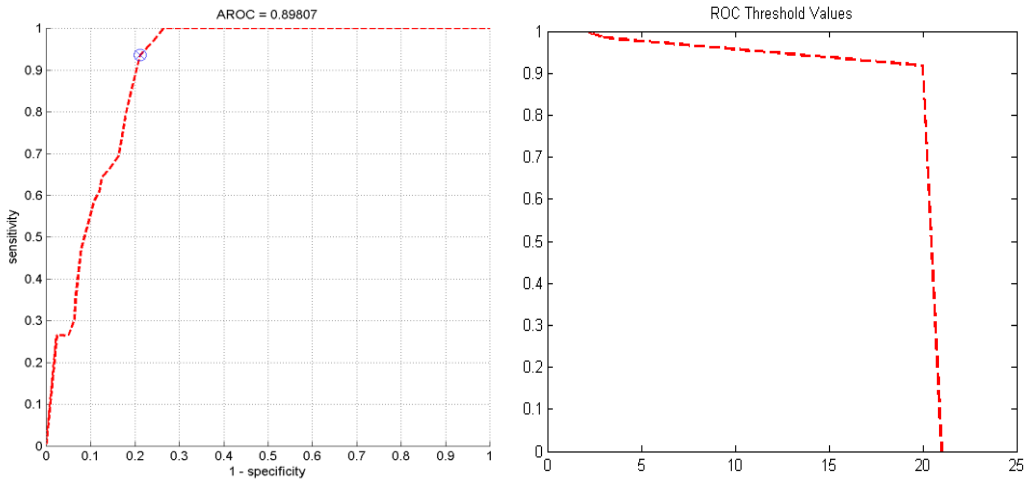

Figure 48 ROC and Threshold of GM Based Landmine Detection with Initial and Optimum Values for Train Set at Optimum Threshold

4.1.2.4 Maximally Stable Extremal Region Based Landmine Detection Algorithm and Results

In this section, MSER detection algorithm block diagram is indicated in Figure 49. The parameters for MSER detection is minimum diversity, maximum variation, minimum area and maximum area. The parameter delta in Table 13 controls how the stability is calculated. A stable region has a small variation in $|R(+\Delta)-R|$ where R is the interested region. Variation parameter is limited by MaxVariation in Table 13. MinDiversity describes the similarity to its parent MSER. MinArea is too small and MaxArea is too big area information for region.

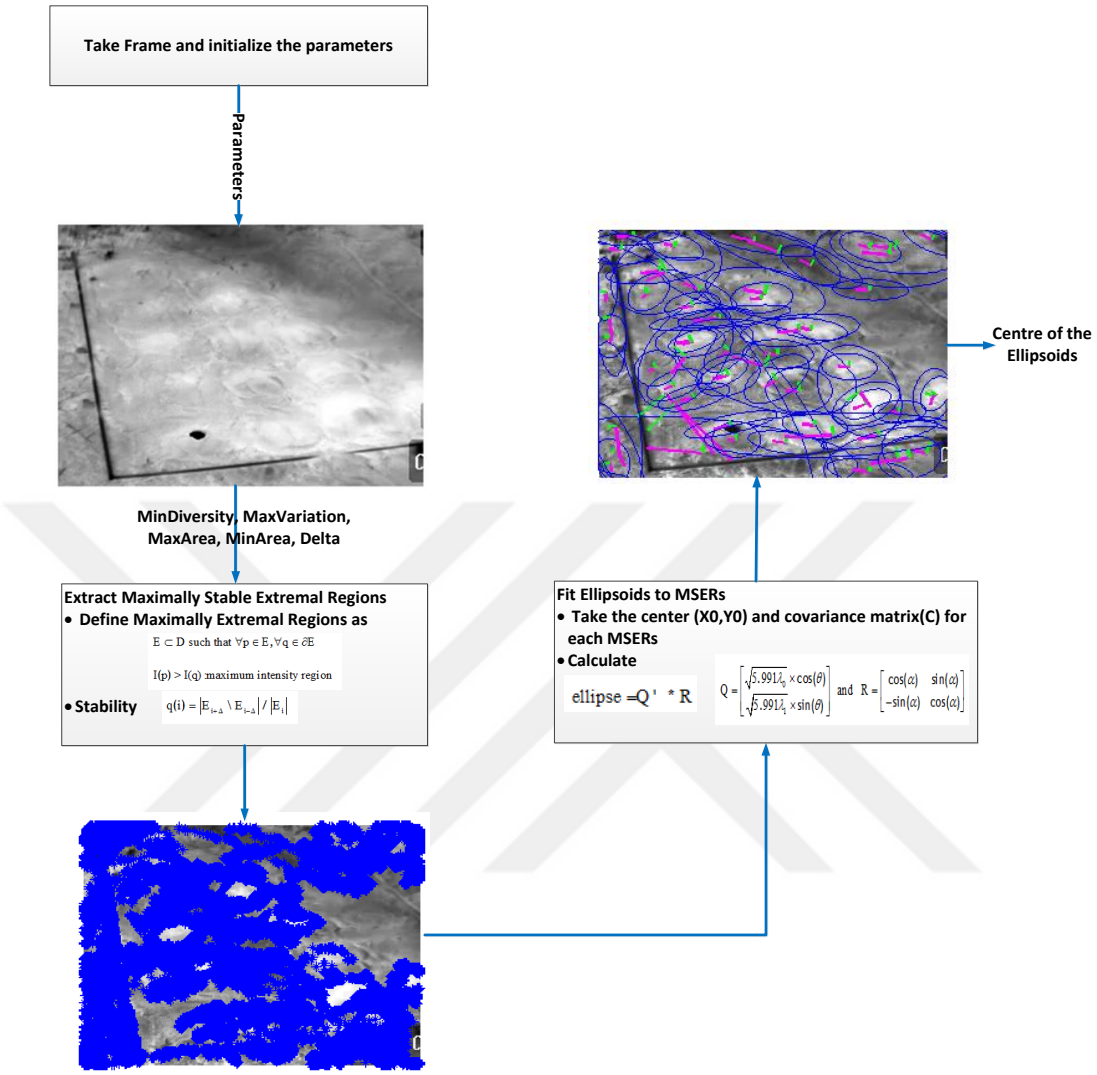

Figure 49 Maximally Stable Extremal Regions Detection Algorithm Block Diagram

According to [16], MSER algorithm is implemented with variables defined in Table 13.

Table 13 MSER Based Landmine Detection Algorithm Parameters

MSER Based Landmine Detection Algorithm Parameters		
Parameter	**Initial Value**	**Optimum Value**
Clip Limit	0,01	0,01
MinDiversity	0,8	0,5
MaxVariation	0,1	1,5
MaxArea	0,03	0,05
MinArea	0,0015	0,005
Delta	3	2,5
Variance in Window Size	35	35

The algorithm results according to both initial and optimum values are indicated in Figure 50 and Figure 52, respectively.

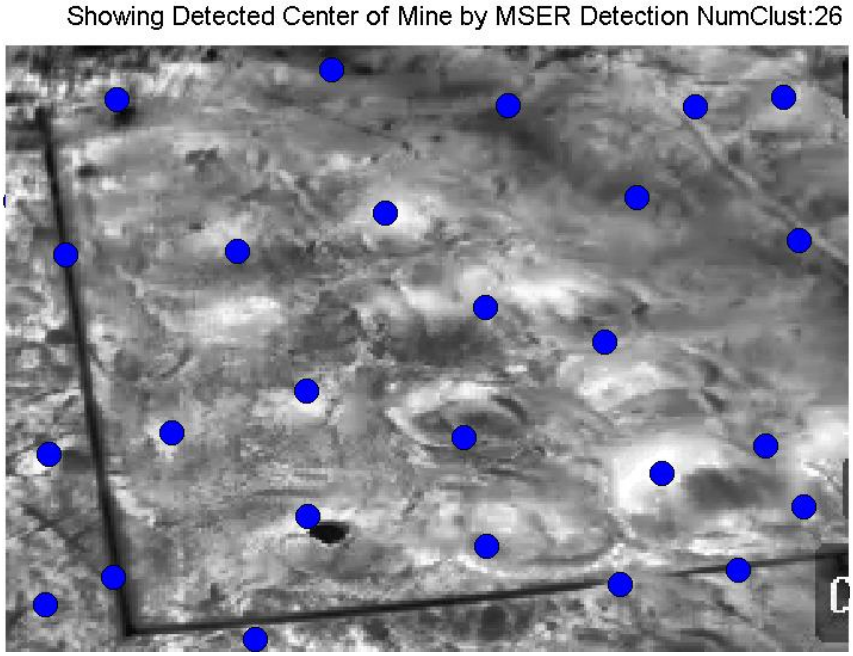

Figure 50 MSER Based Landmine Detections with Initial Value for Train Set

The corresponding ROC curve and threshold values for initial values are given in Figure 51.

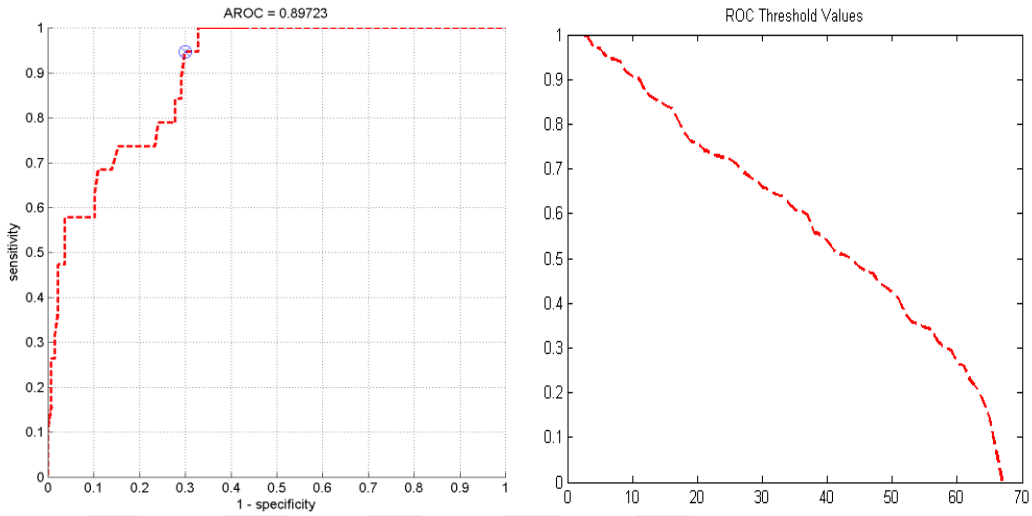

Figure 51 ROC and Threshold of MSER Based Landmine Detection with Initial Value for Train Set at Optimum Threshold

There are 8 detected landmine locations positively. The locations are so close to landmine centers. This provides more precise detection.

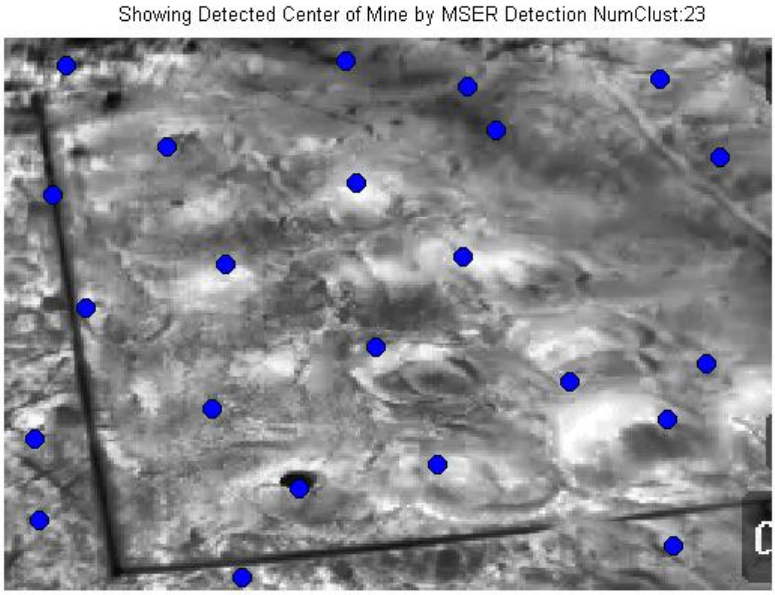

Figure 52 MSER Based Landmine Detections with Optimum Value for Train Set

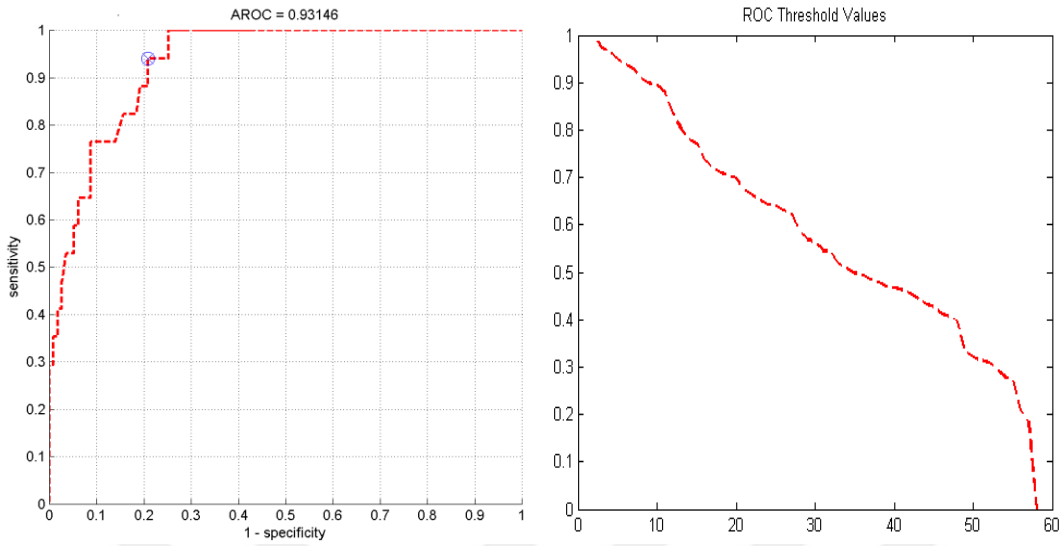

Figure 53 ROC and Threshold of MSER Based Landmine Detection for Optimum Value for Train Set at Optimum Threshold

According to Figure 51 and Figure 53, the ROC performance is highest between all other detection algorithms. The parameters stated in Table 13 affect the performance of detection. Borders create false alarms; but these will be removed in post processing step.

4.1.2.5 Fusion of FLIR Based Landmine Detection Algorithms and Results

In this section, we fuse the all detector results and the locations are detected as shown in Figure 54 and Figure 56. There are nearly 8 and 9 detected landmines for initial and optimum values respectively. The location of the 8 of them is at the center of landmines and 1 of them at the edge of landmine. The borders cause confusion, so that one of them is located near edge of landmine.

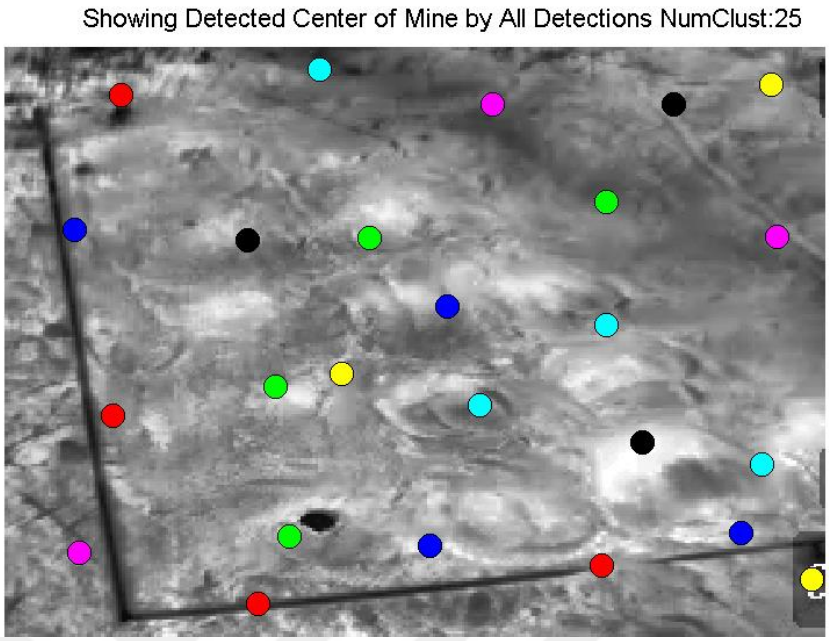

Figure 54 Fusion of Landmine Detection Algorithms with Initial Values for Train Set

The corresponding ROC curve and threshold values are shown in Figure 55. As seen in Figure 55, the ROC curve performance is increased after fusion of all detection algorithms for initial values. After we remove the points out of the borders, there will be 5 false alarm locations.

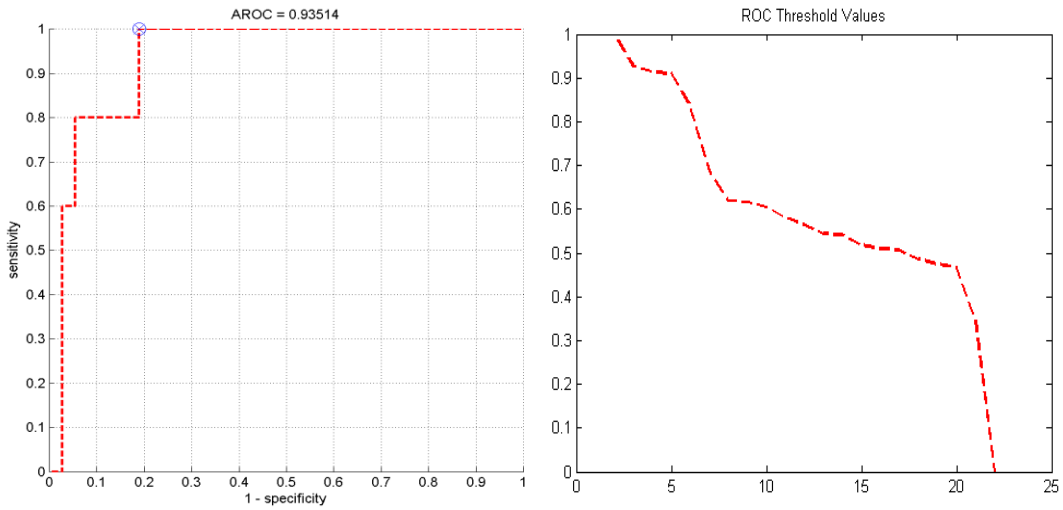

Figure 55 ROC and Threshold of Fusion Landmine Detection for Initial Values for Train Set at Optimum Threshold

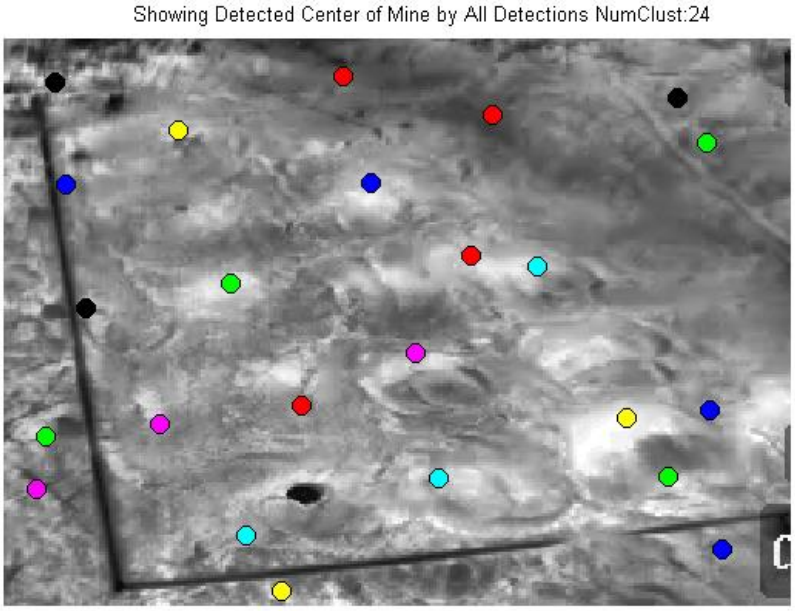

Figure 56 Fusion of Landmine Detection Algorithms with Optimum Values for Train Set

As seen in Figure 57, the ROC curve performance is increased after fusion of all detection algorithms. After we remove the points out of the borders, there will be 5 false alarm locations.

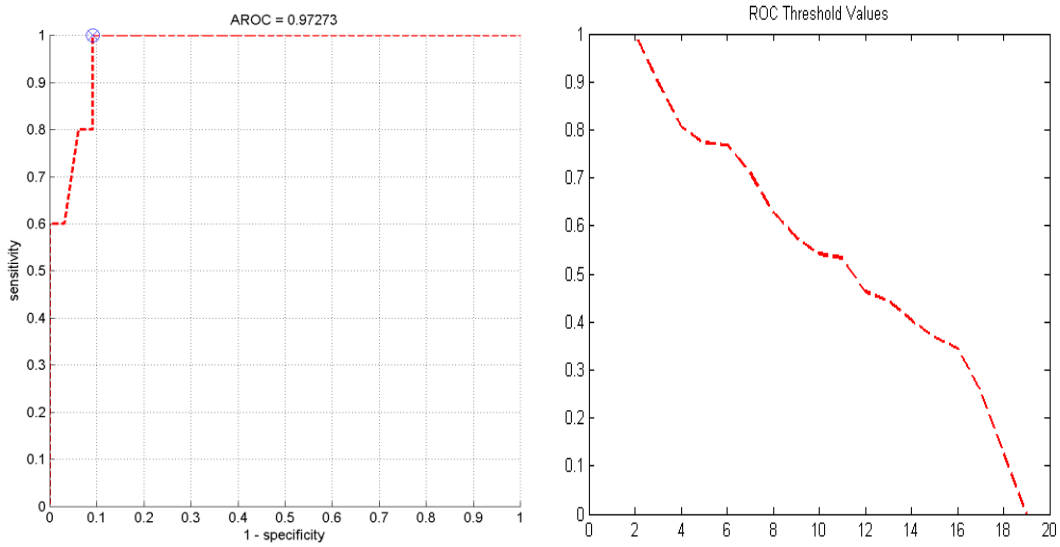

Figure 57 ROC and Threshold of Fusion Landmine Detection for Optimum Values for Train Set at Optimum Threshold

As a summary, Table 14 indicates the results for all detection algorithms. We analyze AROC, TPR and FPR metrics at optimum threshold. We can observe that while we increase both AROC and TPR at fusion of all detection algorithms, we also decrease FPR.

Table 14 Comparison of the Detection Algorithm Results at Optimum Threshold

Comparison of Detection Algorithm Results at Optimum Threshold for Train Set						
Detection Type	Metrics for Initial Values			Metrics for Optimum Values		
	AROC	TPR	FPR	AROC	TPR	FPR
Trainable Size Contrast Filter Based Detection	0,89	0,91	0,26	0,91	0,89	0,17
Corner Based Detection	0,88	0,92	0,23	0,89	0,98	0,23
GM Based Detection	0,90	0,94	0,21	0,90	0,94	0,21
MSER Based Detection	0,90	0,94	0,30	0,93	0,94	0,21
Fusion of Detection Algorithms	0,94	1,00	0,19	0,97	1,00	0,09

In Table 14, we could observe that GM and MSER based detection algorithms have better results compared to Trainable Size Contrast Filters and Corner based detection algorithms. GM has the lowest variable and MSER has the best ROC curve result for optimum values. Fusion of all detection algorithms increase ROC curve besides increasing the precision of detection. Additionally, we can observe from Table 15, there is a relation between AROC and corresponding weights. In our calculation, we take complement of AROC which equals to AAC (Area above ROC) and we try to find values which are minimizes the area when they multiplicated with AAC.

Table 15 Weights for Fusion Algorithms at Optimum Threshold

	WEIGHTS					
	Initial Values			Optimum Values		
Detection Type	CMA-ES Result	Ratio	BW	CMA-ES Result	Ratio	BW
Trainable Size Contrast Filter Based Detection	1.9222e-14	0.2629	30	1.9167e-14	0.2377	30
Corner Based Detection	2.1443e-15	0.0293	30	3.0439e-15	0.0377	30
GM Based Detection	2.3320e-14	0.3190	30	2.0946e-14	0.2597	30
MSER Based Detection	2.8423e-14	0.3888	30	3.7492e-14	0.4649	30

We also analyze AROC, TPR and FPR at fixed FPR = 0.25. The aim is to observe true positive rates and area under ROC curve performance under fixed false alarm rate. The first analysis is done for initial values. We process all detection algorithms at fixed FPR = 0.25. Figure 58 shows the fusion of detection algorithms ROC curve

and corresponding threshold value at FPR = 0.25. The blue point on ROC curve assigns the FPR = 0.25.

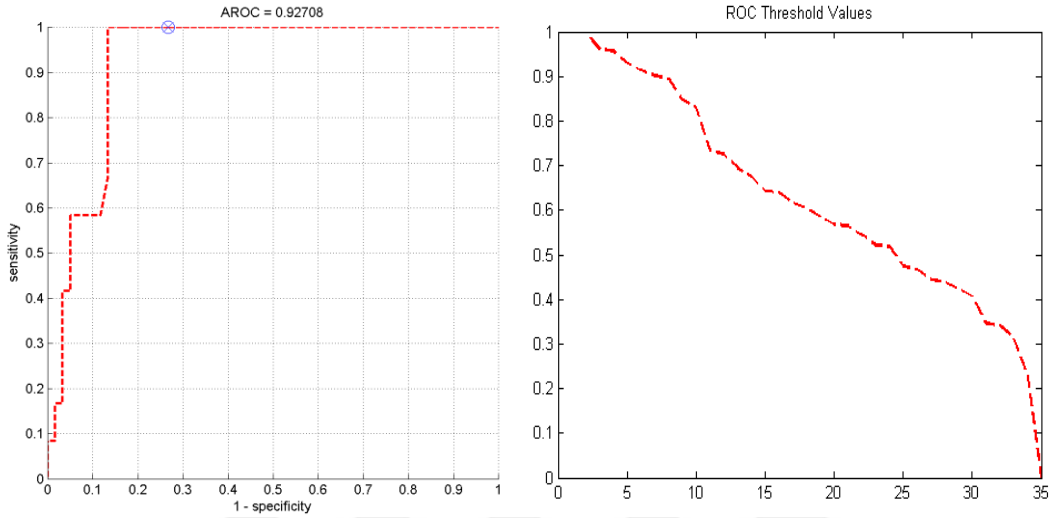

Figure 58 ROC and Threshold of Fusion Landmine Detection with Initial Values for Train Set at Fixed FPR = 0.25

The second analysis is processed for optimum values. The all detection algorithms at optimum values are run at fixed FPR = 0.25. The ROC curve and corresponding threshold values are given in Figure 59.

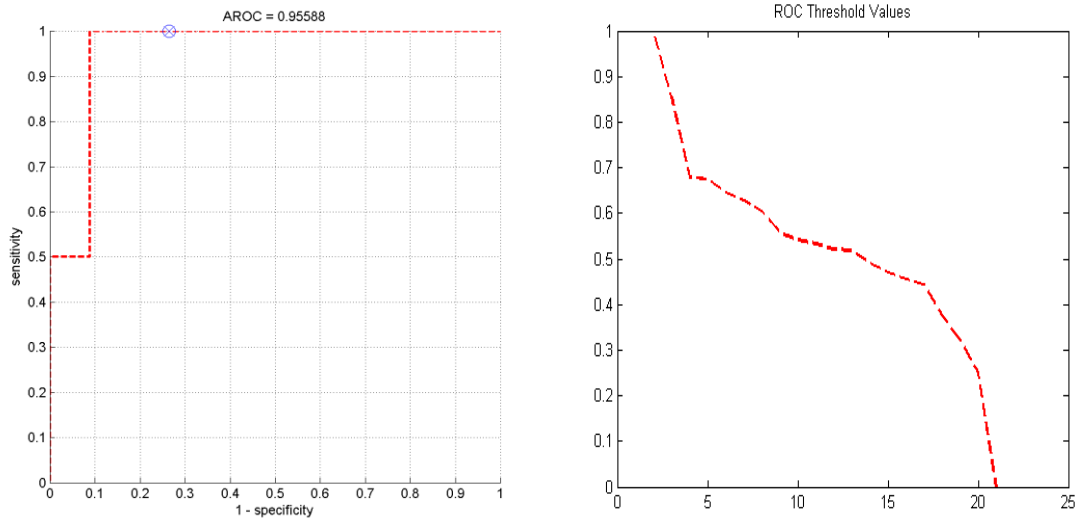

Figure 59 ROC and Threshold of Fusion Landmine Detection with Optimum Values for Train Set at Fixed FPR = 0.25

There is also a table which summarizes the all detection algorithms performance at fixed FPR = 0.25. Table 16 indicates the summary of performance metrics for all detection algorithms and fusion at fixed FPR = 0.25.

Table 16 Comparison of the Detection Algorithm Results at Fixed FPR = 0.25

Comparison of Detection Algorithm Results at Fixed FPR = 0.25 for Train Set						
Detection Type	Metrics for Initial Values			Metrics for Optimum Values		
	AROC	TPR	FPR	AROC	TPR	FPR
Trainable Size Contrast Filter Based Detection	0,89	0,82	0,25	0,91	0,94	0,25
Corner Based Detection	0,88	0,97	0,25	0,89	0,98	0,25
GM Based Detection	0,90	1,00	0,25	0,90	1,00	0,25
MSER Based Detection	0,90	0,79	0,25	0,93	0,94	0,25
Fusion of Detection Algorithms	0,93	1,00	0,25	0,96	1,00	0,25

According to Table 16, we observe that both AROC and TPR metrics increase under fixed FPR. Under both optimum threshold and fixed FPR, we increase both AROC and TPR rate when we fuse all landmine detection algorithms.

4.1.2.6 Sensitivity Analysis of Landmine Detection Algorithms for Train Set

The first analysis is observed for Trainable Size Contrast Filters based landmine detection algorithm. At clipping limit 0.01, 14 different iterations are performed and results are compared. Our train image size is 201x280. The same windowing size requires more time to complete scanning if image size is higher. Increasing the pixel size requires bigger window size for Trainable Size Contrast Filter based landmine detection to meet requirements of high speed and low process time. In Table 35, we also compare the Trainable Size Contrast Filter based landmine detection algorithm result based on both initial and optimum values. In initial value, w_size_h is 1 and it is defined as iteration 1; however this size is acceptable if landmine is so far away from camera. In our setup, there is 2.5 meter distance from camera and first landmine location. So we increase inner window size. Window sizes are so critical; because, variance and mean values of inner and outer windows are used in decision. If window size is so smaller than landmine IR signature, landmine could not be detected. If window size is so bigger than landmine IR signature, landmine could not be detected. There is a relation window size and landmine IR signature to detect effectively. We increase window size and iteration 7 gives higher performance than

initial value called as iteration 1. If we increase window size 20, then AROC is increased. Furthermore, FPR is the lowest at iteration 7. TPR value at iteration 7 is lower than TPR value at iteration 1; however, AROC is increased and FPR is decreased. Figure 60 shows the relation between AROC, TPR and FPR for 14 different iterations.

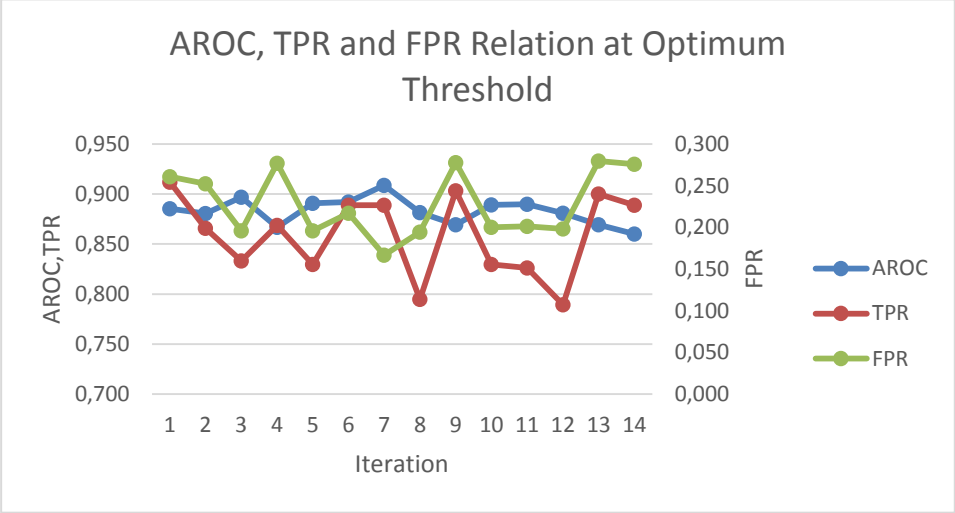

Figure 60 Comparison between AROC, TPR and FPR of Trainable Size Contrast Filter Based Detection for Train Set at Optimum Threshold

Additional analysis is processed at FPR = 0.25. When we fix the FPR, TPR and AROC have maximum value at iteration 7. Figure 61 shows the relation between AROC, TPR and FPR at fixed FPR for 14 different iterations.

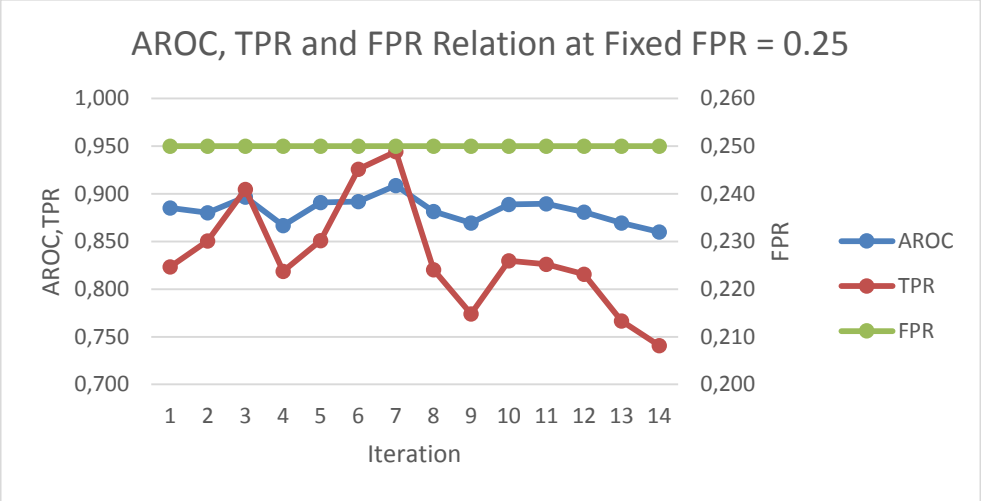

Figure 61 Comparison between AROC, TPR and FPR of Trainable Size Contrast Filter Based Detection for Train Set at Fixed FPR = 0.25

Secondly, Corner detection based algorithm performances is analysed. There are 13 iterations and implementation parameters are listed in Table 37 and Table 38. The first iteration is designed according to initial value. The Gap Size determines the gap between start and end point of edge. Smaller Gap Size results that only closed curves could be detected. In our IR frame, all curves are not closed so we increase the Gap Size as in reference. C is the ellipse axis ratio and we assign optimum C ratio as in reference. Changing the curvature angle by decreasing the T_angle affects the AROC, TPR and FPR negatively. At average, 160 degree is optimum as in reference. We also change the High and Low thresholds for edge detection. Decreasing H and increasing L provides more strong edges are become visible and less weak edges are become visible. Appearing more edges makes the decision harder at detector. Less edge improves the detection performance. As a final, we select optimum values as in iteration 10. Figure 62 shows the relation between AROC, TPR and FPR for 13 different iterations.

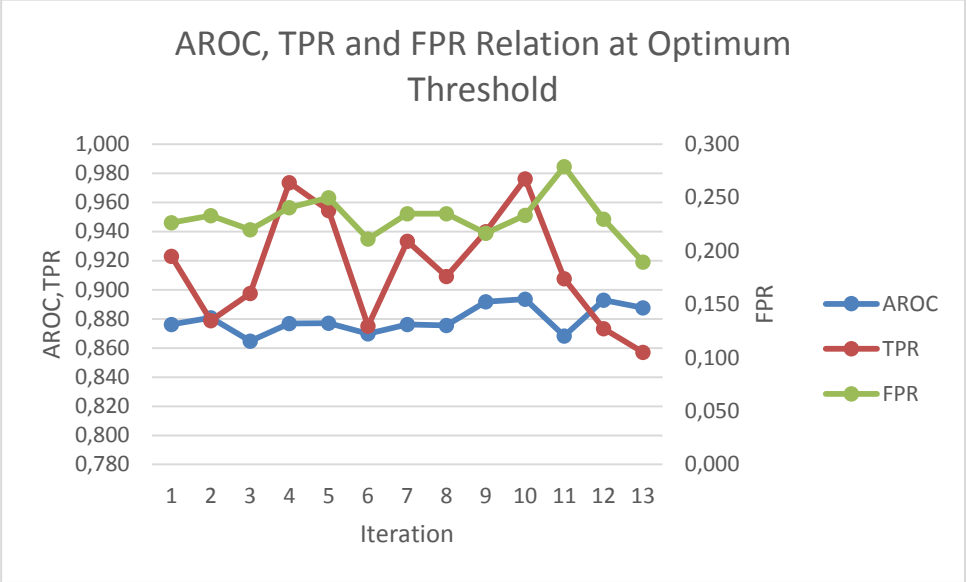

Figure 62 Comparison between AROC, TPR and FPR of Corner Based Detection for Train Set at Optimum Threshold

For Corner based landmine detection, we also analyse the performance at fixed FPR = 0.25. Figure 63 shows the relation between AROC, TPR and FPR at fixed FPR for 13 different iterations.

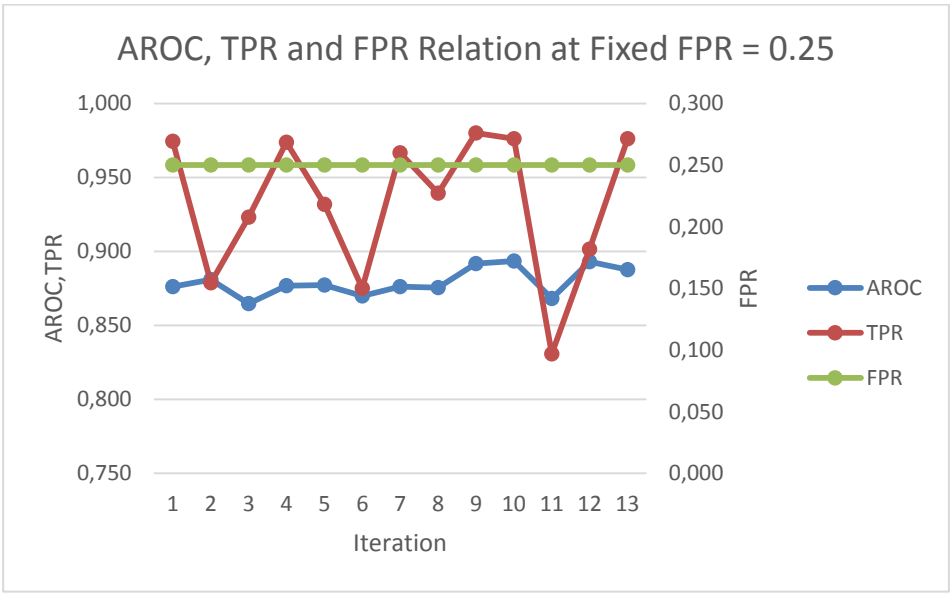

Figure 63 Comparison between AROC, TPR and FPR of Corner Based Detection for Train Set at Fixed FPR = 0.25

The third one is Gaussian Model based landmine detection algorithm parameters analysis. In this algorithm, we observe 7 different iterations. We start the detector parameters definition with initial value. In reference, the Constant value is 2.5. Decreasing the constant value causes lower performance in AROC compared to iteration 1. Alpha is the value which used in extracted histogram of frame and it does not affect so critically. In reference, the algorithm only depends on Constant value. As a final, we choose iteration 1 as indicated in reference. The critical point in GM is that GM requires only one parameter to decide whether there is foreground or background. This algorithm is much suitable for experimental environment. Figure 64 shows the relation between AROC, TPR and FPR for 7 different iterations.

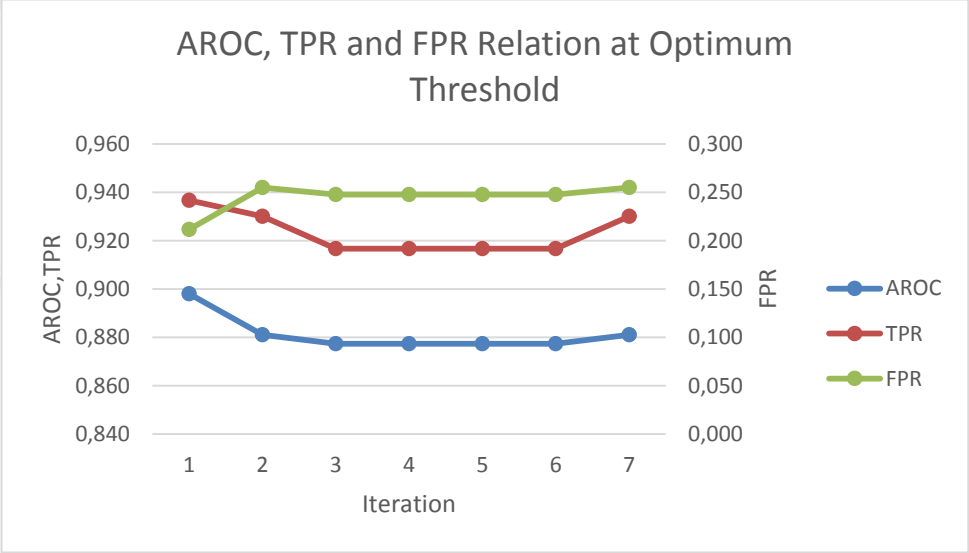

Figure 64 Comparison between AROC, TPR and FPR of GM Based Detection for Train Set at Optimum Threshold

Under fixed FPR, we analyse the AROC and TPR performance of GM based iterations. Figure 65 shows the relation between AROC, TPR and FPR for 13 different iterations. According to Figure 65, iteration 1 gives the best performance when AROC and TPR are taken into account.

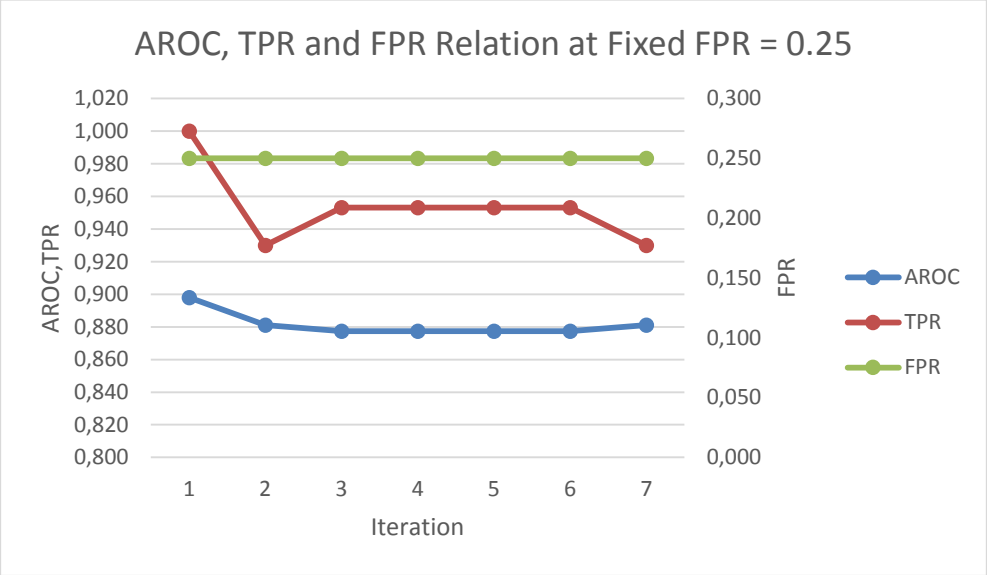

Figure 65 Comparison between AROC, TPR and FPR of GM Based Detection for Train Set at Fixed FPR = 0.25

The last algorithm is Maximally Stable Extremal Region based landmine detection. We analyse the algorithm with 13 iterations. Table 44 shows the parametric analysis for IR image. In Table 44, the first iteration parameters refer to initial values. Maxarea and minarea over an area are critical parameters which depends on figure properties. If IR signature ellipse axis ratio is high, area value could be used as small value. This condition occurs when MSER algorithm tries to find landmine which is far away from camera. In our experimental environment, IR signatures are close and they are bigger, so we should increase the area additionally, maxvariation defines the stability inside the area. When we increase the area, variations will become higher compared to small area. Small area with high variation value decrease AROC; however, high area with high variation increase AROC. We assign iteration 9 as optimum. Although MSER gives more robust results, MSER algorithm has 5 different parameters to optimize for experimental environment. The performance comparison of iterations based on AROC, TPR and FPR is shown in Figure 66.

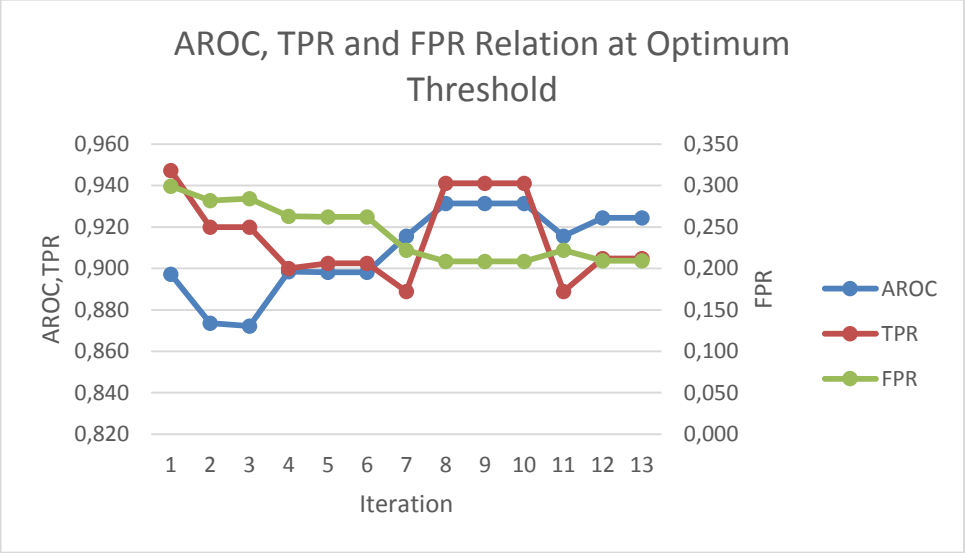

Figure 66 Comparison between AROC, TPR and FPR of MSER Based Detection for Train Set at Optimum Threshold

The AROC and TPR analysis under fixed FPR is also processed for MSER based landmine detection. Iteration 9 gives the best performance in Figure 67.

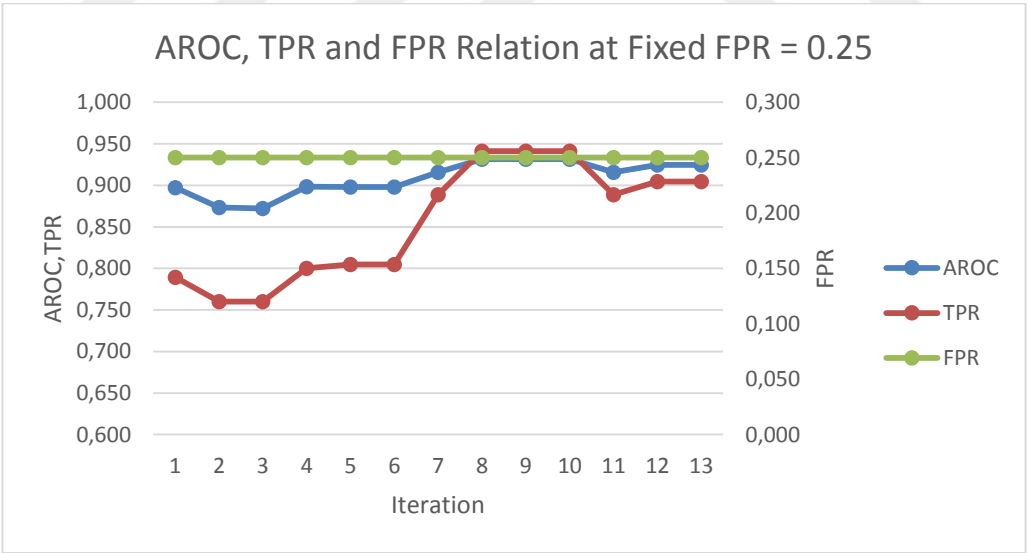

Figure 67 Comparison between AROC, TPR and FPR of MSER Based Detection for Train Set at Fixed FPR = 0.25

The results of 4 detection algorithms for both initial and optimum values are fused with 6 different Weighted-mean shift algorithm which has a variable ‘variance in

window size'. Window size determines the radius of circle which merges the detection points into mean value of circle. In Table 46, we observe that increasing the window size does not give better performance every time. Merging pixel area has a critical role for detection landmine location correctly. When we take in consideration the process time, increasing the bandwidth requires less time. However, the location number that we can find also reduces.

4.1.3 Landmine Detection Algorithms Results on Different Test Sets Captured During Day

In section 4.1.2.6, we analyse the sensitivity of algorithms and compare the optimum result with initial result. We also examine the test sets taken at morning at 10:30 and evening at 18:00. We compare the results to observe that the algorithms work in different frames properly.

The first test set is taken at 10:30, 23 August. The performance metrics of algorithms is shown in Table 17. The performance is lower than Table 14. The reason is that test set is not as smooth as Figure 28. In Table 17, we observe that we increase TPR and AROC metrics while fusing all detection algorithms, besides we decrease FPR. The example test frame at 10:30 and fusion result is shown in Figure 68.

Table 17 Comparison the Detection Algorithms Results for Optimum Values at 10:30 and 18:00 Test Sets respectively

Comparison of Detection Algorithm Results at Optimum Threshold for Test Sets						
Detection Type	Test Set 1 Metrics for Optimum Values			Test Set 2 Metrics for Optimum Values		
	AROC	TPR	FPR	AROC	TPR	FPR
Trainable Size Contrast Filter Based Detection	0,79	0,83	0,28	0,86	0,92	0,26
Corner Based Detection	0,77	0,76	0,34	0,80	0,84	0,33
GM Based Detection	0,80	0,84	0,40	0,84	0,84	0,33
MSER Based Detection	0,83	0,83	0,31	0,87	0,88	0,25
Fusion of Detection Algorithms	0,88	0,86	0,13	0,90	1,00	0,24

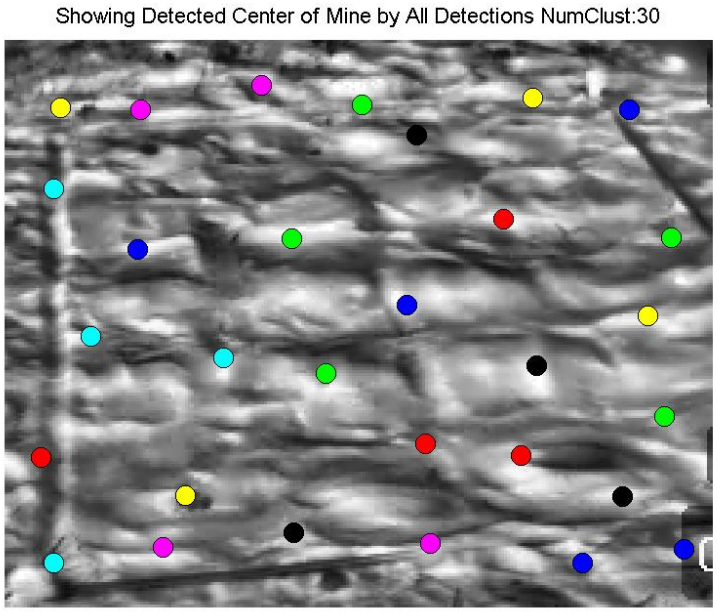

Figure 68 Fusion of Detection Algorithms in FLIR Image for Test Set at 10:30

The ROC curve and threshold values are seen in Figure 69.

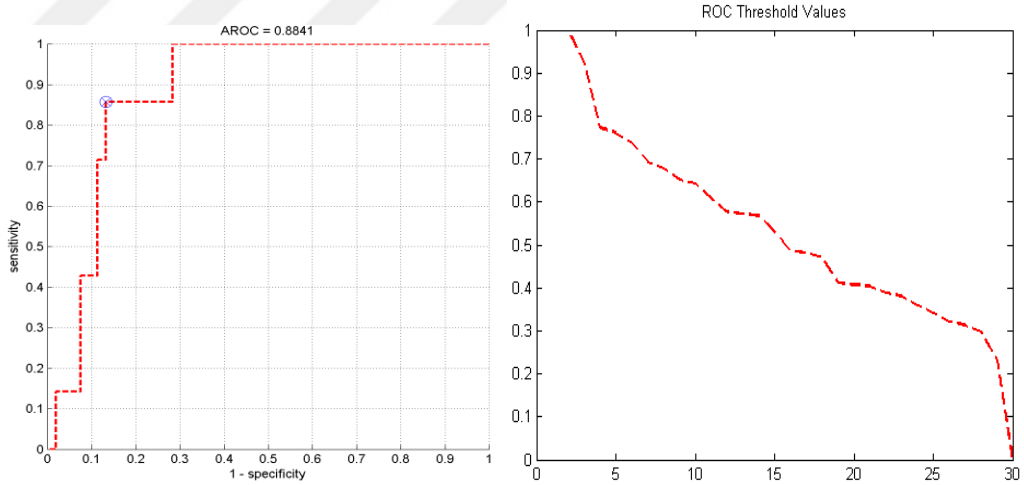

Figure 69 ROC Curve and Threshold Values for Fusion Result for Test Set at 10:30 at Optimum Threshold

For better results, IR image properties and received IR signature are so important. Smoother frame gives better performance.

Secondly, we observe the detection results at 18:00 test set. The test set is also captured at 23 August. Table 17 gives the performance metrics of each detection

algorithm and fusion. The corresponding possible landmine locations after fusion are seen in Figure 70.

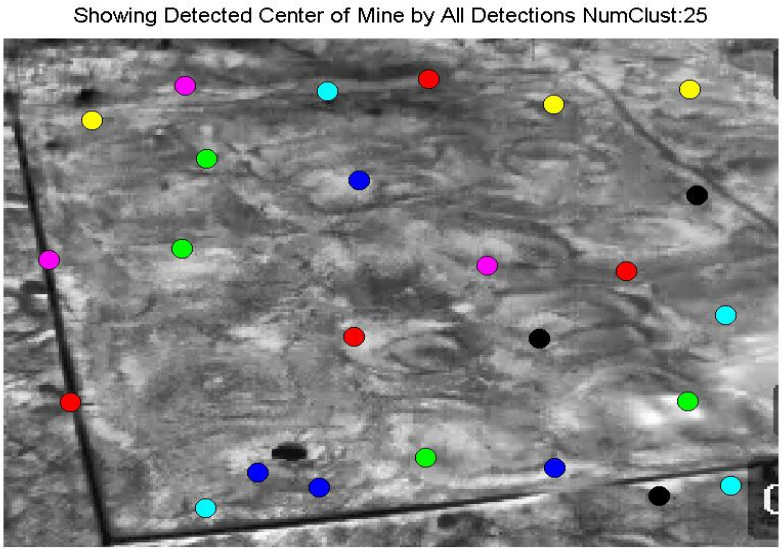

Figure 70 Fusion of Detection Algorithms in FLIR Image for Test Set at 18:00

ROC curve and threshold values of Figure 70 are given Figure 71. The performance of detection algorithms are increased after fusion. In Table 17, we observe that detection performance is increased after fusion of all detection algorithms.

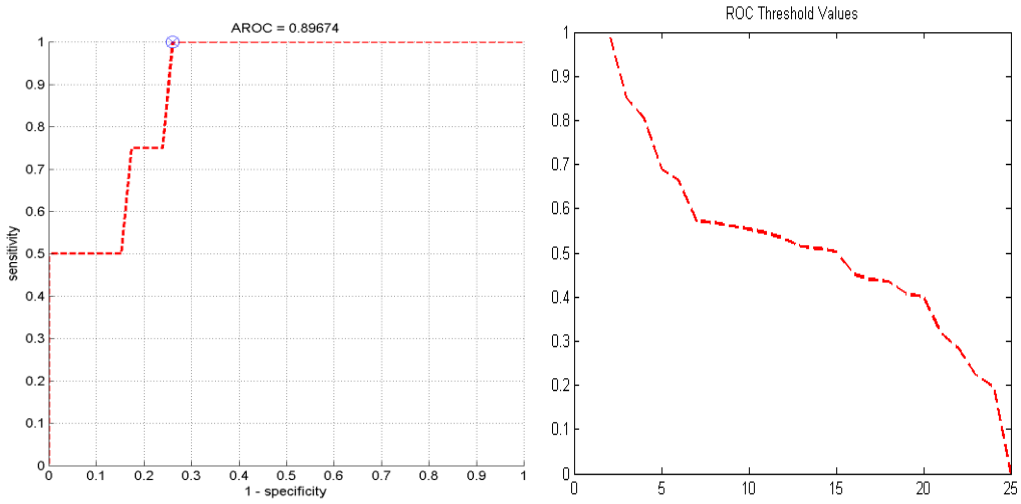

Figure 71 ROC Curve and Threshold Values for Fusion for Test Set at 18:00 at Optimum Threshold

We also analyse test sets at fixed FPR = 0.25. Table 18 shows the summary of performance metrics for all detection algorithms and fusion at fixed FPR = 0.25. In Table 18, the AROC and TPR performance increase at fixed FPR.

Table 18 Comparison the Detection Algorithms Results for Fixed FPR = 0.25 at 10:30 and 18:00 Test Sets respectively

Comparison of Detection Algorithm Results at Fixed FPR = 0.25 for Test Sets						
Detection Type	Test Set 1 Metrics for Optimum Values			Test Set 2 Metrics for Optimum Values		
	AROC	TPR	FPR	AROC	TPR	FPR
Trainable Size Contrast Filter Based Detection	0,79	0,58	0,25	0,86	0,85	0,25
Corner Based Detection	0,77	0,50	0,25	0,80	0,58	0,25
GM Based Detection	0,80	0,60	0,25	0,84	0,71	0,25
MSER Based Detection	0,83	0,69	0,25	0,87	0,81	0,25
Fusion of Detection Algorithms	0,85	0,80	0,25	0,92	1,00	0,25

The ROC curve and corresponding threshold values of fusion results for test sets are given Figure 72 and Figure 73.

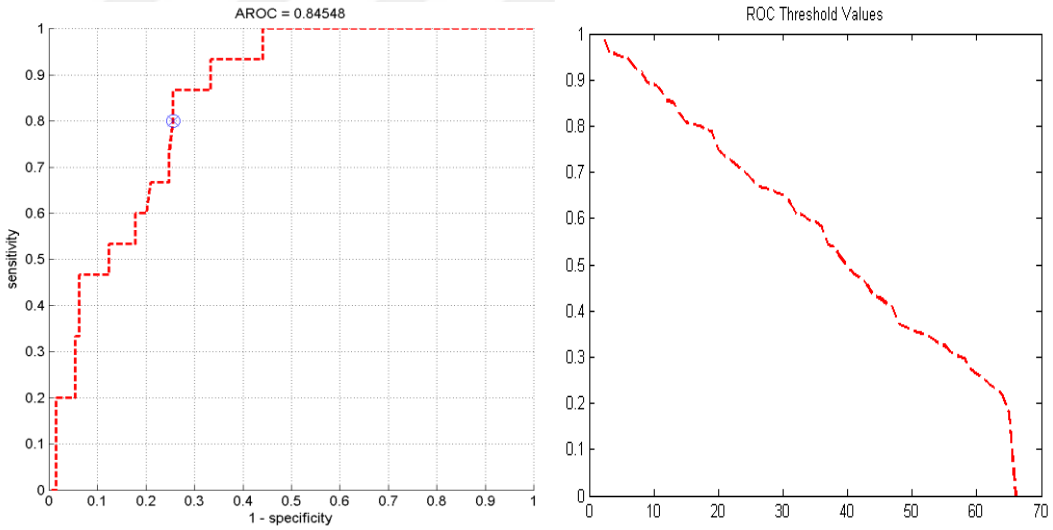

Figure 72 ROC Curve and Threshold Values for Fusion Result for Test Set at 10:30 at Fixed FPR = 0.25

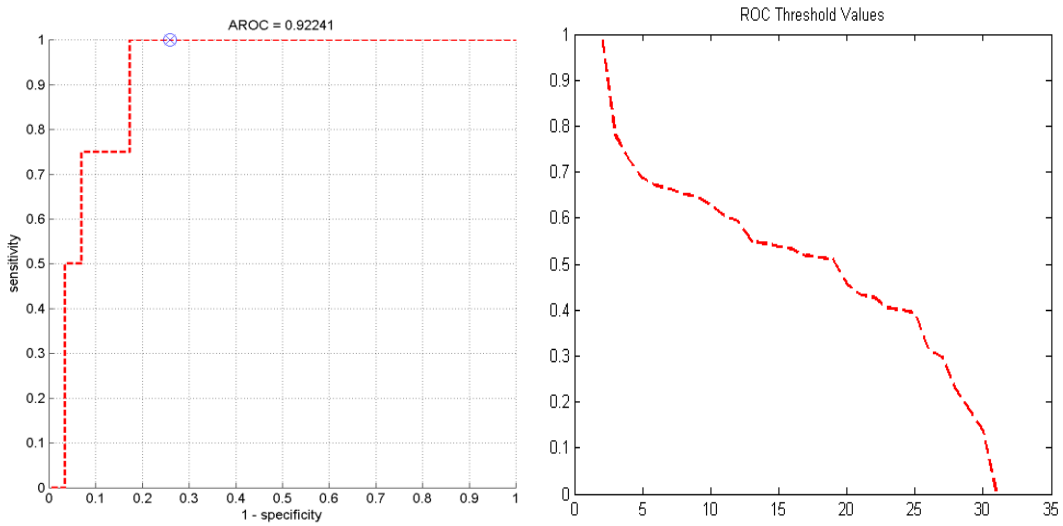

Figure 73 ROC Curve and Threshold Values for Fusion for Test Set at 18:00 at Fixed FPR = 0.25

4.1.4 Conversion of Image Pixel Location into Local Coordinate Location

At this section of thesis, our aim is to form Calibration matrix, which includes camera properties, rotation and translation information through image domain to world domain. We need world reference points which are corresponding to image domain special pixel locations. At Figure 15, we put rocks at (0,0) cm, (0,50) cm, (0,100) cm, (50,0) cm, (100,0) cm, (150,0) cm and (200,0) cm and find corresponding pixel locations in image plane. Table 19 shows the image plane pixel locations corresponding to world domain locations and Figure 74 shows the locations on FLIR example train frame.

Table 19 Reference Coordinates for Calibration

Reference 2D Image Coordinates		Reference 3D World Coordinates (cm)		
x	y	x	y	z
30	14	0	0	0
60	19	50	0	0
95	25	100	0	0
135	30	150	0	0
195	40	200	0	0
182	163	200	50	0
162	108	170	30	0
17	220	0	150	0

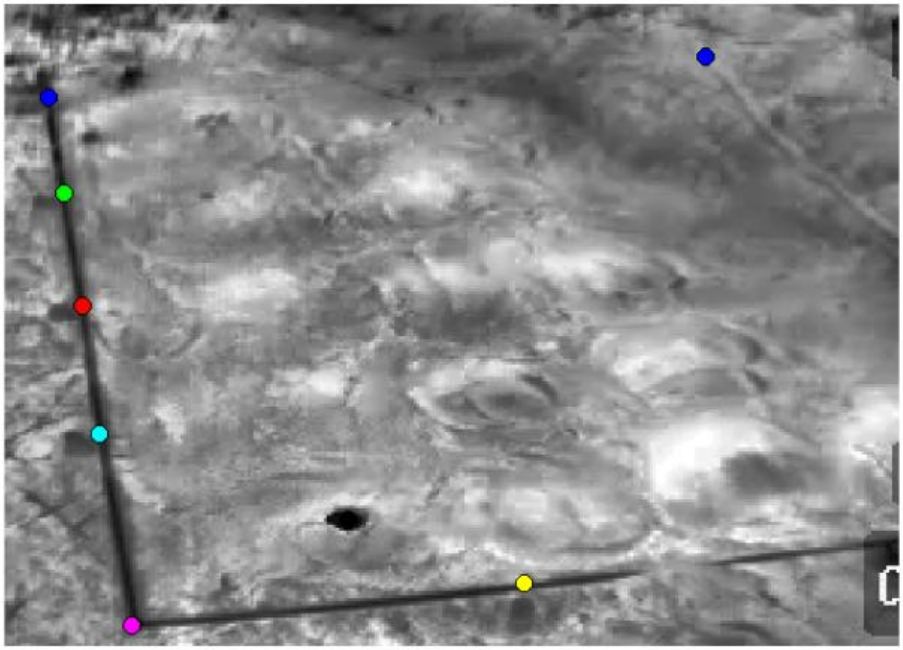

Figure 74 Reference Coordinates at Test Setup

Table 21, SVD and EigenVaule Decomposition methods have the same results; whereas, CMA-ES has slightly different at some locations. We take only 8 reference points in setup. When we increase the number of reference points, CMA-ES method result will be converge SVD method results.

Table 20 Coordinate Transformations at CMA-ES, SVD and Eigenvalue Decomposition and Difference for Detection Algorithms with Initial Values

		CMA-ES			SVD			EigenValue Decomposition			Difference Between CMA_ES&SVD		
2D Image Coordinates		3D World Coordinates (cm)			3D World Coordinates (cm)			3D World Coordinates (cm)			3D World Coordinates (cm)		
x	y	x	y	z	x	y	z	x	y	z	x	y	z
170	145	184	43	0	187	45	0	187	45	0	-3	-2	0
53	205	63	113	0	64	115	0	64	115	0	-1	-2	0
190	87	190	15	0	197	18	0	197	18	0	-7	-3	0
142	258	179	112	0	175	102	0	175	102	0	4	10	0
173	25	168	-7	0	179	-5	0	179	-5	0	-11	-2	0
111	115	125	40	0	130	43	0	130	43	0	-5	-3	0
66	83	70	32	0	68	37	0	68	37	0	2	-5	0
89	151	105	65	0	108	68	0	108	68	0	-3	-3	0
116	93	127	28	0	133	31	0	133	31	0	-6	-3	0
126	37	130	1	0	138	3	0	138	3	0	-8	-2	0
122	162	143	62	0	147	64	0	147	64	0	-4	-2	0
65	264	87	153	0	90	143	0	90	143	0	-3	10	0
13	262	-3	189	0	-3	183	0	-3	183	0	0	6	0
135	218	165	90	0	165	86	0	165	86	0	0	4	0
62	24	61	2	0	55	2	0	55	2	0	6	0	0
65	124	72	55	0	72	61	0	72	61	0	0	-6	0
16	40	0	17	0	-32	20	0	-32	20	0	32	-3	0
95	205	119	96	0	122	94	0	122	94	0	-3	2	0
20	167	7	100	0	-3	110	0	-3	110	0	10	-10	0
182	276	218	108	0	207	95	0	207	95	0	11	13	0
20	229	9	151	0	6	153	0	6	153	0	3	-2	0
166	251	200	99	0	193	90	0	193	90	0	7	9	0
167	97	173	22	0	180	25	0	180	25	0	-7	-3	0
177	204	200	71	0	197	67	0	197	67	0	3	4	0
8	108	-13	61	0	-40	73	0	-40	73	0	27	-12	0

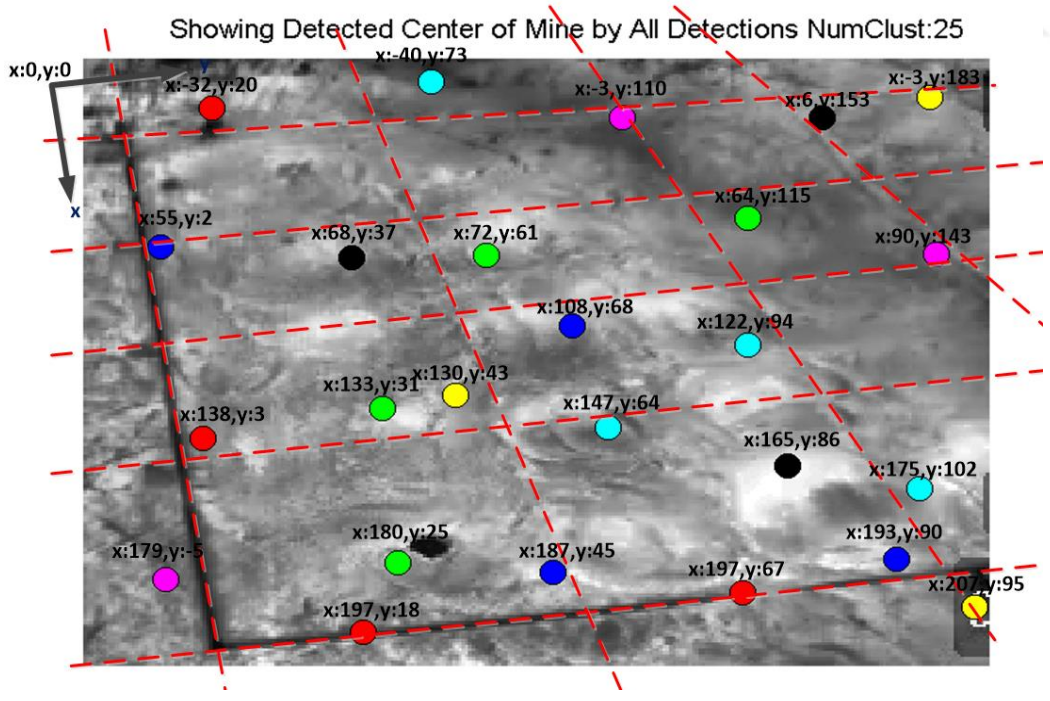

Figure 75 Local Coordinate Locations for Initial Values

Table 21 Coordinate Transformations at CMA-ES, SVD and Eigenvalue Decomposition and Difference for Detection Algorithms with Optimum Values

		CMA_ES			SVD			Eigen Value Decomposition			Difference Between CMA_ES & SVD		
2D Image Coordinates		3D World Coordinates (cm)			3D World Coordinates (cm)			3D World Coordinates (cm)			3D World Coordinates (cm)		
x	y	x	y	z	x	y	z	x	y	z	x	y	z
52	131	57	60	0	52	70	0	52	70	0	5	-10	0
37	250	63	153	0	43	154	0	43	154	0	20	-1	0
130	106	156	28	0	149	35	0	149	35	0	7	-7	0
176	86	190	16	0	186	19	0	186	19	0	4	-3	0
112	146	148	49	0	135	59	0	135	59	0	13	-10	0
33	62	0	25	0	8	32	0	8	32	0	-8	-7	0
16	18	-49	3	0	-36	4	0	-36	4	0	-13	-1	0
181	256	239	76	0	205	88	0	205	88	0	34	-12	0
156	237	216	76	0	184	87	0	184	87	0	32	-11	0
27	174	15	101	0	12	110	0	12	110	0	3	-9	0
156	155	193	43	0	177	52	0	177	52	0	16	-9	0
160	12	161	-6	0	167	-10	0	167	-10	0	-6	4	0
135	222	194	76	0	165	88	0	165	88	0	29	-12	0
96	29	99	2	0	103	2	0	103	2	0	-4	0	0
52	22	30	2	0	38	2	0	38	2	0	-8	0	0
87	81	100	25	0	98	31	0	98	31	0	2	-6	0
77	166	109	70	0	94	81	0	94	81	0	15	-11	0
81	190	122	81	0	103	92	0	103	92	0	19	-11	0
137	56	151	9	0	151	11	0	151	11	0	0	-2	0
196	99	207	18	0	202	22	0	202	22	0	5	-4	0
21	240	18	162	0	10	160	0	10	160	0	8	2	0
132	251	200	91	0	165	102	0	165	102	0	35	-11	0
141	15	145	-5	0	151	-8	0	151	-8	0	-6	3	0
14	121	-33	70	0	-24	80	0	-24	80	0	-9	-10	0

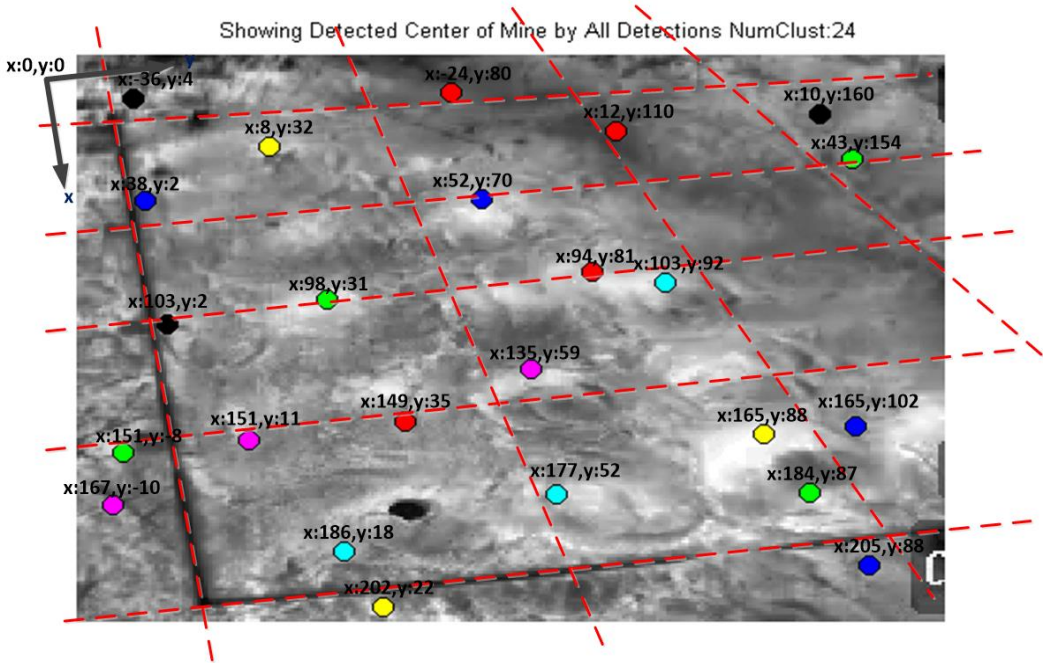

Figure 76 Local Coordinate Locations for Optimum Values

The camera calibration matrix is indicated in Table 23.

Table 22 Calibration Matrix for Detection Algorithms with Initial Values

CALIBRATION MATRIX								
CMA-ES			SVD			Eigen Value Decomposition		
-7,00059E-16	-2,19713E-17	-1,82292E-15	0,10603	-0,0238	0,83927	0,10603	-0,0238	0,83927
-1,47021E-16	-2,03768E-15	-1,02288E-15	0,01277	0,37807	0,37423	0,01277	0,37807	0,37423
1,67821E-18	-2,20348E-18	-1,08358E-16	-0,0006	0,0001	0,02585	-0,0006	0,0001	0,02585

Table 23 Calibration Matrix for Detection Algorithms with Optimum Values

CALIBRATION MATRIX								
CMA_ES			SVD			Eigenvalue Decomposition		
-5E-16	1,21E-16	-4,8E-15	0,106035	-0,02384	0,839267	0,106035	-0,02384	0,839267
-4,7E-17	-2,6E-15	-1,9E-15	0,012771	0,378072	0,374231	0,012771	0,378072	0,374231
2,86E-18	-3,6E-18	-1,3E-16	-0,00055	0,000104	0,025848	-0,00055	0,000104	0,025848

4.1.4.1 Sensitivity Analysis for Fusion Algorithms

We discuss sensitivity analysis for fusion algorithm while changing variance in window of mean shift algorithm. Variance in window determines the diameter which area is merged into center location.

Table 24 Sensitivity Analysis Metrics for Fusion

Iteration	Variance in Window
1	20
2	30
3	37
4	50

- **Fusion with Iteration 1 and Local Coordinate Conversion Results**

Figure 77 and Table 47 are the outcomes of fusion algorithm with iteration 1.

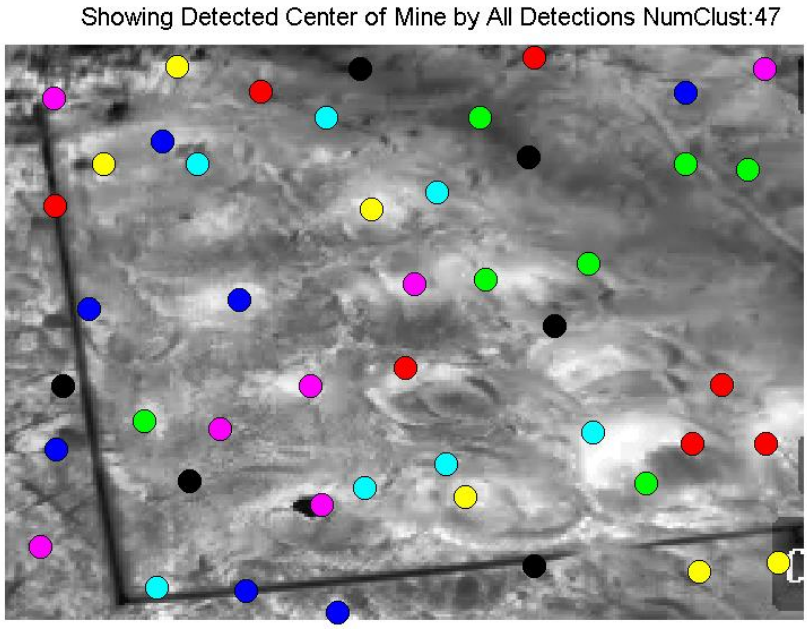

Figure 77 Algorithm Fusion Result with Iteration 1

In Table 47, we observe that SVD and Eigenvalue Decomposition methods results are the same. The maximum difference at both x and y direction between CMA-ES and SVD is 18 cm.

Table 25 represents the Calibration matrix which is found by 3 optimization method.

Table 25 Calibration Matrix at Iteration 1

CALIBRATION MATRIX								
CMA_ES			SVD			Eigenvalue Decomposition		
5,59864E-16	-3,99201E-17	2,79913E-15	0,106035	-0,02384	0,839267	0,106035	-0,02384	0,839267
1,78303E-16	2,01962E-15	-2,90431E-16	0,012771	0,378072	0,374231	0,012771	0,378072	0,374231
-1,78238E-18	1,71272E-18	1,04846E-16	-0,00055	0,000104	0,025848	-0,00055	0,000104	0,025848

- **Fusion with Iteration 2 and Local Coordinate Conversion Results**

Figure 78 and Table 48 are the outcomes of fusion algorithm with iteration 2.

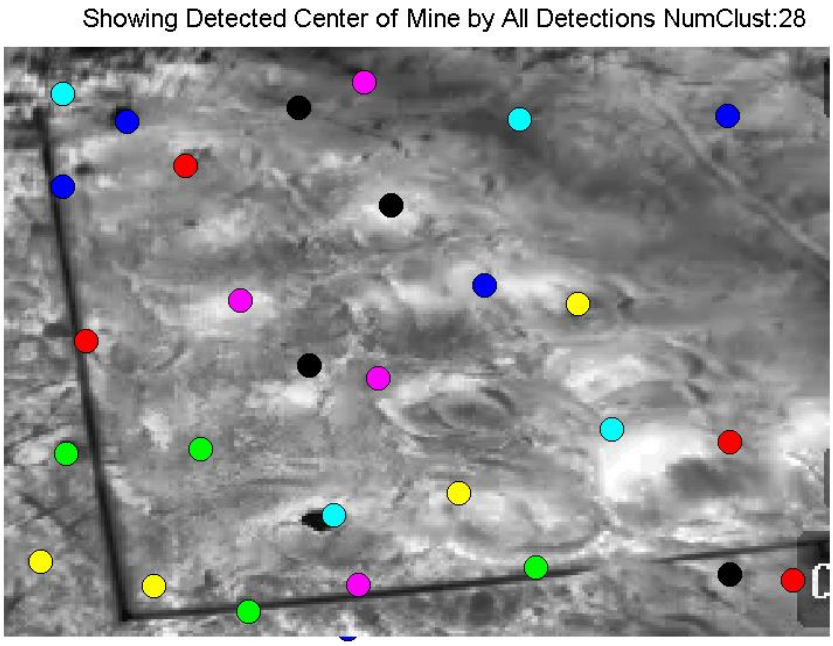

Figure 78 Algorithm Fusion Result with Iteration 2

The maximum difference at both x and y direction between CMA-ES and SVD is 10cm.

Table 26 represents the Calibration matrix which is found by 3 optimization method.

Table 26 Calibration Matrix at Iteration 2

CALIBRATION MATRIX								
CMA_ES			SVD			Eigenvalue Decomposition		
-7,7E-16	3,1E-16	-7,4E-15	0,106035	-0,02384	0,839267	0,106035	-0,02384	0,839267
-9,5E-17	-2,8E-15	-3,1E-15	0,012771	0,378072	0,374231	0,012771	0,378072	0,374231
4,51E-18	8,91E-19	-2,1E-16	-0,00055	0,000104	0,025848	-0,00055	0,000104	0,025848

- **Fusion with Iteration 3 and Local Coordinate Conversion Results**

Figure 79 and Table 49 are the outcomes of fusion algorithm with iteration 3.

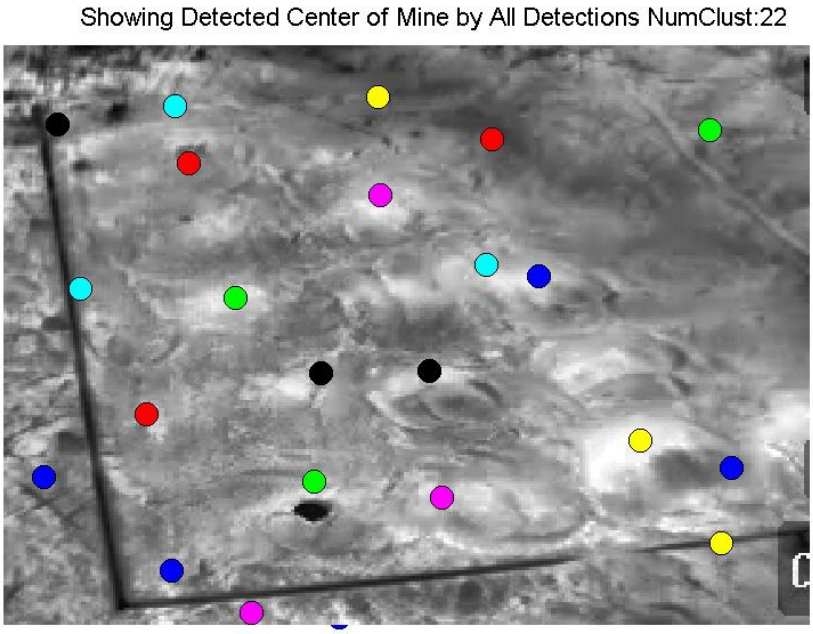

Figure 79 Algorithm Fusion Result with Iteration 3

The maximum difference at both x and y direction between CMA-ES and SVD is 6 cm. This iteration gives the best result by now. CMA-ES and SVD have the same locations.

Table 27 represents the Calibration matrix which is found by 3 optimization method.

Table 27 Calibration Matrix at Iteration 3

CALIBRATION MATRIX								
CMA_ES			SVD			Eigenvalue Decomposition		
4,4E-16	-2,1E-16	6,61E-15	0,106035	-0,02384	0,839267	0,106035	-0,02384	0,839267
1,8E-17	2,02E-15	2,39E-15	0,012771	0,378072	0,374231	0,012771	0,378072	0,374231
-3,4E-18	8,53E-20	1,46E-16	-0,00055	0,000104	0,025848	-0,00055	0,000104	0,025848

- **Fusion with Iteration 4 and Local Coordinate Conversion Results**

Figure 80 and Table 50 are the outcomes of fusion algorithm with iteration 4.

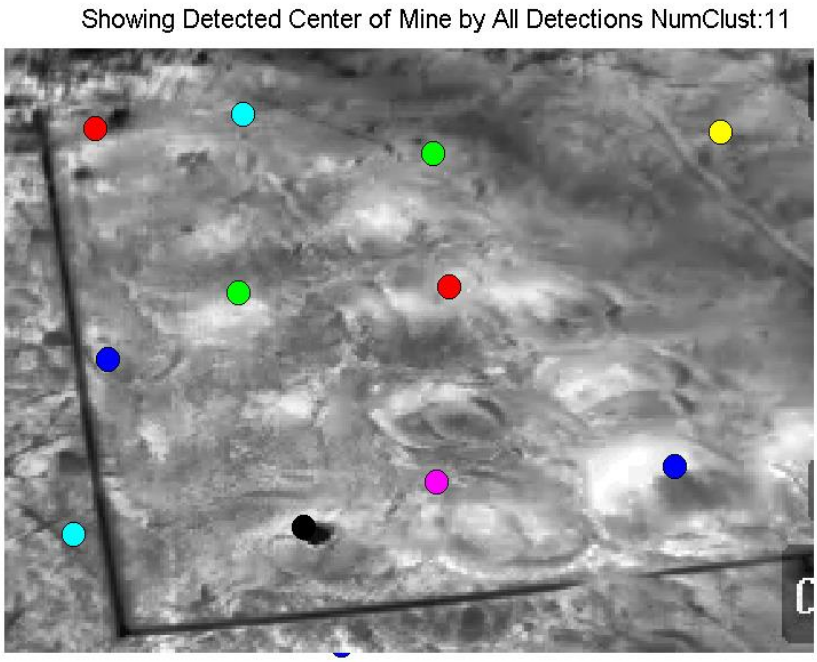

Figure 80 Algorithm Fusion Result with Iteration 4

The maximum difference at both x and y direction between CMA-ES and SVD is 55 cm. Difference starts increasing. CMA-ES and SVD have the same locations.

Table 28 represents the Calibration matrix which is found by 3 optimization method.

Table 28 Calibration Matrix at Iteration 4

CALIBRATION MATRIX								
CMA_ES			SVD			Eigenvalue Decomposition		
2,37E-16	-2,1E-16	1,61E-15	0,106035	-0,02384	0,839267	0,106035	-0,02384	0,839267
9,93E-17	4,06E-16	7,51E-17	0,012771	0,378072	0,374231	0,012771	0,378072	0,374231
-2,9E-19	-9,4E-19	4,09E-17	-0,00055	0,000104	0,025848	-0,00055	0,000104	0,025848

4.1.5 Post-Processing

Table 21 indicates the outcome of the fusion algorithm with local coordinate mapping. Our test site is (0,200) mm in x direction and (0,150) mm in y direction as seen in Figure 14. We remove out the possible alarm locations which are out of the boundary. The final result is shown in Table 29. We remove 8 false alarms with post-processing.

Table 29 Local Coordinate Results after Post-Processing for Optimum Values

		CMA_ES			SVD			Eigen Value Decomposition		
2D Image Coordinates		3D World Coordinates (cm)			3D World Coordinates (cm)			3D World Coordinates (cm)		
x	y	x	y	z	x	y	z	x	y	z
52	131	57	60	0	52	70	0	52	70	0
130	106	156	28	0	149	35	0	149	35	0
176	86	190	16	0	186	19	0	186	19	0
112	146	148	49	0	135	59	0	135	59	0
33	62	0	25	0	8	32	0	8	32	0
156	237	216	76	0	184	87	0	184	87	0
27	174	15	101	0	12	110	0	12	110	0
156	155	193	43	0	177	52	0	177	52	0
135	222	194	76	0	165	88	0	165	88	0
96	29	99	2	0	103	2	0	103	2	0
52	22	30	2	0	38	2	0	38	2	0
87	81	100	25	0	98	31	0	98	31	0
77	166	109	70	0	94	81	0	94	81	0
81	190	122	81	0	103	92	0	103	92	0
137	56	151	9	0	151	11	0	151	11	0
132	251	200	91	0	165	102	0	165	102	0

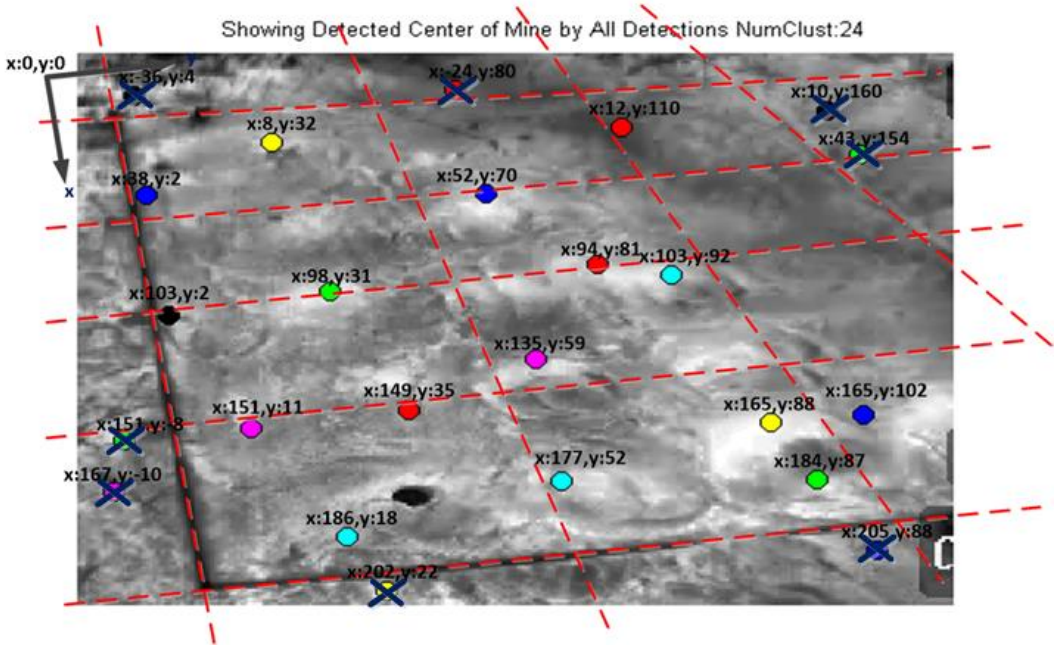

Figure 81 Local Coordinate Results after Post-Processing for Optimum Values

In this thesis, we also calculate the error of local coordinate results according to original landmine locations. Table 30 gives the original landmines location and accepted possible landmine locations. Our mock-up landmine radius is 10 cm at maximum. So, we accepted -/+ 10 cm interval around the center of original landmine locations.

Table 30 Original Landmine Location and Accepted Interval Location

	Original Mine Location			Possible Mine Location		
	3D World Coordinates (cm)			3D World Coordinates (cm)		
Mine Type	x	y	z	x	y	z
1	10	30	0	0-20	20-40	0
2	50	30	0	40-60	20-40	0
3	90	30	0	80-100	20-40	0
4	130	30	0	120-140	20-40	0
5	170	30	0	160-180	20-40	0
6	10	60	0	0-20	50-70	0
7	50	60	0	40-60	50-70	0
8	90	60	0	80-100	50-70	0
9	130	60	0	120-140	50-70	0
10	170	60	0	160-180	50-70	0
11	10	90	0	0-20	80-100	0
12	50	90	0	40-60	80-100	0
13	90	90	0	80-100	80-100	0
14	130	90	0	120-140	80-100	0
15	170	90	0	160-180	80-100	0

After defining the accepted possible landmine locations, we compare the registration result according to defined interval which is shown in Table 30.

Table 31 Comparison of the Possible Landmine Location According to Accepted Landmine Location for CMA-ES

CMA-ES			
3D World Coordinates (cm)			
x	y	z	Mine Type
57	60	0	Mine Type 7
156	28	0	Mine Type 4(error with 16 cm in x dir.)
190	16	0	No Mine
148	49	0	No mine
0	25	0	Mine Type 1 (clutter)
216	76	0	No Mine
15	101	0	Mine Type 11 (clutter)
193	43	0	No Mine
194	76	0	No Mine
99	2	0	No Mine
30	2	0	No Mine
100	25	0	Mine Type 4
109	70	0	Mine Type8 (error with 9 cm in x dir.)
122	81	0	Mine Type 14
151	9	0	No Mine
200	91	0	No Mine

Table 32 Comparison of the Possible Landmine Location According to Accepted Landmine Location for SVD

SVD			
3D World Coordinates (cm)			
x	y	z	Mine Type
52	70	0	Mine Type 7
149	35	0	Mine Type 4(error with 9 cm in x dir.)
186	19	0	No Mine
135	59	0	Mine Type 9
8	32	0	Mine Type 1 (clutter)
184	87	0	Mine Type 15 (error with 7 cm in x dir.)
12	110	0	Mine Type 11 (clutter)
177	52	0	Mine Type 10
165	88	0	Mine Type 15
103	2	0	No Mine
38	2	0	No Mine
98	31	0	Mine Type 3
94	81	0	Mine Type 13
103	92	0	Mine Type 14
151	11	0	No Mine
165	102	0	Mine Type 15

Table 33 Comparison of the Possible Landmine Location According to Accepted Landmine Location for EigenValue Decomposition

EigenValue Decomposition			
3D World Coordinates (cm)			
x	y	z	Mine Type
52	70	0	Mine Type 7
149	35	0	Mine Type 4(error with 9 cm in x dir.)
186	19	0	No Mine
135	59	0	Mine Type 9
8	32	0	Mine Type 1 (clutter)
184	87	0	Mine Type 15 (error with 7 cm in x dir.)
12	110	0	Mine Type 11 (clutter)
177	52	0	Mine Type 10
165	88	0	Mine Type 15
103	2	0	No Mine
38	2	0	No Mine
98	31	0	Mine Type 3
94	81	0	Mine Type 13
103	92	0	Mine Type 14
151	11	0	No Mine
165	102	0	Mine Type 15

In Table 31, the estimated landmine locations and corresponding mine type are listed. In CMA-ES, there are 5 possible landmine locations are listed correctly. When we observe the results for SVD and EigenValue Decomposition, 10 possible landmine locations are found in accepted interval. SVD and EigenValue Decomposition gives better performance compared to CMA-ES. However, if we

increase the reference points that we use in registration, the CMA-ES performance is also increased.

4.2 Summary of Sensitivity Analysis for Landmine Detection Algorithms

In this thesis our test setup is shown in Figure 15. In landmine detection system, FLIR camera is mounted top of the vehicle and vehicle is moving during detection. In our system, we could not find moving mechanism; so FLIR camera is fixed on tripod. We produce landmine mock-ups at different size to analyse the effects of variable depth, radius and density. Depth and density effects are not observed very clearly; however radius effect could be comparable. Bigger radius landmine causes temperature rise in wider area around it.

We take sample videos at time intervals during day. Our aim is to observe that landmine is cooler than sand at morning and hotter than sand at afternoon. While testing, we extract this property from our sample videos. Another topic is that weather also determines the imagery detection performance. The weather is rainy at last 2 days evenings of test. Moist sand is cooler than dry sand at the same atmosphere temperature and detection performance decrease under moist sand. Landmine and sand temperature are not distinguishable under moist sand condition. Later in day, moist sand temperature rises and starts getting dry and temperature difference between landmine and sand becomes detectable.

Furthermore, we analyse the performance of all detection algorithms under both optimum threshold and fixed FPR for ROC. We observe that individual detection algorithms give parallel results under both optimum threshold and fixed FPR. In Trainable Size Contrast Filter based detection, iteration 7 gives the optimum result. In Corner based landmine detection, iteration 10 gives optimum result. In GM based landmine detection, iteration 1 gives optimum result. Finally, MSER based landmine detection, iteration 9 gives optimum result. These optimum results are observed both optimum threshold and fixed FPR for ROC curve performance. Inside these detection algorithms, GM requires least number of parameters and MSER is the most robust algorithm which is more adaptive according to environmental factors.

When we integrate FLIR to landmine detection system, FLIR does not be only detection sensor in system. FLIR could be integrated with GPR system. That so, all detected points should be converted into local coordinate data which can be adapted to GPS. Camera registration is so important topic in such system. Camera properties are required for registration; however we propose a method that it is not necessary to know camera properties. Getting minimum 5 reference coordinate locations both in local coordinate and corresponding image coordinate is enough for extracting camera calibration matrix. This matrix includes camera properties, rotation and translation information. In our test setup, we put stones and meters to create our local coordinates. GPS unit could not be found during experiments. The algorithm is also suitable for getting reference points from GPS.

CHAPTER 5

CONCLUSION & FUTURE WORK

The aim of this thesis is to use FLIR imagery as pre-screener in anti-personal landmine detection system by fusing the detection algorithms. According to detection performance such as FAR, ROC and TPR and process time, various type of detection algorithm in literature are simulated and optimized. Then, optimized algorithms are processed by image which is recorded at our test setup. Matlab2014a is used for implementation of the detection algorithms.

In first part of thesis, analytical solutions for landmine detections in infrared imagery are mentioned. There are 4 different solutions which are used in literature generally. After finding landmine locations with algorithms, fusion of these algorithms according to their FAR and ROC performance characteristics is the next criteria for this thesis. Fusion algorithms are also researched and improved by assigning weight to each algorithm. The last critical topic for thesis is camera registration. There are some methods which are depending on camera properties which are time consuming before starting detection. Instead, reference points are taken to calibrate between camera image plane and local coordinate. Calibration matrix calculation methods are discussed in this part.

In the second part of thesis, implementation of algorithms is done in Matlab2014a according to part one. We prepare an experimental setup to reflect the effects for FLIR imagery. These effects can be weather, size of landmine, diurnal time variation, clutter. Our test setup is designed by including these variables There is an IR sample videos taken by FLIR camera T440 in our test setup to process the algorithms. All implemented algorithms are run at train and test sets which are taken

by our test setup. Based on the initial values, the optimization of the parameters of each algorithm is done with train set. Results of FAR and ROC of each algorithms are compared, besides all algorithms process time are recorded. Local coordinate mapping algorithm is implemented.

The first analysis is observed for Trainable Size Contrast Filters based landmine detection algorithm. At clipping limit 0.01, 14 different iterations are performed and results are compared. The same windowing size requires more time to complete scanning if pixel size is higher. Increasing the pixel size requires bigger window size for Trainable Size Contrast Filter based landmine detection to meet high speed low process time requirements. We also compare the Trainable Size Contrast Filter based landmine detection algorithm result based on both initial and optimum values. In initial value, w_size_h is 1 and it is defined as iteration 1; however this size is acceptable if landmine is so far away from camera. In our setup, there is 2.5 meter distance from camera and first landmine location. So we increase inner window size. Window sizes are so critical; because, variance and mean values of inner and outer windows are used in decision. If window size is so smaller than landmine IR signature, landmine could not be detected. If window size is so bigger than landmine IR signature, landmine could not be detected. There is a relation window size and landmine IR signature to detect effectively. As optimum iteration, we choose iteration 7 which has the less process time maximum AROC.

Secondly, Corner detection based algorithm performances is analysed. There are 13 different iterations which are compared. The first iteration is designed according to initial value. The Gap Size determines the gap between start and end point of edge. Smaller Gap Size results that only closed curves could be detected. In our IR train set, all curves are not closed so we increase the Gap Size as in reference. C is the ellipse axis ratio and we use value as in reference. We also change the High and Low thresholds for edge detection. Decreasing the increasing the L provides more edges are became visible. However, more edges cause more difficult analysis for detector. As optimum iteration, we select iteration 10.

The third one is Gaussian Model based landmine detection algorithm parameters analysis. In this algorithm, we observe 7 different iterations. We start the detector parameters definition with initial value. In reference, the Constant value is 2.5. Decreasing the constant value causes lower performance in AROC compared to iteration 1. As a final, we choose iteration 1 as indicated in reference. The critical point in GM is that GM requires only one parameter to decide whether there is foreground or background. This algorithm is much suitable for experimental environment.

The last algorithm is Maximally Stable Extremal Region based landmine detection. We analyse 13 iterations. Maxarea and minarea over an area are critical parameter which depends on figure properties. If IR signature ellipse axis ratio is high, area value could be used as small value. This condition occurs when MSER algorithm tries to find landmine which is far away from camera. In our experimental environment, IR signatures are close and they are bigger, so we should increase the area; additionally, maxvariation defines the stability inside the area. When we increase the area, variations will become higher compared to small area. Small area with high variation value decrease AROC; however, high area with high variation increase AROC. The 9^{th} iteration gives the optimum performance for MSER based detection algorithm. Although MSER has good results, MSER algorithm has 5 different parameters to optimize for experimental environment. As a comparison between all detection algorithms, GM has the least number of parameters which provides to apply different frame easily and MSER is the most robust algorithms while environmental changes are affecting IR imagery. The landmines locations should be further from each other for Corner based detection and frame size should not be high for Trainable Size Contrast Filter based detection.

All detection algorithm performances are calculated under both optimum threshold and fixed FPR. According to analysis, we compare detection results based on AROC, TPR and FPR and we observe that under both conditions, optimum values give parallel results. The results of 4 detection algorithms for both initial and optimum values are fused with Weighted-mean shift algorithm which has a variable ‘variance

in window size'. Window size determines the radius of circle which merges the detection points into mean value of circle. Merging pixel area has a critical role for detection landmine location correctly. When we take in consideration the process time, increasing the window size requires less time. However, the location number that we can find also reduces. At final, we put reference points while recording; so we could perform the local coordinate mapping with real coordinate locations. We processed image with bright intensity however our algorithm is compatible to video and dark intensity regions. At post-processing step, we remove the possible landmine locations which are not inside the boundary of test area. We can find 10 acceptable possible landmine locations with SVD algorithm and we have 12 buried landmines in test area.

In the future work, our test system was fixed and this FLIR system actually is integrated moving vehicle in usage area. If we could find this moving mechanism, we could adapt our algorithm for this type application. We used stones for reference points. In landmine detection system, there is a GPS unit which creates world coordinates data. While integration of detection algorithm, GPS data could be used; because it is also compatible to get data from GPS. We used sandbox in test setup. This algorithm performance should be experienced in field and effects of clutter should be analysed. As conventional method, GPR system is used as landmine detector. However, GPR has short stand-off distance and process time is long. To increase short stand-off distance in low processing time, additional sensor should be used. In FLIR and GPR combination, FLIR takes responsibility for pre-screener. When we consider this GPR and FLIR system, we will fuse these two systems. The world coordinates which are found by FLIR pre-screener will be sent to GPR system to scan only these locations. These will increase the standoff distance, decrease process time and propose the moving faster capability to vehicle.

REFERENCES

[1] The International Campaign to Ban Landmines (ICBL), 2009. Available: http://www.icbl.org/en-gb/problem/why-landmines-are-still-a-problem.aspx.

[2] R. Bello, "Literature Review on Landmines and Detection Methods," *Frontiers in Science*1, pp. 27-42, 2013.

[3] Transitioning Mine Action Programmes to National Ownership. Geneva International Center for Humanitarian Demining, 2012. Available: http://www.gichd.org/fileadmin/GICHD/topics/transition/Transition-Cambodia-CaseStudy-Mar2012.pdf

[4] L. M. Collins, L. G. Huettel, W. A. Simpson and S. L. Tantum, "Sensor Fusion ıf EMI and GPR Data for Improved Landmine Detection," J. T. Broach, R. S. Harmon and G. J. Dobeck Editors, *SPIE Detection and Remediation Technologies for Mines* and *Minelike Targets VII*, pp. 872-879, 2002.

[5] P. Gao, S. Tantum and L. Collins, "Single Sensor Processing and Sensor Fusion of GPR and EMI Data for Landmine Detection," *SPIE Conference on Detection and Remediation Technologies for Mines and Minelike Targets IV, Orlando*, vol. 3710, pp. 1139-1148, April, 1999.

[6] P. Gao, L. Collins, P. M. Garberi N. Geng and L. Carin, "Classification of Landmine-Like Metal Targets Using Wideband Electromagnetic Induction," *IEEE Transactions on Geoscience and Remote Sensing,* vol. 38, no. 3, pp. 1352-1361, May, 2000.

[7] J. N. Wilson, P. Gader, W. H. Lee, H. Frigui and K. C. Ho, "A Large-Scale Systematic Evaluation of Algorithms Using Ground-Penetrating Radar for

Landmine Detection and Discrimination," *IEEE Transactions on Geoscience and Remote Sensing*, vol. 45, no. 8, pp. 2560-2572, August, 2007.

[8] L. Peters, J. J. Daniels and J. D. Young, "Ground Penetrating Radar as a Subsurface Environmental Sensing Tool," *IEEE Proceedings of the IEEE,* vol. 82, no. 12, pp. 1802-1822, December, 1994.

[9] P. J. Chiang, S. L. Tantum and L. M. Collins "Signal Processing of Ground Penetrating Radar Data for Subsurface Object Detection," In A. C. Dubey, J. F. Harvey, J. Thomas and V. George Editors, *SPIE Detection and Remediation Technologies for Mines* and *Minelike Targets VI,* vol. 4394, pp. 470-475, 2001.

[10] S. M. Shrestha, I. Arai and Y. Tomizawa, "Landmine Detection with GPR Using Super Resolution Signal Processing Algorithm," *Tenth International Conference on Ground Penetrating Radar,* pp. 705-708, June 21-24, 2004.

[11] C. R. Ratto, P. A. Torrione and L. M. Collins, "Context-Dependent Feature Selection for Landmine Detection with Ground-Penetrating Radar," R. S. Harmon, J. T. Broach and J. H. Holloway Editors, *SPIE Detection and Sensing of Mines, Explosive Objects and Obscured Targets XIV,* vol. 7303, pp. 730327-1 – 730327-12, 2009.

[12] R. T. Sakaguchi, K. D. Morton, L. M. Collins and P. A. Torrione, "Physics-Based Deformations of Ground Penetrating Radar Signals to Improve the Detection of Buried Explosives," S. S. Bishop and J. C. Isaacs Editors, *Detection and Sensing of Mines, Explosive Objects, and Obscured Targets XIX*, vol. 9072, pp. 9072P-1 – 9072P-11, 2014.

[13] D. T. Anderson, J. M. Keller and O. Sjahputera, "Algorithm Fusion in Forward Looking Long Wave Infrared Imagery for Buried Explosive Hazard Detection," R. S.Harmon, J. H. Holloway and J. T. Broach Editors, *Detection and Sensing of Mines, Explosive Objects, and Obscured Targets XVI,* vol. 8017, pp. 801722-1 – 801722-12, 2011.

[14] D. M. Donskoy, "Resonance and Nonlinear Seismo-Acoustic Land Mine Detection," *Humanitarian Demining: Innovative Solutions and Challenges of Technology*, pp. 392, February, 2008.

[15] K. Stone, J. M. Keller, M. Popescu and C. J. Spain, "Buried Explosive Hazard Detection Using Forward-Looking Long-Wave Infrared Imagery," R. S.Harmon, J. H. Holloway and J. T. Broach Editors, *Detection and Sensing of Mines, Explosive Objects, and Obscured Targets XVI,* vol. 8017, pp. 801725-1 – 801725-15, 2011.

[16] D. T. Anderson, K. E. Stone and C. J. Spain, "Combination of Anomaly Algorithms and Image Features for Explosive Hazard Detection in Forward Looking Infrared Imagery," *IEEE Journal of Selected Topics in Applied Earth and Remote Sensing*, vol. 5, no. 1, pp. 313-323, 2012.

[17] J. M. Malof, K. D. Morton Jr., L. M. Collins and P. T. Torrione, "Fusion of Forward-Looking Infrared and Ground Penetrating Radar for Improved Stopping Distances in Landmine Detection," S. S. Bishop, J. C. Isaac Editors, *Detection and Sensing of Mines, Explosive Objects, and Obscured Targets XIX*, vol. 9072, pp. 90720W-1 – 90720W-11, 2014.

[18] S. E. Yuksel, G. B. Akar and S. Ozturk, "Fusion of Forward-Looking Infrared Camera and Down-Looking Ground Penetrating Radar for Buried Target Detection," S. Bishop, J. C. Isaac Editors, *Detection and Sensing of Mines, Explosive Objects, and Obscured Targets XX,* vol. 9454, pp. 945418-1 – 945418-14, 2015.

[19] K. E. Stone and J. Keller, "Automatic Explosive Hazard Detection in FL-LWIR and FL-GPR Data," *Thesis at University of Missouri,* Columbia, December, 2012.

[20] C. Hülsmeyer, patent DE 165 546, April, 1904.

[21] G. Leimbach and H. Löwy, patent DE 237 944, 1910.

[22] Dr. Hülsenbeck, patent DE 489 434, 1926.

[23] History of Ground Penetrating Radar Technology, 2008. Available: https://www.obonic.de/en/history-ground-penetrating-radar-technology/

[24] R. Abrahamsson, E. G. Larsson, J. Li, J. Habersat, G. Maksymonko and M. Bradley, "Elimination of Leakage and Ground-Bounce Effects in Ground-Penetrating Radar Data," *IEEE,* 2001.

[25] D. J. Daniels, "Ground Penetrating Radar," ISBN 0 86341 360 9, 2004.

[26] P. Torrione, L. Collins, F. Clodfelter, S. Frasier and I. Starnes, "Application of the LMS Algorithm to Anomaly Detection Using the Wichmann/Nitek Ground Penetrating Radar," R. S. Harmon, J. H. Holloway Jr. and J. T. Broach Editors, *Detection and Remediation Technologies for Mines and Minelike Targets VII,* vol. 5089, pp. 1127- 1136, 2003.

[27] P. A. Torrione, C. S. Throckmorton and L. M. Collins, "Performance of an Adaptive Feature-Based Processor for a Wideband Ground Penetrating Radar System," *IEEE Transactions on Aerospace and Electronic Systems,* pp. 1-10, 2006.

[28] K. C. Ho, L. Carin, P.D. Gader and J. N. Wilson, "An Investigation of Using the Spectral Characteristics from Fround Penetrating Radar for Landmine/Clutter Discrimination," *IEEE Transactions on Geoscience and Remote Sensing,* vol. 46, no. 4, pp. 1177-1191, April, 2008.

[29] R. Wu, A. Clement, J. Li, E. G. Larsson, M. Bradley, H. Habersat and G. Maksymonko, "Adaptive Ground Bounce Removal," *Electronics Letters,* vol. 37, no. 20, pp. 1250-1252, September 27, 2001.

[30] P.D. Gader, R. Grandhi, W-H. Lee and J. N. Wilson, "Feature Analysis for the NITEK Ground Penetrating Radar Using Order Weighted Averaging Operators for Landmine Detection," R. S. Harmon, J. H. Holloway Jr. and J.

T. Broach Editors, *Detection and Remediation Technologies for Mines and Minelike Targets IX*, vol. 5415, pp. 953-962, 2004.

[31] K. C. Ho and P. D. Gader, "A Linear Prediction Land Mine Detection Algorithm for Hand Held Ground Penetrating Radar," *IEEE Transactions on Geoscience and Remote Sensing*, vol. 40, no.6, pp. 1374-1384, June, 2002.

[32] P. Torrione and L. Collins, "Ground Penetrating Tracking for Improved Landmine Detection in Ground Penetrating Radar Data," *IEEE*, pp. 153-156, 2006.

[33] T. S. Huang, G. J. Yang and G. Y. Tang, "A Fast Two-Dimensional Median Filtering Algorithm," *IEEE Transactions on Acoustics, Speech and Signal Processing*, vol. ASSP-27, no. 1, pp. 13-18, February, 1979.

[34] K. Ho, P. D. Gader and J. N. Wilson, "Improving Landmine Detection Using Frequency Domain Features from Ground Penetrating Radar," *IEEE*, pp. 1617-1620, 2004.

[35] D. A. Lang, B. M. Duston, P. Torrione and L. Collins, "Three Dimensional Features to Improve Detection Using Ground Penetrating Radar," R. S. Harmon, J. H. Holloway Jr. and J. T. Broach Editors, *Detection and Remediation Technologies for Mines and Minelike Targets IX*, vol. 5415, pp. 913-922, 2004.

[36] P. Gader, W-H. Lee and J. N. Wilson, "Detecting Landmines With Ground Penetrating Radar Using Feature-Based Rules, Order Statistics and Adaptive Whitening," *IEEE Transactions on Geoscience and Remote Sensing*, vol. 42, no. 11, pp. 2522-2537-4, November, 2004.

[37] B. Widrow, J. M. Mccool, M. G. Larimore and C. R. Johnson, "Stationary and Nonstationary Learning Characteristics of the LMS Adaptive Filter," *Proc. IEEE*, vol. 64, no. 8, pp. 1151-1162, August, 1976.

[38] B. Widrow, M. Lehr, F. Beaufays, E. Wan and M. Bilello, “Adaptive Signal Processing,” 1985.

[39] Y. Nesterov, “Introduction Lectures on Convex Programming Volume 1: Basic Course,” 1998.

[40] M. M. Hadhoud and D. W. Thomas, “The Two-Dimensional Adaptive LMS (TDLMS) Algorithm,” *IEEE Transactions on Circuits and Systems,* vol. 35, no. 5, pp. 485-494, May, 1988.

[41] M. R. Azimi-Sadjadi and H. Pan, “Two-Dimensional Block Diagonal LMS Adaptive Filtering,” *IEEE Transactions on Signal Processing*, vol. 42, no. 9, pp. 2420-2429, September, 1994.

[42] S-G. Chen and Y-A. Kao, “A New Efficient 2-D LMS Adaptive Filtering Algorithm,” *IEEE International Symposium on Circuits and Systems,* pp. 299-302, May, 1993.

[43] P. A. Ffrench, J. R. Zeidler and W. H. Ku, “Enhanced Detectability of Small Objects in Correlated Clutter Using an Improved 2-D Adaptive Lattice Algorithm,” *IEEE Transactions on Image Processing,* vol. 6, no. 3, March, 1997.

[44] S-H. Yu, R. K. Mehra and T. R. Witten, “Automatic Mine Detection Based on Ground Penetrating Radar,” *SPIE Conference on Detection and Remediation Technologies for Mines and Minelike Targets IV,* vol. 3710, pp. 961-972, Orlando, Florida, April, 1999.

[45] D. Reichman, K. D. Morton Jr., L. M. Collins and P. A. Torrione, “Target Localization and Signature Extraction in GPR Data Using Expectation-Maximization and Principal Component Analysis,” S. S. Bishop and J. C. Isaacs Editors, *Detection and Remediation Technologies for Mines and Minelike Targets XIX,* vol. 9072, pp. 90720Q-1 – 90720Q- 12, 2014.

[46] D. Kalika, M. T. Knox, L. M. Collins, P. A. Torrione and K. D. Morton Jr., "Leveraging Robust Principal Component Analysis to Detect Buried Explosive Threats in Handheld Ground-Penetrating Radar Data," S. S. Bishop and J. C. Isaacs Editors, *Detection and Remediation Technologies for Mines and Minelike Targets XX,* vol. 9454, pp. 94541D-1 – 94541D-10, 2015.

[47] E. J. Candes, X. Li, Y. Ma and J. Wright, "Robust Principal Component Analysis?," *Journal of the ACM (JACM),* pp. 1-39, December 17, 2009.

[48] P. P. Gandhi and S. A. Kassam, "Analysis of CFAR in Nonhomogeneous Background," *IEEE Transactions on Aerospace and Electronic Systems,* vol. 24, no. 4, pp. 427-445, July, 1988.

[49] R. Srinivasan, "Simulation of CFAR Detection Algorithms for Arbitrary Clutter Distributions," *IEE Proc.-Radar, Sonar Navig.*, vol. 147, no. 1, pp. 31-40, February, 2000.

[50] B. N. Nelson, "Region of Interest Identification, Feature Extraction and Information Fusion in a Forward Looking Infrared Sensor Used in Landmine Detection," *IEEE,* 2000.

[51] D. T. Anderson, K. Stone, J. M. Keller and J. Rose, "Anomaly Detection Ensemble Fusion for Buried Explosive Material Detection in Forward Looking Infrared Imaging for Addressing Diurnal Temperature Variation," J. H. Holloway Jr. and J. T. Broach Editors, *Detection and Sensing Technologies for Mines, Explosives Objects and Obscured Targets XVII,* vol. 8357, pp. 83570T-1 – 83570T-15, 2012.

[52] R. C. Gonzalez, R. E. Woods and S. L. Eddins, "Digital Image Processing," *2nd Edition,* Pearson Education, 2002

[53] S. M. Pizer, E. P. Amburn, J. D. Austin, R. Cromartie, A. Geselowitz, T. Greer, B. T. H. Romeny, J. B. Zimmerman and K. Zuiderveld, "Adaptive Histogram Equalization and Its Variations," *Computer Vision, Graphics and Image Processing,* pp. 355-368, 1987.

[54] D. T. Anderson, J. Farrell, K. Stone, J. M. Keller and C. Spain, "Fusion of Algorithm Decision Maps and Spectrum Features for Detecting Buried Explosive Hazard in Forward Looking Infrared Imagery," *Applied Imagery Pattern Recognition Workshop (AIPR),* pp. 1-8, 2011.

[55] R. Ros, N. Hansen, "A Simple Modification in CMA-ES Achieving Linear Time and Space Complexity," pp. 1-22, April, 2008. Available: https://hal.inria.fr/inria-00270901

[56] Y. Cheng, "Mean Shift, Mode Seeking and Clustering," *IEEE Transactions on Pattern Analysis and Machine Intelligence,* vol. 17. No. 8, pp. 790-799, August, 1995.

[57] C. Stauffer and W. E. L. Grimson, "Adaptive background Mixture Models for Real-Time Tracking," *IEEE Computer Vision and Pattern Recognition,* vol. 2, pp. 1-7, June, 1999.

[58] C. J. Spain, D. T. Anderson, J. M. Keller, M. Popescu and K. E. Stone, "Gaussian Mixture Models for Measuring Local Change Down-Track in LWIR Imagery for Explosive Hazard Detection," R. S. Harmon, J. H. Holloway Jr. and J. T. Broach Editors, *Detection and Sensing Technologies for Mines, Explosives Objects and Obscured Targets XVI,* vol. 8017, pp. 80171Y-1 – 80171Y-15, 2011.

[59] M. Popescu, K. Stone, T. Havens, D. Ho and J. Keller, "Anomaly Detection in Forward Looking Infrared Imaging Using One Class Classifiers," R. S. Harmon, J. H. Holloway Jr. and J. T. Broach Editors, *Detection and Sensing Technologies for Mines, Explosives Objects and Obscured Targets XV,* vol. 7664, pp. 76642B-1 – 76642B-8, 2010.

[60] X. C. He and N. H. C. Yung, "Corner Detector Based on Global and Local Curvature Properties," *Optical Engineering,* pp. 057008-1 – 057008-12, May, 2008.

[61] M. Heikkilä, M. Pietikäinen and C. Schmid, “Description of Interest Regions with Local Binary Patterns,” pp. 1-32, June 30, 2008. Available: http://www.ee.oulu.fi/mvg/files/pdf/marko-pr-accepted.pdf

[62] M. Popescu, K. Stone and J. M. Keller, “Detection of Targets in Forward Looking Infrared Imaging Using a Multiple Instance Learning Framework,” R. S. Harmon, J. H. Holloway Jr. and J. T. Broach Editors, *Detection and Sensing Technologies for Mines, Explosives Objects and Obscured Targets XVI*, vol. 8017, pp. 80171Z-1- 80171Z-8, 2011.

[63] J. Matas, O. Chum, M. Urban and T. Pajdla, “Robust Wide Baseline Stereo from Maximally Stable Extremal Regions,” pp. 384-393, 2004. Available: http://cmp.felk.cvut.cz/~matas/papers/matas-bmvc02.pdf

[64] C. P. Gooneratne, S.C. Mukhopahyay and G. S. Gupta, “A Review of Sensing Technologies for Landmine Detection: Unmanned Vehicle Based Approach,” *2nd International Conference on Autonomous Robots and Agents*, December, 2004.

[65] L. Robledo, M. Carrasco and D. Mery, “A Survey of Land Mine Detection Technology,” *International Journal of Remote Sensing*, vol. 30, no. 9, pp. 2399-2410, May, 2009.

[66] P. L. Martinez, L. V. Kempen, H. Sahli and D. C. Ferrer, “Improved Thermal Analysis of Buried Landmines,” *IEEE Transactions on Geoscience and Remote Sensing*, vol. 42, no. 9, pp. 1965-1975, September, 2004.

[67] J. M. Malof, “Exploiting Multi-Look Information for Landmine Detection in Forward Looking Infrared Video,” *Master Thesis*, 2013.

[68] B. Wang and S. Fan, “An Improved Canny Edge Detection Algorithm.” *IEEE Computer Science and Engineering*, DOI 10.1109/WSCSE, 2009.

[69] Chi-Square Table. Available: http://sites.stat.psu.edu/umga/401/tables/chi-square-table.pdf

[70] T. Fawcett, "An Introduction to ROC Analysis," *Pattern Recognition Letters 27,* pp. 861-874, 2006.

[71] Emissivity of Materials. Available: http://www.infrared-thermography.com/material.htm

[72] R. R. Willey, "Emittance and Reflectance of Various Materials in the 2 to 20 micrometer Spectral Region," *SPIE Infrared, Adaptive and Synthetic Aperture Optical Systems,* vol.643, 1986.

[73] A. Bhuiyan and B. Nath, "Anti-Personnel Landmine Detection Based on GPR and IR Imaging: A Review, "*Melbourne's Research Publications,* 2006.

[74] R. L. V. Dam, B. Boerchers, J. M. H. Hendrickx and S. Hong, "Soil Effects on Thermal Signatures of Buried Non Metallic Landmines," *In the Proceedings of SPIE-Detection and Remediation Technologies for Mines and Minelike Targets VIII,* vol. 5089, pp. 1210-1218, 2003.

[75] Anti-Personnel Mine Types. Available: http://www.jmu.edu/cisr/_pages/research/munitions.shtml

[76] M. Heikkilä and M. Pietikäinen, "A Texture-Based Method for Modeling the Background and Detecting Moving Objects," *IEEE Transactions Pattern Analysis and Machine Intelligence,* pp. 657-662, 2006.

[77] M. Popescu, A.Paino, K. Stone and J. Keller, "Detection of Buried Objects in FLIR Imaging Using Mathematical Morphology and SVM," *Proc. of IEEE CISDA,* pp. 1-5, 2012.

[78] B. Tuomanen, K. Stone, T. Madison, M. Popescu, and J. Keller, "Buried Target Detection in FLIR Images Using Shearlet Features," *Proceedings of SPIE-Detection and Sensing of Mines, Explosive Objects and Obscured Targets XVIII,* vol. 8709, pp. 1-12, 2013.

[79] I. K. Sendur and B. A. Baertlein, "Techniques for Improving Buried Mine Detection in Thermal IR Imagery," *Proceedings of SPIE-Detection and*

Remediation Technologies for Mines and Minelike Targets IV, vol. 3710, pp. 1-12, 1999.

[80] Electromagnetic Spectrum. Available: https://en.wikipedia.org/wiki/Electromagnetic_spectrum

[81] J. R. White, "Herschel and the Puzzle of Infrared," *American Scientists*, vol. 100, pp. 218-225, 2012.

[82] Fundamentals of Thermal Radiation. Available: kntu.ac.ir/DorsaPax/userfiles/file/Mechanical/OstadFile/Sayyalat/Bazargan/cen58933_ch11.pdf

[83] J. R. White, "Herschel and the Puzzle of Infrared," *American Scientists*, vol. 100, pp. 218-225, 2012.

[84] SecuritySales & Integration, "History of Thermal Imaging," *FLIR*, 2011.

APPENDIX-A

SENSITIVITY ANALYSIS TABLES FOR TRAIN SET

Table 34 Trainable Size Contrast Filters Detection Algorithm Parameters with Clipping Limit = 0.01

Detection Type	Clipping Limit	Iteration	Bhattacharya Distance	Mahalanobis Distance	W_Size_v	W_Size_h	W_Pad_v	W_Pad_h
Trainable Size Contrast Filter Detection	0,01	1	0,9365	397,7208	14	1	17	38
Trainable Size Contrast Filter Detection	0,01	2	200	500	10	10	5	5
Trainable Size Contrast Filter Detection	0,01	3	200	500	10	10	10	10
Trainable Size Contrast Filter Detection	0,01	4	200	500	15	15	5	5
Trainable Size Contrast Filter Detection	0,01	5	200	500	15	15	10	10
Trainable Size Contrast Filter Detection	0,01	6	200	500	15	15	15	15
Trainable Size Contrast Filter Detection	0,01	7	200	500	20	20	20	20
Trainable Size Contrast Filter Detection	0,01	8	300	500	15	15	10	10
Trainable Size Contrast Filter Detection	0,01	9	500	500	15	15	10	10
Trainable Size Contrast Filter Detection	0,01	10	200	700	15	15	10	10
Trainable Size Contrast Filter Detection	0,01	11	200	900	15	15	10	10
Trainable Size Contrast Filter Detection	0,01	12	300	900	15	15	10	10
Trainable Size Contrast Filter Detection	0,01	13	500	900	15	15	10	10
Trainable Size Contrast Filter Detection	0,01	14	700	900	15	15	10	10

Table 35 Sensitivity Analysis for Trainable Size Contrast Filters based Detection for Optimum Threshold at Clip Limit = 0.01

Detection Type	Iteration	Threshold	Sensitivity	Specificity	AROC	Accuracy %	PPV %	NPV %	Process Time	TPR	FPR	AAC
Trainable Size Contrast Filter Detection	1	0,486	0,912	0,739	0,885	90,163	98,246	34,359	20,713	0,912	0,261	0,115
Trainable Size Contrast Filter Detection	2	0,498	0,866	0,748	0,880	86,225	99,138	14,239	379,225	0,866	0,252	0,120
Trainable Size Contrast Filter Detection	3	0,553	0,833	0,804	0,897	83,195	98,851	19,259	118,260	0,833	0,196	0,103
Trainable Size Contrast Filter Detection	4	0,490	0,869	0,723	0,867	86,504	99,174	12,595	565,104	0,869	0,277	0,133
Trainable Size Contrast Filter Detection	5	0,541	0,830	0,804	0,891	82,849	98,750	20,230	166,672	0,830	0,196	0,109
Trainable Size Contrast Filter Detection	6	0,545	0,889	0,783	0,892	88,155	98,214	34,429	79,540	0,889	0,217	0,108
Trainable Size Contrast Filter Detection	7	0,541	0,889	0,833	0,909	88,154	97,222	53,333	45,530	0,889	0,167	0,091
Trainable Size Contrast Filter Detection	8	0,541	0,795	0,806	0,881	79,544	98,649	18,035	168,916	0,795	0,194	0,119
Trainable Size Contrast Filter Detection	9	0,486	0,903	0,722	0,869	89,485	98,529	26,609	161,819	0,903	0,278	0,131
Trainable Size Contrast Filter Detection	10	0,541	0,830	0,800	0,889	82,828	98,734	20,000	196,148	0,830	0,200	0,111
Trainable Size Contrast Filter Detection	11	0,541	0,826	0,799	0,890	82,473	98,734	19,478	199,734	0,826	0,201	0,110
Trainable Size Contrast Filter Detection	12	0,541	0,789	0,802	0,881	79,012	98,649	17,219	209,768	0,789	0,198	0,119
Trainable Size Contrast Filter Detection	13	0,486	0,900	0,720	0,869	89,165	98,507	26,007	192,372	0,900	0,280	0,131
Trainable Size Contrast Filter Detection	14	0,486	0,889	0,724	0,860	88,022	98,305	26,612	187,594	0,889	0,276	0,140

Table 36 Sensitivity Analysis for Trainable Size Contrast Filters based Detection for Fixed FPR = 0.25 at Clip Limit = 0.01

Detection Type	Iteration	Threshold	Sensitivity	Specificity	AROC	Accuracy %	PPV %	NPV %	Process Time	TPR	FPR	AAC
Trainable Size Contrast Filter Detection	1	0,486	0,824	0,750	0,885	81,944	98,246	20,000	20,655	0,824	0,250	0,115
Trainable Size Contrast Filter Detection	2	0,498	0,851	0,750	0,880	84,785	99,138	12,945	379,452	0,851	0,250	0,120
Trainable Size Contrast Filter Detection	3	0,553	0,905	0,749	0,897	89,849	98,851	24,766	118,633	0,905	0,251	0,103
Trainable Size Contrast Filter Detection	4	0,490	0,819	0,745	0,867	81,683	99,174	9,910	546,644	0,819	0,255	0,133
Trainable Size Contrast Filter Detection	5	0,541	0,851	0,745	0,891	84,677	98,750	17,469	155,368	0,851	0,255	0,109
Trainable Size Contrast Filter Detection	6	0,545	0,926	0,741	0,892	91,463	98,214	39,370	75,131	0,926	0,259	0,108
Trainable Size Contrast Filter Detection	7	0,541	0,944	0,750	0,909	92,550	97,222	59,302	42,778	0,944	0,250	0,091
Trainable Size Contrast Filter Detection	8	0,541	0,821	0,749	0,881	81,745	98,649	15,760	159,252	0,821	0,251	0,119
Trainable Size Contrast Filter Detection	9	0,486	0,774	0,749	0,869	77,309	98,529	13,250	150,266	0,774	0,251	0,131
Trainable Size Contrast Filter Detection	10	0,541	0,830	0,748	0,889	82,647	98,734	15,645	180,653	0,830	0,252	0,111
Trainable Size Contrast Filter Detection	11	0,541	0,826	0,746	0,890	82,288	98,734	15,159	186,258	0,826	0,254	0,110
Trainable Size Contrast Filter Detection	12	0,541	0,816	0,744	0,881	81,277	98,649	14,955	180,162	0,816	0,256	0,119
Trainable Size Contrast Filter Detection	13	0,486	0,767	0,744	0,869	76,569	98,507	12,645	171,746	0,767	0,256	0,131
Trainable Size Contrast Filter Detection	14	0,486	0,741	0,747	0,860	74,103	98,305	12,678	166,818	0,741	0,253	0,140

Table 37 Corner Based Detection Algorithm Parameters with Clipping Limit = 0.01

Detection Type	Clipping Limit	Iteration	C	T Angle	Sigma	H	L	Endpoint	Gap Size
Corner Detection	0,01	1	1,5	160	3	0,35	0,15	1	20
Corner Detection	0,01	2	1,5	160	3	0,35	0,15	1	1
Corner Detection	0,01	3	1,5	160	3	0,35	0,15	1	10
Corner Detection	0,01	4	1	160	3	0,35	0,15	1	20
Corner Detection	0,01	5	1	160	3	0,35	0,12	1	20
Corner Detection	0,01	6	1	160	3	0,35	0,17	1	20
Corner Detection	0,01	7	2	160	3	0,35	0,15	1	20
Corner Detection	0,01	8	1,5	150	3	0,35	0,15	1	20
Corner Detection	0,01	9	1,5	170	3	0,35	0,15	1	20
Corner Detection	0,01	10	1,5	160	2,5	0,35	0,15	1	20
Corner Detection	0,01	11	1,5	160	2,5	0,25	0,15	1	20
Corner Detection	0,01	12	1,5	160	2,5	0,25	0,17	1	20
Corner Detection	0,01	13	1,5	160	2,3	0,35	0,15	1	20

Table 38 Sensitivity Analysis for Corner Detection for Optimum Threshold at Clip Limit = 0.01

Detection Type	Iteration	Threshold	Sensitivity	Specificity	AROC	Accuracy %	PPV %	NPV %	Process Time	TPR	FPR	AAC
Corner Detection	1	0,533	0,923	0,773	0,876	91,438	98,507	38,295	1,335	0,923	0,227	0,124
Corner Detection	2	0,525	0,879	0,767	0,881	87,307	98,592	25,428	0,338	0,879	0,233	0,119
Corner Detection	3	0,525	0,897	0,780	0,865	89,069	98,529	31,640	0,279	0,897	0,220	0,135
Corner Detection	4	0,498	0,974	0,759	0,877	96,165	98,551	63,197	0,349	0,974	0,241	0,123
Corner Detection	5	0,506	0,955	0,750	0,877	94,411	98,611	47,015	0,392	0,955	0,250	0,123
Corner Detection	6	0,545	0,875	0,789	0,870	87,031	98,630	26,630	0,366	0,875	0,211	0,130
Corner Detection	7	0,514	0,933	0,765	0,876	92,255	98,305	44,031	0,330	0,933	0,235	0,124
Corner Detection	8	0,533	0,909	0,765	0,875	90,036	98,361	35,165	0,358	0,909	0,235	0,125
Corner Detection	9	0,533	0,940	0,783	0,892	93,175	98,734	42,068	0,347	0,940	0,217	0,108
Corner Detection	10	0,498	0,976	0,766	0,894	96,552	98,734	63,307	0,388	0,976	0,234	0,106
Corner Detection	11	0,498	0,908	0,721	0,868	90,125	98,913	21,827	0,480	0,908	0,279	0,132
Corner Detection	12	0,537	0,873	0,770	0,893	86,932	98,969	19,388	0,451	0,873	0,230	0,107
Corner Detection	13	0,569	0,857	0,810	0,888	85,449	98,684	25,486	0,429	0,857	0,190	0,112

Table 39 Sensitivity Analysis for Corner Detection for Fixed FPR = 0.25 at Clip Limit = 0.01

Detection Type	Iteration	Threshold	Sensitivity	Specificity	AROC	Accuracy %	PPV %	NPV %	Process Time	TPR	FPR	AAC
Corner Detection	1	0,533	0,974	0,749	0,876	96,184	98,507	63,240	0,599	0,974	0,251	0,124
Corner Detection	2	0,525	0,879	0,749	0,881	87,261	98,592	23,620	0,316	0,879	0,251	0,119
Corner Detection	3	0,525	0,923	0,741	0,865	91,388	98,529	33,892	0,301	0,923	0,259	0,135
Corner Detection	4	0,498	0,974	0,747	0,877	96,154	98,551	61,619	0,307	0,974	0,253	0,123
Corner Detection	5	0,506	0,932	0,750	0,877	92,275	98,611	36,607	0,326	0,932	0,250	0,123
Corner Detection	6	0,545	0,875	0,750	0,870	86,921	98,630	22,581	0,345	0,875	0,250	0,130
Corner Detection	7	0,514	0,967	0,748	0,876	95,310	98,305	59,722	0,307	0,967	0,252	0,124
Corner Detection	8	0,533	0,939	0,749	0,875	92,822	98,361	43,532	0,329	0,939	0,251	0,125
Corner Detection	9	0,533	0,980	0,748	0,892	96,898	98,734	65,046	0,344	0,980	0,252	0,108
Corner Detection	10	0,498	0,976	0,750	0,894	96,541	98,734	61,194	0,384	0,976	0,250	0,106
Corner Detection	11	0,498	0,831	0,745	0,868	82,781	98,913	13,629	0,437	0,831	0,255	0,132
Corner Detection	12	0,537	0,901	0,749	0,893	89,591	98,969	22,099	0,403	0,901	0,251	0,107
Corner Detection	13	0,569	0,976	0,750	0,888	96,500	98,684	62,121	0,339	0,976	0,250	0,112

Table 40 Gaussian Model Based Detection Algorithm Parameters with Clipping Limit = 0.01

Detection Type	Clipping Limit	Iteration	Alpha	Constant
GM Detection	0,01	1	0,03	2,5
GM Detection	0,01	2	0,03	2,3
GM Detection	0,01	3	0,03	2,1
GM Detection	0,01	4	0,05	2,1
GM Detection	0,01	5	0,02	2,1
GM Detection	0,01	6	0,01	2,1
GM Detection	0,01	7	0,01	2,3

Table 41 Sensitivity Analysis for GM Detection for Optimum Threshold at Clip Limit = 0.01

Detection Type	Iteration	Threshold	Sensitivity	Specificity	AROC	Accuracy %	PPV %	NPV %	Process Time	TPR	FPR	AAC
GM Detection	1	0,925	0,937	0,788	0,898	85,874	80,000	93,227	0,057	0,937	0,212	0,102
GM Detection	2	0,894	0,930	0,745	0,881	82,853	75,000	92,835	0,058	0,930	0,255	0,119
GM Detection	3	0,867	0,917	0,752	0,877	84,684	83,333	87,004	0,101	0,917	0,248	0,123
GM Detection	4	0,867	0,917	0,752	0,877	84,684	83,333	87,004	0,069	0,917	0,248	0,123
GM Detection	5	0,867	0,917	0,752	0,877	84,684	83,333	87,004	0,071	0,917	0,248	0,123
GM Detection	6	0,867	0,917	0,752	0,877	84,684	83,333	87,004	0,071	0,917	0,248	0,123
GM Detection	7	0,894	0,930	0,745	0,881	82,853	75,000	92,835	0,068	0,930	0,255	0,119

Table 42 Sensitivity Analysis for GM Detection for Fixed FPR = 0.25 at Clip Limit = 0.01

Detection Type	Iteration	Threshold	Sensitivity	Specificity	AROC	Accuracy %	PPV %	NPV %	Process Time	TPR	FPR	AAC
GM Detection	1	0,925	1,000	0,735	0,898	87,138	80,000	100,000	0,114	1,000	0,265	0,102
GM Detection	2	0,894	0,930	0,745	0,881	82,853	75,000	92,835	0,057	0,930	0,255	0,119
GM Detection	3	0,867	0,953	0,738	0,877	86,265	83,333	91,997	0,060	0,953	0,262	0,123
GM Detection	4	0,867	0,953	0,738	0,877	86,265	83,333	91,997	0,058	0,953	0,262	0,123
GM Detection	5	0,867	0,953	0,738	0,877	86,265	83,333	91,997	0,058	0,953	0,262	0,123
GM Detection	6	0,867	0,953	0,738	0,877	86,265	83,333	91,997	0,066	0,953	0,262	0,123
GM Detection	7	0,894	0,930	0,745	0,881	82,853	75,000	92,835	0,058	0,930	0,255	0,119

Table 43 Maximally Stable Extremal Region Detection Algorithm Parameters with Clipping Limit = 0.01

Detection Type	Clipping Limit	Iteration	MinDiversity	MaxVariation	MaxArea	MinArea	Delta
MSER Detection	0,01	1	0,8	0,1	0,03	0,0015	3
MSER Detection	0,01	2	0,8	0,5	0,03	0,0015	3
MSER Detection	0,01	3	0,8	1	0,03	0,0015	3
MSER Detection	0,01	4	0,5	1	0,03	0,0015	3
MSER Detection	0,01	5	0,5	1	0,05	0,0015	3
MSER Detection	0,01	6	0,5	1	0,05	0,0015	3
MSER Detection	0,01	7	0,5	1	0,05	0,005	3
MSER Detection	0,01	8	0,5	1	0,05	0,005	2,5
MSER Detection	0,01	9	0,5	1,5	0,05	0,005	2,5
MSER Detection	0,01	10	0,5	1,5	0,05	0,005	2
MSER Detection	0,01	11	0,5	1,5	0,05	0,005	3,5
MSER Detection	0,01	12	0,4	1,5	0,05	0,005	2,5
MSER Detection	0,01	13	0,4	1	0,05	0,005	2,5

Table 44 Sensitivity Analysis for MSER Detection for Optimum Threshold at Clip Limit = 0.01

Detection Type	Iteration	Threshold	Sensitivity	Specificity	AROC	Accuracy %	PPV %	NPV %	Process Time	TPR	FPR	AAC
MSER Detection	1	0,435	0,947	0,701	0,897	93,439	98,276	42,509	0,026	0,947	0,299	0,103
MSER Detection	2	0,435	0,920	0,718	0,874	90,422	97,468	43,192	0,025	0,920	0,282	0,126
MSER Detection	3	0,435	0,920	0,716	0,872	90,416	97,468	42,925	0,025	0,920	0,284	0,128
MSER Detection	4	0,435	0,900	0,737	0,899	89,499	99,083	18,919	0,024	0,900	0,263	0,101
MSER Detection	5	0,435	0,902	0,738	0,898	89,740	99,091	19,281	0,024	0,902	0,262	0,102
MSER Detection	6	0,435	0,902	0,738	0,898	89,740	99,091	19,281	0,032	0,902	0,262	0,102
MSER Detection	7	0,510	0,889	0,778	0,916	87,879	97,561	41,176	0,024	0,889	0,222	0,084
MSER Detection	8	0,510	0,941	0,791	0,931	92,805	97,917	56,347	0,026	0,941	0,209	0,069
MSER Detection	9	0,510	0,941	0,791	0,931	92,805	97,917	56,347	0,025	0,941	0,209	0,069
MSER Detection	10	0,510	0,941	0,791	0,931	92,805	97,917	56,347	0,025	0,941	0,209	0,069
MSER Detection	11	0,510	0,889	0,778	0,916	87,879	97,561	41,176	0,024	0,889	0,222	0,084
MSER Detection	12	0,510	0,905	0,791	0,925	89,585	98,077	41,304	0,025	0,905	0,209	0,075
MSER Detection	13	0,510	0,905	0,791	0,925	89,585	98,077	41,304	0,026	0,905	0,209	0,075

Table 45 Sensitivity Analysis for MSER Detection for Fixed FPR = 0.25 at Clip Limit = 0.01

Detection Type	Iteration	Threshold	Sensitivity	Specificity	AROC	Accuracy %	PPV %	NPV %	Process Time	TPR	FPR	AAC
MSER Detection	1	0,435	0,789	0,745	0,897	78,716	98,276	16,088	0,024	0,789	0,255	0,103
MSER Detection	2	0,435	0,760	0,749	0,874	75,918	97,468	19,684	0,024	0,760	0,251	0,126
MSER Detection	3	0,435	0,760	0,746	0,872	75,900	97,468	19,473	0,026	0,760	0,254	0,128
MSER Detection	4	0,435	0,800	0,747	0,899	79,849	99,083	9,844	0,024	0,800	0,253	0,101
MSER Detection	5	0,435	0,805	0,748	0,898	80,325	99,091	10,078	0,026	0,805	0,252	0,102
MSER Detection	6	0,435	0,805	0,748	0,898	80,325	99,091	10,078	0,024	0,805	0,252	0,102
MSER Detection	7	0,510	0,889	0,750	0,916	87,755	97,561	37,500	0,027	0,889	0,250	0,084
MSER Detection	8	0,510	0,941	0,748	0,931	92,695	97,917	50,237	0,028	0,941	0,252	0,069
MSER Detection	9	0,510	0,941	0,748	0,931	92,695	97,917	50,237	0,025	0,941	0,252	0,069
MSER Detection	10	0,510	0,941	0,748	0,931	92,695	97,917	50,237	0,024	0,941	0,252	0,069
MSER Detection	11	0,510	0,889	0,750	0,916	87,755	97,561	37,500	0,024	0,889	0,250	0,084
MSER Detection	12	0,510	0,905	0,744	0,925	89,435	98,077	35,145	0,026	0,905	0,256	0,075
MSER Detection	13	0,510	0,905	0,744	0,925	89,435	98,077	35,145	0,027	0,905	0,256	0,075

Table 46 Sensitivity Analysis for Weighted Mean Shift Algorithm at Clipping Limit = 0.01

Fusion Type	Clipping Limit	Iteration	Bandwidth	Threshold	Sensitivity	Specificity	AROC	Accuracy %	PPV %	NPV %	Process Time	TPR	FPR	AAC
Weigthed Mean Shift	0,01	1	20	0,490	0,727	0,977	0,878	85,227	96,970	78,182	5,567	0,727	0,023	0,122
Weigthed Mean Shift	0,01	2	30	0,608	0,621	0,966	0,902	79,310	94,737	71,795	3,163	0,621	0,034	0,098
Weigthed Mean Shift	0,01	3	37	0,624	0,714	0,952	0,923	83,333	93,750	76,923	2,665	0,714	0,048	0,077
Weigthed Mean Shift	0,01	4	40	0,604	0,412	0,941	0,690	67,647	87,500	61,538	2,427	0,412	0,059	0,310
Weigthed Mean Shift	0,01	5	50	0,600	0,733	0,933	0,933	83,333	91,667	77,778	2,180	0,733	0,067	0,067
Weigthed Mean Shift	0,01	6	70	0,431	0,600	0,900	0,956	75,000	85,714	69,231	1,830	0,600	0,100	0,044

APPENDIX-B

LOCAL COORDINATE MAPPING RESULTS FOR TRAIN SET

Table 47 Coordinate Transformations at CMA-ES, SVD and Eigenvalue Decomposition at Iteration 1

		CMA_ES			SVD			Eigen Value Decomposition			Difference Between CMA-ES and SVD		
2D Image Coordinates		3D World Coordinates (cm)			3D World Coordinates (cm)			3D World Coordinates (cm)			3D World Coordinates Error (cm)		
x	y	x	y	z	x	y	z	x	y	z	x	y	z
89	82	99	30	0	100	31	0	100	31	0	-1	-1	0
77	205	99	98	0	99	102	0	99	102	0	0	-4	0
119	251	158	104	0	153	108	0	153	108	0	5	-4	0
136	206	168	76	0	164	80	0	164	80	0	4	-4	0
119	107	136	35	0	138	38	0	138	38	0	-2	-3	0
185	244	217	78	0	206	82	0	206	82	0	11	-4	0
183	186	206	54	0	200	59	0	200	59	0	6	-5	0
17	239	1	156	0	1	163	0	1	163	0	0	-7	0
132	49	141	8	0	145	8	0	145	8	0	-4	0	0
57	18	49	5	0	46	0	0	46	0	0	3	5	0
26	113	7	64	0	1	69	0	1	69	0	6	-5	0
19	17	-12	11	0	-29	3	0	-29	3	0	17	8	0
57	128	61	62	0	60	66	0	60	66	0	1	-4	0
99	193	126	82	0	125	87	0	125	87	0	1	-5	0
92	29	96	5	0	98	2	0	98	2	0	-2	3	0
82	168	101	75	0	101	80	0	101	80	0	0	-5	0
113	141	134	52	0	135	56	0	135	56	0	-1	-4	0
190	53	191	3	0	194	4	0	194	4	0	-3	-1	0
176	13	175	-9	0	180	-10	0	180	-10	0	-5	1	0
181	271	219	91	0	206	94	0	206	94	0	13	-3	0
39	184	38	103	0	37	110	0	37	110	0	1	-7	0
142	18	147	-4	0	152	-6	0	152	-6	0	-5	2	0
44	261	56	152	0	56	156	0	56	156	0	0	-4	0
140	241	178	91	0	171	95	0	171	95	0	7	-4	0
42	67	31	33	0	26	33	0	26	33	0	5	0	0
161	111	177	28	0	177	32	0	177	32	0	0	-4	0
158	161	182	49	0	179	54	0	179	54	0	3	-5	0
153	65	163	12	0	166	13	0	166	13	0	-3	-1	0
191	84	197	14	0	197	17	0	197	17	0	0	-3	0
26	167	12	99	0	9	106	0	9	106	0	3	-7	0
140	267	182	104	0	174	106	0	174	106	0	8	-2	0
155	126	174	35	0	173	39	0	173	39	0	1	-4	0
84	144	100	62	0	101	66	0	101	66	0	-1	-4	0
8	61	-30	39	0	-48	38	0	-48	38	0	18	1	0
9	125	-24	79	0	-35	86	0	-35	86	0	11	-7	0
34	55	16	29	0	9	27	0	9	27	0	7	2	0
42	239	49	138	0	50	143	0	50	143	0	-1	-5	0
5	186	-29	125	0	-35	134	0	-35	134	0	6	-9	0
147	155	171	49	0	169	54	0	169	54	0	2	-5	0
9	267	-14	187	0	-11	191	0	-11	191	0	-3	-4	0
42	35	28	16	0	21	12	0	21	12	0	7	4	0
120	21	126	-1	0	130	-3	0	130	-3	0	-4	2	0
199	117	207	24	0	205	29	0	205	29	0	2	-5	0
154	225	188	79	0	182	83	0	182	83	0	6	-4	0
17	90	-10	54	0	-22	56	0	-22	56	0	12	-2	0
52	152	56	77	0	55	83	0	55	83	0	1	-6	0
135	76	148	19	0	151	20	0	151	20	0	-3	-1	0

Table 48 Coordinate Transformations at CMA-ES, SVD and Eigenvalue Decomposition at Iteration 2

		CMA_ES			SVD			Eigen Value Decomposition			Difference Between CMA-ES and SVD		
2D Image Coordinates		3D World Coordinates (cm)			3D World Coordinates (cm)			3D World Coordinates (cm)			3D World Coordinates Error (cm)		
x	y	x	y	z	x	y	z	x	y	z	x	y	z
48	20	28	2	0	30	1	0	30	1	0	-2	1	0
178	181	198	58	0	196	58	0	196	58	0	2	0	0
40	62	20	32	0	21	30	0	21	30	0	-1	2	0
16	20	-45	7	0	-35	6	0	-35	6	0	-10	1	0
183	120	200	33	0	194	32	0	194	32	0	6	1	0
152	154	177	53	0	173	52	0	173	52	0	4	1	0
21	100	-12	65	0	-11	62	0	-11	62	0	-1	3	0
81	163	102	78	0	100	77	0	100	77	0	2	1	0
193	83	206	17	0	198	16	0	198	16	0	8	1	0
100	28	113	1	0	108	1	0	108	1	0	5	0	0
160	112	181	34	0	176	32	0	176	32	0	5	2	0
113	127	137	50	0	134	49	0	134	49	0	3	1	0
184	51	198	4	0	189	4	0	189	4	0	9	0	0
54	131	58	71	0	56	69	0	56	69	0	2	2	0
24	245	23	153	0	17	161	0	17	161	0	6	-8	0
137	67	158	17	0	152	16	0	152	16	0	6	1	0
135	246	167	96	0	167	99	0	167	99	0	0	-3	0
131	206	161	81	0	160	82	0	160	82	0	1	-1	0
87	80	101	32	0	98	30	0	98	30	0	3	2	0
87	195	113	92	0	111	93	0	111	93	0	2	-1	0
180	246	202	82	0	203	84	0	203	84	0	-1	-2	0
25	42	-16	22	0	-11	20	0	-11	20	0	-5	2	0
139	21	157	-5	0	149	-5	0	149	-5	0	8	0	0
182	268	204	90	0	206	92	0	206	92	0	-2	-2	0
25	175	12	112	0	8	112	0	8	112	0	4	0	0
12	122	-28	85	0	-28	82	0	-28	82	0	0	3	0
176	13	190	-11	0	180	-10	0	180	-10	0	10	-1	0
109	104	131	40	0	127	38	0	127	38	0	4	2	0

Table 49 Coordinate Transformations at CMA-ES, SVD and Eigenvalue Decomposition at Iteration 3

		CMA_ES			SVD			Eigen Value Decomposition			Difference Between CMA-ES and SVD		
2D Image Coordinates		3D World Coordinates (cm)			3D World Coordinates (cm)			3D World Coordinates (cm)			3D World Coordinates Error (cm)		
x	y	x	y	z	x	y	z	x	y	z	x	y	z
147	253	180	93	0	178	97	0	178	97	0	2	-4	0
29	245	18	159	0	27	157	0	27	157	0	-9	2	0
33	170	9	109	0	24	104	0	24	104	0	-15	5	0
21	60	-53	37	0	-17	33	0	-17	33	0	-36	4	0
157	152	179	51	0	177	50	0	177	50	0	2	1	0
18	130	-40	92	0	-13	85	0	-13	85	0	-27	7	0
27	19	-48	3	0	-10	3	0	-10	3	0	-38	0	0
182	58	191	9	0	189	7	0	189	7	0	2	2	0
88	81	94	33	0	99	31	0	99	31	0	-5	2	0
128	50	141	11	0	141	9	0	141	9	0	0	2	0
85	27	80	3	0	89	2	0	89	2	0	-9	1	0
52	131	41	73	0	52	70	0	52	70	0	-11	3	0
137	221	168	84	0	167	87	0	167	87	0	1	-3	0
114	110	132	42	0	133	40	0	133	40	0	-1	2	0
80	186	99	91	0	101	91	0	101	91	0	-2	0	0
152	108	171	33	0	169	32	0	169	32	0	2	1	0
41	64	1	34	0	24	31	0	24	31	0	-23	3	0
76	168	90	84	0	93	82	0	93	82	0	-3	2	0
197	86	204	19	0	201	17	0	201	17	0	3	2	0
173	249	200	83	0	198	87	0	198	87	0	2	-4	0
113	148	136	60	0	136	59	0	136	59	0	0	1	0
150	14	159	-6	0	159	-8	0	159	-8	0	0	2	0

Table 50 Coordinate Transformations at CMA-ES, SVD and Eigenvalue Decomposition at Iteration 4

		CMA_ES			SVD			Eigen Value Decomposition			Difference Between CMA-ES and SVD		
2D Image Coordinates		3D World Coordinates (cm)			3D World Coordinates (cm)			3D World Coordinates (cm)			3D World Coordinates Error (cm)		
x	y	x	y	z	x	y	z	x	y	z	x	y	z
139	232	175	104	0	170	91	0	170	91	0	5	13	0
81	81	87	44	0	90	32	0	90	32	0	-3	12	0
79	154	105	85	0	96	73	0	96	73	0	9	12	0
162	24	172	-21	0	170	-5	0	170	-5	0	2	-16	0
144	150	170	66	0	166	52	0	166	52	0	4	14	0
28	248	80	136	0	25	160	0	25	160	0	55	-24	0
160	103	181	35	0	175	29	0	175	29	0	6	6	0
103	36	100	6	0	113	5	0	113	5	0	-13	1	0
35	148	58	94	0	24	88	0	24	88	0	34	6	0
27	31	0	27	0	-9	12	0	-9	12	0	9	15	0
22	82	18	63	0	-12	49	0	-12	49	0	30	14	0